Abstract of "Discrete Dislocation Modeling of Fracture/Fatigue"

by Sutee Olarnrithinun, Ph.D., Brown University, May 2013

The discrete dislocation (DD) plasticity is truly mechanism-based plasticity and well-suited for mesoscale modeling in metal. The effects of size-dependent plasticity and plastic dissipation emerge naturally from this framework. The micromechanics of fracture is material dependent and involves a broad range of length and time scales. The intermediate situation between the cleavage crack growth and the plastic dissipation involved in fracture based on DD plasticity is focused here. Fracture crack growth is affected by dislocations: (i) dislocation motion shields the crack tip and increases the dissipation energy and (ii) the local stress concentration associated with discrete dislocation in the vicinity of the crack tip can reach atomic bond strength, causing the crack to grow. In this work fatigue crack growth from small cracked particle into single crystal is first investigated with a focus on the effects of plastic confinement due to elastic particle, and elastic modulus mismatch between the reinforcement and matrix phases. The results show that fatigue crack growth from micron-scale particles is strongly influenced by size effect of plasticity, elastic mismatch, and the presence of particle to plastic flow. However the yield stress of the matrix material and the cohesive strength in the cohesive zone model are unrealistic due to the limitations of the standard DD algorithm. Also the computational cost and storage can be reduced by using symmetric boundaries. Therefore the new algorithm of discrete dislocation plasticity to improve the computational efficiency and its application in the short crack problem are presented here. To study the role of plastic anisotropy on crack growth in a single crystal, the standard DD formulation can be extended to perform the effects of plastic dissipation and dislocation/crack interaction on the basal cleavage in HCP-like material. To do so, the concept of plastic flow controlled by a Peierls stress is first implemented to the standard DD methodology. The results show that the fracture toughness is largely independent of plastic anisotropy. Interestingly, the fracture toughnesses of both Peierls stress-

controlled flow material and obstacle-controlled flow material are unified through the new Stress Gradient Plasticity concept.

Discrete Dislocation Modeling of Fracture/Fatigue

by

Sutee Olarnrithinun

B.Eng, Mechanical Engineering, King Mongkut Institue of Technology, North Bangkok, 2000

M.Eng., Mechanical Engineering, Chulalongkorn University, 2004

A Dissertation submitted in partial fulfillment of the requirements for the Degree of Doctor of Philosophy in the School of Engineering at Brown University

Providence, Rhode Island

May 2013

This dissertation by Sutee Olarnrithinun is accepted in its present form
by the School of Engineering as satisfying the
dissertation requirement for the degree of Doctor of Philosophy.

Date ______________ ____

William A. Curtin, Director

Recommended to the Graduate Council

Date ______________ ____

Janet Blume, Reader

Date ______________ ____

Nitin P. Padture, Reader

Approved by the Graduate Council

Date ______________ ____

Peter M. Weber, Dean of the Graduate School

Vitæ

Sutee Olarnrithinun was born in Bangkok, Thailand on August 2, 1977 to Somyos and Suwanna. Sutee earned degree of his Bachelor of Engineering from King Mongkut Institute of Technology, North Bangkok in Mechanical Engineering in 2000. He continued further studies to earn a Masters in Mechanical Engineering at Chulalongkorn University in 2004. In the same year he worked for National Metal and Materials Technology Center (MTEC) as an engineer utilizing commercial FEM codes until 2006. In fall 2006, he started his doctoral studies at Brown University in solid mechanics. Sutee looks forward to join National Metal and Materials Technology Center, Thailand as a researcher.

Acknowledgements

First, I would like to thank my advisor, Prof. William A. Curtin for being a source of guidance, and encouragement over the years. He has set an example of excellence as a researcher, mentor, instructor, and role model of mine. He has been always more than generous with both his time and effort of discussion and suggestion since the moment of our first correspondence. I always receive the useful help, suggestion, or insight that I need when working on my project. His concern is for his students, not only in the academic area, but also in matters of personal difficulties; I am very impressed and grateful.

I would like to thank my thesis committee members, Prof.Janet Blume and Prof.Nitin P. Padture, for their time and guidance to provide constructive criticism of my work. Special thanks to Prof.Srinath Chakravarthy of Northeastern University, for his continued assistance and insight over the past few years during his time as a post-doc at Brown University. Certainly, all the faculty members in Solid Mechanics group were always to offer their impressive lectures in courseworks at Brown which is more insightful in solid mechanics. I also offer my appreciation to Prof.Pramote Dechaumphai, Dr.Suwat Jirathearanat, and Dr.Nuwong Chollacoop for encouraging me to pursue PhD studies at Brown University.

I give thanks to the fellow members of the Solid Mechanics class of 2006, and my group members for their support, patience and encouragement during our time together. I also thank Pat Capeace, Peggy Mercurio and Stephanie Gesualdi for administrative support to make my life easier. I would especially like to thank my amazing roomates, Dr.Yang Lei, Dr.Jun Song, Moses Riner and Dr.Nitin Jadhav, for the support, and constant encouragement to my work over the years. I also must thank Yi Dong who spend time and enjoy coffee with me in both Providence for 5 years and Lausanne, Switzerland for 10 months, and even in the last moment of my thesis defense.

Finally, I give all my love and thanks to my family for the long distance support. In particular, I deeply acknowledge and thank my parents, my wife and my son. Without their love and support none of this could be possible, so I dedicate this work to them.

Dedicated to my parents, my wife and son

Contents

List of Tables

List of Figures

Chapter 1

Introduction

Fracture is the process of separating a solid object into two or more pieces. Generally, this involves nucleation and propagation of crack-like defects. In most fields, growth is much better understood than crack nucleation. That is why most fracture studies have been focused on growth initiation and propagation of pre-existing crack. A key difficulty is that fracture spans several length scales from the atomistic scale to the macroscopic scale. Fig. 1.1 shows the important length scales involved for cleavage crack growth in ductile materials. At the sufficiently large scale as shown in Fig. 1.1(a), stress and deformation fields near a crack tip can be described in terms of a macroscopic, and often isotropic, continuum. Under small scale yielding where the plastic flow and separation region are very small compared to the crack length, the stress intensity factor (K) in linear elastic fracture mechanics (LEFM) serves as characterizing parameter to describe the near crack tip stress field, while the energy release rate (Γ) is used as characterizing parameter when the plastic flow becomes larger compared to the crack length. At the smaller scale in Fig. 1.1(b), the anisotropic nature of individual grains comes into play. The fluctuation of stress and strain can be described by crystal plasticity models. Closer to the crack tip, Fig. 1.1(c), the energy dissipation is associated with the mobile dislocations moving through the lattice. Each dislocation induces a localized stress concentration, giving rise to large local stress fluctuations that vary as dislocations moving. The dislocations

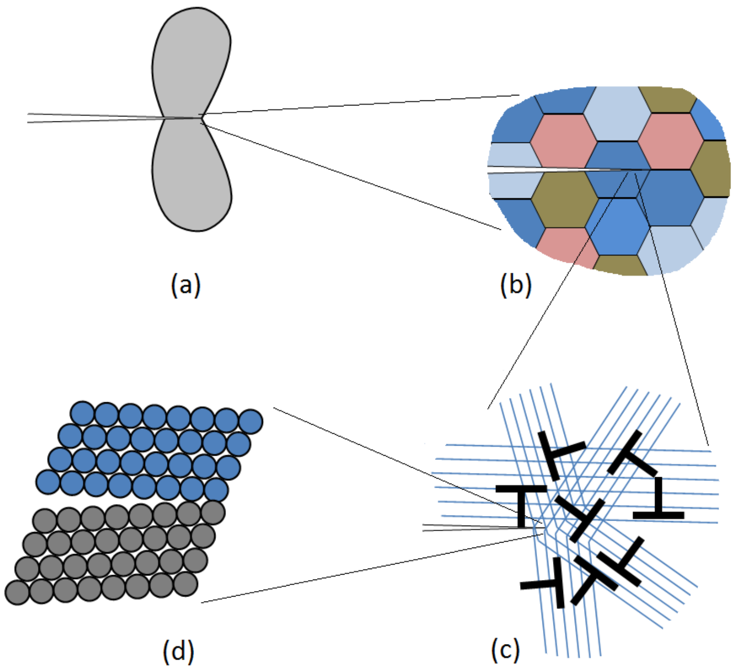

Figure 1.1: The various relevant scale in fracture: (a) the macroscopic scale that the plastic zone is governed by continuum plastic flow (b) the grain scale in a polycrystalline metal (c) the scale of discrete dislocations and of discrete slip planes (d) the atomic scale.

can also be generated from the crack tip itself or from nearby sources. As shown in Fig. 1.1(d), the actual separation process takes place at the atomic scale. The stress fields from the next higher-up scales increase the stress level of the atomic bonds to be broken when the stresses at this scale reach the value on the order of bond strength. This emphasized the fact that fracture is highly localized at the atomic scale but is driven by the macroscopic applied load to atomic scale via stress field on smaller length scales.

Over last two decades, computational studies of crystal plasticity, material instabilities, such as shear bands, and fracture mechanisms have made major contributions to understand the mechanical behavior of materials (Tvergaard and Herrmann (1993), Beaudoin et al. (1995), Camacho and Ortiz (1996)). The prediction of fracture toughness requires a material length scale to accurately describe the material behavior over the size matter scale (so-called *mesoscale*). The importance of failure mechanisms, such as nucleation, growth and coalescence of voids or fracture, occurs on this mesoscale of which the formulations are intermediate between an atomistic and an unstructured continuum description of deformation processes. There is lots of experimental evidence (e.g. Fleck et al. (1994), Lloyd (1994), Ma and Clarke (1995), Shell De Guzman et al. (1993)) showing the size dependence effect of plastic flow; smaller is stronger. Atomistic models certainly incorporate the proper underlying mechanics, but they are not practical for the analysis of larger mesoscale structure. It is worth noting that as a general rule, computations on smaller size scales require smaller time steps. Computational power limits such studies to millions of atoms, typically, corresponding to submicron volumes of material. In materials that deform plastically and/or undergo fatigue degradation, the collective behavior of defects, especially dislocations, occurs on much larger scales of microns to millimeters. While the conventional continuum plasticity can significantly reduce the number of degrees of freedom relative to atomic simulations, incorporation of a material length scale is also necessary to capture the defect behaviors, i.e. shear bands and strain localization, Zhou et al. (1994), Aifantis (1987), Zbib and Aifantis (1988), De Borst and Mühlhaus (1992). Such defect behaviors are subsumed into effective constitutive laws for the material deformation by introducing a material parameter with the dimensions of length. The continuum model of fracture processes containing a length scale have been developed, see e.g. Tvergaard and Hutchinson (1992), Buehler et al. (2003). Despite the substantial successes, the material length scale over the continuum description is not straightforward due to the requirement from experimental data for the prediction.

The fracture processes are composed of the underlying physical mechanisms of both irreversible deformation (i.e. plastic dissipation) and material separation (i.e. atomic bond breaking). Alternative method to eliminate the atomistic degree of freedom and to consider only the tracking explicit defects is discrete dislocation dynamics (Van der Giessen and Needleman (1995), Fivel et al. (1996), Zbib and Diaz de la

Rubia (2002)). The discrete dislocation modeling solves boundary value problems for the body containing dislocations which are characterized entirely by continuum representations using concepts such as eigenstrains and introducing mobility laws to capture the motion of the dislocations under applied stresses. Discrete dislocation plasticity has emerged as a mean to study plastic deformation, providing fundamental understanding of hardening/strengthening, size effects and plastic dissipation. That framework does not require the specification of elastic-plastic constitutive laws. Discrete dislocation plays a dual role in fracture; (i) their motion leading to plastic flow increases the resistance to crack growth; (ii) The crack propagation is promoted by the local stress concentration associated with the dislocations.

This thesis will focus on the two dimensional discrete dislocation (2d-DD) of Van der Giessen and Needleman (1995) which provides computational advantages for a certain class of problems and has low computational cost compared with 3d-DD. A variety of fracture problems including fatigue crack growth in single crystals (Deshpande et al. (2002, 2003a)), crack growth in thin film (O'Day et al. (2006)), bimaterial interfaces (O'Day and Curtin (2005)) and recently an insight into size effects in fracture (Chakravarthy and Curtin (2010b)). The stability, accuracy and robustness of the 2d-DD methodology for fracture can be improved significantly by the new algorithm, proposed by Chakravarthy and Curtin (2011a). Here, a few more applications of 2d-DD is applied for the detailed quantitative analysis of two problems of considerable current interest; (i) fatigue crack growth from a cracked particle into a ductile matrix and (ii) the effect of plastic anisotropy on basal crack growth in HCP-like material.

1.1 Fatigue in metal matrix composite materials

Metal matrix composites (MMCs) provide significantly enhanced properties over unreinforced materials, such as higher strength and weight saving, are potentially valuable in aerospace and transportation applications. The strengthening takes place by the reinforcing phase carrying much of the applied load. Under an applied load, the load is transferred from the weaker matrix, across the matrix/particle interface, to the typically stiffer reinforcing particle. An increase in reinforcement volume fraction, or a decrease in particle size, increases the amount of indirect strengthening, since a larger amount of interfacial area exists for dislocation punching to occur (Chawla et al. (1998a), Ganesh and Chawla (2005)). It should be noted that cracked particles in the composite, which may result from the processing of composites with fairly coarse particulate reinforcement, do not contribute to load transfer or strengthening and would decrease strength. The high stress concentration at the tips of the cracked particles would also contribute to a lower ductility in the composite, compared to the unreinforced one.

Much understanding of the behavior of metal matrix composites has been obtained from analyses based on conventional, size independent plasticity theory, Allison et al. (1993). However, two commonly observed characteristics of the material behavior are not amenable to explanation within such a framework: (i) the stress-strain behavior is size dependent for reinforcing particle sizes in the micrometer range; and (ii) the matrix stress-strain behavior that needs to be assumed in calculations to get good agreement with experiment is often different from the observed stress-strain behavior of the unreinforced material. Cleveringa et al. (1997) first analyzed a simple model of composite material through the discrete dislocation method giving rise to stress-strain behavior that is strongly affected by the size, shape, and distribution of the reinforcing phase. Cleveringa et al. (1997, 1998), also found a strong size dependence of the stress-strain response from microstructural factors including resistance to dislocation motion and pileup at precipitates and/or reinforcing particles.

An important incentive to develop MMCs is that monolithic lightweight alloys have inadequate fatigue resistance for many demanding applications. The use of high stiffness particle reinforcement, such as SiC, can result in a substantial increase in fatigue resistance while maintaining cost at an acceptable level. This is an important design criterion in many applications such as in automotive components. The fatigue resistance of particulate MMCs depends on a variety of factors, including reinforcing particle volume fraction, size, matrix microstructure, the presence of inclusions or defects that arise from processing, and testing environment (Hall et al. (1994), Chawla et al. (1998b)). Many literature data (e.g. Tanaka et al. (2000), Chen et al. (2001), Milan and Bowen (2003),etc.) show that the fatigue threshold of particle reinforced metal matrix composites is generally larger than that of unreinforced metals. With decreasing particle size, for a given reinforcement volume fraction, the reinforcement interparticle spacing decreases, resulting in more barriers for the reversible slip motion that takes place during fatigue, and a decrease in strain localization by cyclic slip refinement. Above a critical particle size, reinforcement fracture is predominant and contributes to premature fatigue life, because of the increased propensity for particle cracking as the particle size increases, Chawla et al. (1998b). In fatigue, failure processes are affected by a variety of microstructural factors, including resistance to dislocation motion and pileup at precipitates and/or reinforcing particles. Fatigue failure in MMC materials can occur from the small particle cracking followed by crack propagation into the surrounding ductile matrix. The time spent in fatigue crack formation, which is comprised of the crack incubation, nucleation and microstructurally small propagation, is consumed up to 70-90% of the total fatigue life, Brockenbrough et al. (1994), Fan et al. (2001), Suresh (1998). The focus of this thesis is on understanding the mechanics of the small fatigue crack in such MMC materials. The crack growth from pre-cracked micron-scale elastic particles into single crystals is investigated by using 2d-DD to characterize the effects of (i) plastic confinement due to the elastic particle and (ii) elastic modulus mismatch between the particle and the ductile matrix. This will be analyzed in Chapter 3.

1.2 Crack growth in a HCP-like material

The study on crack growth in HCP-like materials is motivated by the recent work of crack propagation on the basal planes in single-crystal zinc (Catoor and Kumar (2008)). The main purpose of that study is to understand the mechanisms of crack transmission across grain boundaries. Before doing that problem, it is essential to understand the micromechanisms involved in crack growth in the simplest situations that would characterize Mode-I crack growth along the basal plane in single crystals. Pure zinc with a hexagonal structure provides several advantages to the study: (i) there is a system with only one set of parallel cleavage planes that can be fabricated; (ii) zinc can grow into single crystals without much difficulty; and (iii) there is a large body of conducted research describing the mechanical properties of zinc, which can eventually be used in an analytical and numerical model. A number of prior experiments studying crack initiation in pure zinc single crystals also exist (Deruyttere and Greenough (1956), Gilman (1958), Parisot et al. (2004), Stofel (1962)). Catoor and Kumar (2008) investigated crack growth along the basal plane in single-crystal zinc for two crack growth directions, $[2\bar{1}\bar{1}0]$ (orientation 1) and $[10\bar{1}0]$ (orientation 2), and performed complementary Finite Element Method (FEM) crystal plasticity simulations. Catoor and Kumar (2008) found that there is a complex interplay of dynamic and quasi-static processes that bring about interesting micromechanisms, i.e. the role of pre-existing twins and of ligaments that bridge cracks on retarding the crack growth by micro-crack nucleation on the parallel basal plane. Moreover the crack growth response was found to depend on the crystallographic direction in which the crack is made to grow. In that study the FEM models did not allow crack growth, and so could not be compared directly with the experimental crack growth results. In that work, the role of plastic anisotropy in crack propagation has not been given adequate consideration. Thus the effect of basal/pyramidal interaction on crack growth remains unclear, and modeling of crack growth in such plastically anisotropic systems has not been investigated. The intrinsic lattice resistance to dislocation motion, or Peierls stress, is one essential feature controlling plastic anisotropy in HCP-like materials such as Zn, Mg, and Ti. In Chapter 4 we implement an anisotropic Peierls model as a friction stress within a 2d-DD plasticity model and investigate the role of plastic anisotropy on the crack tip stress fields, crack growth, toughening, and microcracking.

1.3 Thesis outline

The remainder of this thesis is organized as follows. Chapter 2 presents a brief overview on the standard DD formulation of Van der Giessen and Needleman (1995), and the limitation of the standard algorithm to the crack or/and inclusion problem is discussed. Also new algorithms proposed by Chakravarthy and Curtin (2011a) to overcome these limitations are reviewed briefly in this chapter.

Chapter 3 presents the analysis of fatigue crack growth from micron-scale particles. The monotonic and cyclic crack growth rate of a short crack is strongly influenced by microstructure. The crack growth rate of a short crack is changed by the presence of a brittle reinforcing phase in the specimen. In this case, the different contributions due to the particle on the crack growth rate are decomposed. These contributions presumably are: (i) the plasticity confinement due to the interface; and (ii) the deformation compatibility due to the elastic mismatch between two phases. The plasticity of the ductile phase is modeled using a standard 2d-DD simulation. The crack surface is implemented by a cohesive zone model to capture the crack propagation. The comparisons with the crack growth rate obtained in a single crystal are reported. The plasticity confinement and the deformation compatibility tend to decrease the fatigue threshold and also the exponent of the Paris law.

The role of plastic anisotropy for the basal cleavage in HCP-like materials is examined in Chapter 4. The 2d-DD models and algorithm is extended to control plastic dissipation on basal and pyramidal slip systems separately by using Peierls stress concept. First, tension tests for a pure single crystal with no obstacles to dislocation motion are carried out to capture the general flow behavior in pure HCP-like materials having slip on basal and pyramidal planes. Then Mode-I crack growth in such a single crystal of the HCP material is analyzed using the 2d-DD model. Generally the fracture toughness is largely independent of the plastic anisotropy and decreased as increasing Peierls stress on the pyramidal planes which is consistent with recent experiments on Zn. Analysis of the fracture toughness with Stress Gradient Plasticity concepts is investigated for materials with flow stress controlled by both Peierls stress and dislocation obstacles. Finally, the DD simulations show that local stress concentrations exist sporadically along the pyramidal plane(s) that emanate from the current crack tip, suggesting an origin for experimentally-observed basal-plane microcracking near the tip of large cracks.

In Chapter 5, crack growth from a cracked particle into realistic elastic-plastic matrix material is examined. We first implement the symmetric boundaries to the 2d-DD simulation by using the new superposition scheme (O'Day and Curtin (2004)) to reduce computational domain. Also the new algorithm by Chakravarthy and Curtin (2011a) for crack growth simulations is implemented to model materials with realistic yield stress and realistic cohesive strength. With the high yield strength, the fracture behavior is a brittle-like material behavior in general. A comparison of material properties between Al-alloy and Ni-alloy with the same yield stress and cohesive properties is presented. It demonstrates that there are some effects of the material parameters (i.e. Young's modulus) influencing the toughness through the mutual elastic interaction of the defects and dislocation evolution. Chapter 6 summarizes the main conclusions and discusses avenues of future research.

Chapter 2

Discrete Dislocation Plasticity

Discrete dislocation (DD) methods have been applied to study plastic deformation at sub-continuum scales over the last two decades, providing understanding of strengthening/hardening phenomena and of size effects in plasticity. The DD method of Van der Giessen and Needleman (1995) solves boundary value problems for isotropic elastic bodies which contain mobile dislocations. Without any special constitutive model, plastic deformation is described through the motion of large number of discrete dislocations, which are treated as singularities in an isotropic elastic solid. The DD method is well-suited for micro-scale deformation analysis in metals since size-dependent plastic flow emerges naturally from strain/stress gradients through the discrete dislocation evolution. With only a few physically-based constitutive rules governing the short range dislocation interactions (e.g. dislocation nucleation, motion and annihilation), the DD method has shown a remarkable ability to reproduce complicated physical phenomena. Discrete dislocation models show that fatigue crack growth emerges naturally under cyclic loading without requiring any additional rules or interface/material constitutive modifications (Deshpande et al. (2002, 2003b)); a strong Bauschinger effect during unloading of a metal matrix composite with elastic particle reinforcements(Bittencourt et al. (2003)); and that the Mode-I crack tip fields in a single crystal are in good agreement with Drugan (2001)'s analytical crystal plasticity solution. This section briefly presents an overview of the standard DD methodology by Van der Giessen and Needleman (1995) and its numerical implementation for a crack problem. Special attention is given to aspects of the formulation that, for computational reasons, tend to discourage its application to problems with instability in dislocation velocity, elastic inhomogeneities and difficulties in capturing micrometer of crack growth with sub-Å mesh sizes around the crack tip. These limitations are avoided using a new algorithm for discrete dislocation modeling of fracture proposed by Chakravarthy and Curtin (2011a).

2.1 General approach

Fully three-dimensional DD models have been used primarily to study strain hardening due to dislocation forest interactions in nominally homogeneous blocks of material under uniform loading at the largest scales (Devincre and Kubin (1997), Hartmaier et al. (1997)), individual dislocation/obstacle interactions (Wang et al. (2000), Shin et al. (2005)) and individual loop dislocation/crack interactions (Mastorakos and Zbib (2006)) at the smallest scales. The use of 2d-DD model is common for solving the complex boundary value problems, due to the high computational expense of 3d-DD. The two dimensional plane strain DD method has been widely used to provide insight into a variety of fracture problems including fatigue crack growth in single crystals (Deshpande et al. (2002, 2003b)), crack growth in thin films (O'Day et al. (2006)), bi-material interfaces (O'Day and Curtin (2004)) and size effects in fracture (Chakravarthy and Curtin (2010b)). From those works, attention is focussed on small strain and small scale yielding for crack tip plasticity. Thus the stress intensity factor, K, is used to characterize the loading type of fracture. The discrete dislocation framework models dislocations as point defects in an isotropic elastic material where they glide on a discrete set of slip planes. The edge dislocation lines are straight and parallel to the x_3 direction (out of plane). Long range dislocation interactions operate through their singular continuum elastic fields. These fields are expected to accurately characterize the dislocation beyond distances of several times the Burgers vector from the dislocation core (Hull and Bacon (2011)). Short range dislocation interactions are governed by a set of constitutive rules for dislocation nucleation, motion, and annihilation, which were proposed by Kubin et al. (1992). These rules are designed to approximate the complicated atomic-level interactions of dislocation segments that approach within a few Burgers vectors. In fact realistic dislocation interactions are more complex and so rules for junction formation and destruction, dislocation climb, and cross slip also exist. In 2d-DD, dislocation nucleation is assumed as the creation of a dislocation dipole to mimic the mechanism of Frank-Read loop expansion. The dislocation segment glides with a velocity which is proportional to the Peach-Koehler force resolved on the dislocation segment. The general discrete

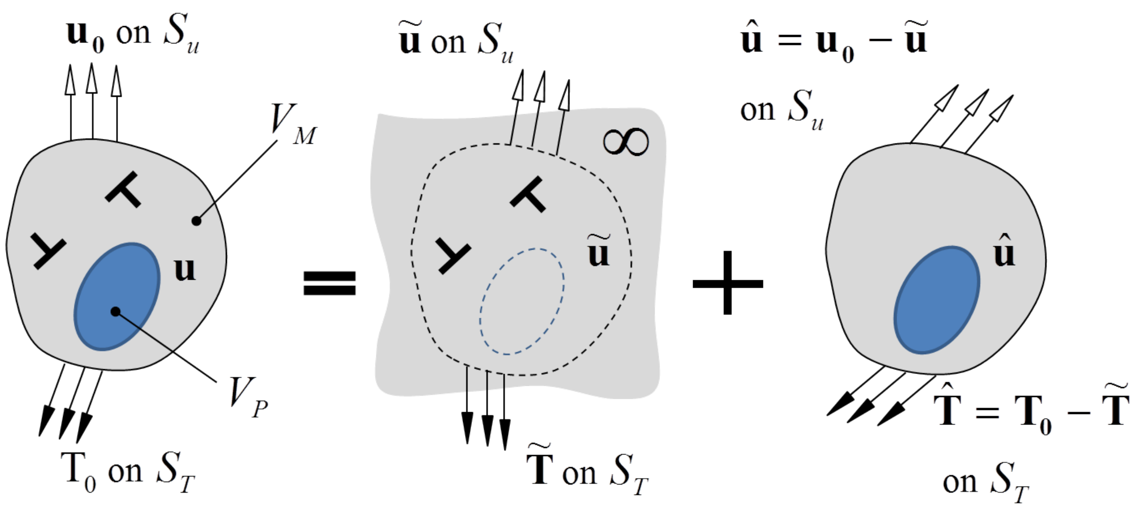

Figure 2.1: General discrete dislocation boundary value problem using the superposition scheme of Van der Giessen and Needleman (1995).

dislocation boundary value problem is shown in Fig. 2.1 for an arbitrary body of volume V subject to boundary conditions $\mathbf{u}$=$\mathbf{u}_0$ on S_u, and $\mathbf{T}$=$\mathbf{T}_0$ on S_T. The body V is composed of an elastic-plastic matrix, V_M, and an elastic inclusion or particle, V_P, with elastic modulus L^M_{ijkl} and L^P_{ijkl}, respectively. The stress, strain and displacement fields are written as

$$\boldsymbol{\sigma} = \tilde{\boldsymbol{\sigma}} + \hat{\boldsymbol{\sigma}}\,, \quad \boldsymbol{\epsilon} = \tilde{\boldsymbol{\epsilon}} + \hat{\boldsymbol{\epsilon}}\,, \quad \mathbf{u} = \tilde{\mathbf{u}} + \hat{\mathbf{u}}$$
$$\text{or} \tag{2.1}$$
$$\sigma_{ij} = \tilde{\sigma}_{ij} + \hat{\sigma}_{ij}\,, \quad \epsilon_{ij} = \tilde{\epsilon}_{ij} + \hat{\epsilon}_{ij}\,, \quad u_i = \tilde{u}_i + \hat{u}_i$$

where the ($\tilde{\ }$)-fields are the singular fields associated with each individual dislocation in an infinite body of a homogeneous matrix material and the ($\hat{\ }$)-fields are the corrective fields for the actual boundary conditions, finite geometry and presence of inclusions. The strain-displacement relations are related by

$$\epsilon_{ij} = \frac{1}{2}\left(\frac{\partial u_i}{\partial x_j} + \frac{\partial u_j}{\partial x_i}\right) \tag{2.2}$$

The stress field satisfies the equilibrium equation

$$\frac{\partial \sigma_{ij}}{\partial x_j} = 0 \tag{2.3}$$

With V_M denoting the volume occupied by the matrix and V_P the volume occupied by the particle, the stress and strain fields are related by

$$\sigma_{ij} = \begin{cases} L^M_{ijkl}\epsilon_{kl} & \text{in } V_M \\ L^P_{ijkl}\epsilon_{kl} & \text{in } V_P \end{cases} \tag{2.4}$$

Throughout $V = V_M + V_P$, the dislocation stress field $\tilde{\sigma}_{ij}$ is related to the strain field $\tilde{\epsilon}_{kl}$ by

$$\tilde{\sigma}_{ij} = L^M_{ijkl}\tilde{\epsilon}_{kl} \tag{2.5}$$

Hence,

$$\hat{\sigma}_{ij} = \begin{cases} L^M_{ijkl}\hat{\epsilon}_{kl} & \text{in } V_M \\ L^P_{ijkl}\hat{\epsilon}_{kl} + (L^P_{ijkl} - L^M_{ijkl})\tilde{\epsilon}_{kl} & \text{in } V_P \end{cases} \tag{2.6}$$

The polarization stress term, $(L^P_{ijkl} - L^M_{ijkl})\tilde{\epsilon}_{kl}$ in Eq. 2.6, vanishes for a homogeneous elastic materials, i.e. for $L^P_{ijkl} \equiv L^M_{ijkl}$. Since $\tilde{\sigma}_{ij}$ satisfies equilibrium throughout V, $\hat{\sigma}_{ij}$ satisfies

$$\frac{\partial \hat{\sigma}_{ij}}{\partial x_j} = 0 \tag{2.7}$$

in V with the boundary conditions

$$\hat{u}_i = u_{0,i} - \tilde{u}_i \quad \text{on } S_u\ , \hat{T}_i = T_{0,i} - \tilde{T}_i \quad \text{on } S_T \tag{2.8}$$

where S_u is that part of the boundary on which displacements $u_{0,i}$ are prescribed, and S_T that part of the boundary on which tractions $T_{0,i}$ are prescribed, with $T_i = \sigma_{ij} n_j$ and n_j is the outward normal to the surface. Equations (2.7) and (2.8) together with the constitutive relation Eq. (2.6) give a boundary value problem for the $(\hat{\ })$-fields. The $(\hat{\ })$-fields are smooth in V and a finite element method is used to obtain a solution. The polarization stress, $(L^P_{ijkl} - L^M_{ijkl})\tilde{\epsilon}_{kl}$ in Eq. 2.6 for V_P, is computed in FEM as a body force.

2.1.1 Dislocation constitutive rules

The 2d-DD method of Van der Giessen and Needleman (1995) treats edge dislocations with Burgers vector b as line defects in a plane strain problem of elastically-isotropic single-crystal materials. The potentially active slip planes are introduced with a given spacing d. The evolution of dislocations is modeled through a set of constitutive rules governing dislocation glide, nucleation, annihilation and interaction with obstacles. Dislocation glide is controlled by Peach-Koehler force. The component of Peach-Koehler force on the slip plane and normal to the dislocation line is the driving force for dislocation glide, which for the I^{th} dislocation is

$$f^{(I)} = m_j \left(\hat{\sigma}_{ji} + \sum_{J \neq I}^{N_d} \sigma^{(J)}_{ji} \right) b_i \tag{2.9}$$

where b_i are the vector components of the Burgers vector on the slip planes, m_j are the components of the slip plane normal, σ_{ij} are the total stress tensor components at the location of the dislocation and N_d is the number of dislocations. The total stress includes applied stress, image stresses, and the interaction stresses with all other dislocations. In most DD simulations the glide velocity v is taken to be linearly related to the Peach-Koehler force f with a drag coefficient B written as

$$f^{(I)} = Bv^{(I)} \tag{2.10}$$

and dislocation positions are updated using a forward-Euler scheme. For FCC modeling, there are three slip systems initially free of dislocations, but dislocations can be generated from discrete Frank-Read-like sources that are randomly distributed on the slip planes with a density ρ_s. These sources generate dislocation dipoles when the Peach-Koehler force exceeds a critical value of $\tau_s b$ during a period of time t_{nuc}, with the sign of the dipole determined by the direction of Peach-Koehler force. The initial width of the generated dipole L_{nuc} is chosen so that the two dislocations are in equilibrium at the nucleation stress,

$$L_{nuc} = \frac{\mu}{2\pi(1-\nu)} \frac{b}{\tau_{nuc}} \tag{2.11}$$

Annihilation of two oppositely signed dislocations on the same slip plane occurs when they come within a critical distance of $L_e = 6b$ (Kubin et al. (1992)). Obstacles blocking dislocation motion are also randomly placed on the slip planes to represent small precipitates, solutes, or forest dislocations. The obstacles pin the dislocations until the Peach-Koehler force is sufficient to overcome the obstacle strength τ_{obs}. It is worth noting that the DD method does not solve for equilibrium dislocation distributions. Since dislocations always have velocity which is proportional to Peach-Koehler force, the dislocation configuration at the end of any increment is an instantaneous snapshot of the constantly evolving dislocation structure.

2.1.2 An interface model for Mode-I crack growth

A common technique in the numerical modeling of fracture crack growth is that of the cohesive zone model. This is most effective when the problem geometry suggests a particular region where crack growth is likely. While a wide assortment of specific cohesive zone models have been used to model fracture in metals (Needleman (1987), Xu and Needleman (1993), Tvergaard and Hutchinson (1993)), the laws are in general defined by the maximum cohesive strength and a length scale. Measurement and first principle calculation suggest that, for cleavage of atomic planes in crystalline metals, the peak traction is on the order of *gigapascals*, and the cohesive length is on the order of *nanometers*, giving a work of separation of roughly 1 J/m^2 for most metals (Raynolds et al. (1996)). However, for numerical implementation, such large cohesive strengths and small cohesive lengths demand an extremely fine mesh to resolve the stress gradients in the vicinity of the crack tip. For the fatigue problem in Chapter 3, the cohesive strength is taken on the order of *megapascals* and the cohesive length is chosen on the order of *microns*, so that the cohesive work of fracture remains unchanged. By this way, the cohesive zone characterizes a fracture process over hundreds or thousands of atomic planes, rather than between two planes of atoms.

Here we focus on the fracture/fatigue problems Mode-I crack growth where the symmetry with respect to the crack plane is used, so only the upper half of the crystal is directly simulated. Crack growth is modeled using a cohesive zone model which extends along the crack plane. Along the cohesive surface, $T_1 = 0$ from symmetry while $T_2 = T_n$ has a universal binding form (Rose et al. (1981)), as shown in Fig. 2.2(a). In the reversible case, the cohesive behavior for both loading and unloading behavior follows the same curve as

$$T_n(\Delta_n) = -\frac{\sigma_{coh}\Delta_n}{\delta_n}\exp\left(\frac{\delta_n - \Delta_n}{\delta_n}\right) \tag{2.12}$$

where $\Delta_n = 2u_2(x_1, 0)$, σ_{coh} is the normal cohesive strength and δ_n is a characteristic

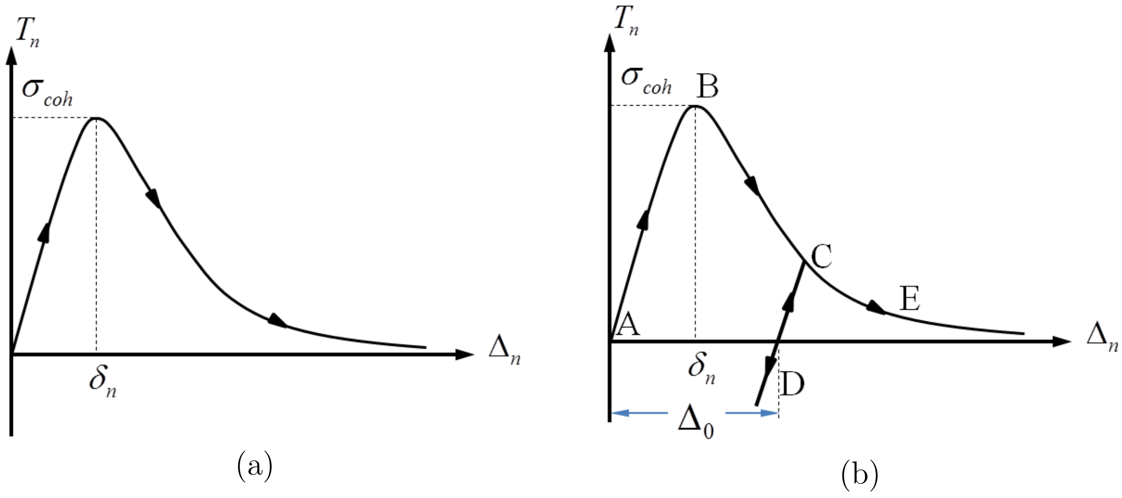

Figure 2.2: Schematics of cohevie zone laws (a)the reversibly cohesive relation (b)the irreversibly cohesive relation.

opening length. A cohesive relation that accounts for the irreversibility of separation is modeled by specifying unloading from and reloading to the monotonic cohesive function, as illustrated in Fig. 2.2(b) (Deshpande et al. (2001b)). Unloading from point C takes place along path CD, with stiffness

$$\frac{\partial T_n}{\partial \Delta_n} = -\frac{\exp(1)\sigma_{coh}}{\delta_n} \tag{2.13}$$

During the reloading, the traction increases along DC and then follows the original softening curve BCE. This is a phenomenological cohesive relation introduced to model the effects of irreversibility arising from the formation of an oxide layer (Deshpande et al. (2001b)). Under continued cyclic loading conditions, the permanent opening Δ_0 (see Fig. 2.2(b)) grows, but only up to a value Δ_s=4 nm which is a representative value for the oxide layer thickness on aluminium under ambient conditions (Do et al. (1999)). The work of separation is $\phi_n = \exp(1)\delta_n\sigma_{coh}$, corresponding to a Mode-I fracture toughness in the absence of plasticity which is given by

$$K_0 = \sqrt{\frac{E\phi_n}{1-\nu^2}} \tag{2.14}$$

In all calculations, a finite element mesh consisting of bilinear quadrilateral elements is employed. The length of the nonlinear cohesive region ahead of the crack tip, δ_c, just at the point of crack growth is

$$\delta_c = \frac{\pi \phi_n E}{8\sigma_{coh}^2} \tag{2.15}$$

This length is used to define the minimum mesh spacing of width $\delta_c/4$, which is used over a region that extends $40\delta_c$ ahead of the initial crack tip. In the numerical solutions of the DD problem, extreme care, however, must be taken in the presence of the cohesive zone particularly when the cohesive zone lengths are comparable to atomistically-derived values.

2.2 New algorithm for Fatigue/Fracture

As mentioned before, several modifications to the existing 2d-DD and cohesive zone methodology have been made by Chakravarthy and Curtin (2011a). These modifications significantly improve the capability to model materials with the realistic material properties, especially cohesive properties. A brief overview of the new approach for improvements is presented in this section.

2.2.1 A new superposition technique

A new superposition scheme along with a Newton-Raphson iterative scheme was first suggested by O'Day and Curtin (2004). The motivation of this new superposition framework is to reduce the computational cost in calculating polarization stress for elastically inhomogeneous problems. Also the new superposition framework is found to have several other important benefits: (i) the DD calculation is largely decoupled from the specific model geometry and boundary conditions (see Chapter 5 applied for symmetric boundaries) and (ii) ability to easily model bodies with multiple distinct regions of dislocation activities, e.g. polycrystalline metal (Shishvan et al. (2011)), metallic multi-layers (O'Day and Curtin (2005), Chng et al. (2006)). The decom-

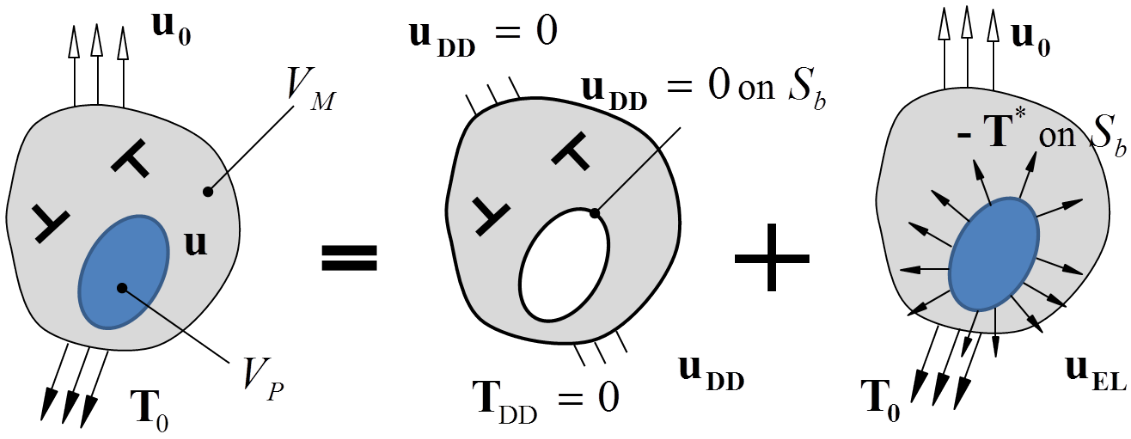

Figure 2.3: Schematic decomposition into two subsidiary problems: (DD) homogeneous discrete dislocation sub-problem solved with the standard formulation, subject to zero displacement boundary conditions and (EL) elastic sub-problem contain all specific boundary conditions and loading, solved with standard elastic FEM, O'Day and Curtin (2004).

position of the new superposition scheme is illustrated in Fig. 2.3. The total field is composed of (i) a homogeneous discrete dislocation sub-problem (DD) subject to zero displacement boundary conditions and (ii) a fully elastic sub-problem (EL) subject to all actual boundary conditions. The DD sub-problem is solved using the standard DD methodology but with the special boundary conditions while the EL sub-problem is solved using standard finite element methodology with a Newton-Raphson(NR) iterative scheme to capture accurately the nonlinearity of the interface (e.g. the cohesive zone interface and the particle−matrix interface, etc.). The DD sub-problem encompasses only the portion of the structure where dislocation activity is permitted. The key point is that the DD sub-problem is always homogeneous so that the polarization stresses vanish. An outcome of the DD sub-problem solution at each increment is a traction $\mathbf{T}^*$ along the constrained boundary S_b, thus information about the dislocation structure in any plastic regions of the body is transmitted to the remainder of the structure through the addition of a body force $-\mathbf{T}^*$ along S_b in EL sub-problem, as shown in Fig. 2.3. Chakravarthy and Curtin (2011a) showed that various instabilities reported when using the standard superposition are eliminated with the use of this new superposition scheme.

2.2.2 A moving mesh scheme

The moving mesh method is implemented to capture micrometer crack growth with nanometer mesh sizes. The essence of this method is that, in a frame of reference moving with the crack tip, the dislocations and all field variables including those of cohesive zone can be considered as moving in the opposite direction. The moving mesh method allows the crack to grow forward for some distance and then shifts the dislocations and field variables backward by exactly that amount. This re-establishes the crack tip at the original location relative to the original mesh and leaves the stiffness matrix unchanged. A more detailed description is given in the work of Chakravarthy and Curtin (2011a).

2.2.3 A gradient correction of the velocity

The gradient correction for computing dislocation velocity completely eliminates instabilities and oscillations in the standard forward-Euler approach. The incremental dislocation motion gives rise to spurious large interaction forces when the dislocations become too close. To avoid unfavorable behavior, the gradient correction of the mobility law proposed by Chakravarthy and Curtin (2011a) is given as

$$v = \begin{cases} \dfrac{(f - \tau_f b \cdot sign(f))}{B} \cdot \dfrac{1}{\left(1 - \dfrac{1}{B}\dfrac{\partial f}{\partial x}\Delta t\right)} & , \quad \text{if } |f| > \tau_f b \\ 0 & , \quad \text{otherwise} \end{cases} \tag{2.16}$$

where B is a drag coefficient of dislocations on the slip planes and τ_f is a frictional stress on the slip planes. This correction also precludes the introduction of an artificially-low cut-off velocity for dislocation motion.

2.2.4 Modified dislocation nucleation

In generic DD simulations, a dislocation dipole is instantaneously nucleated at a distance $L_{nuc}/2$ on each side of the source when the stress on the source is greater than the source strength τ_{nuc} for a time period t_{nuc}. For the sources located close to the crack surface, the abrupt injection of a dislocation dipole results in a sudden jump in the displacement field on the crack boundary, which causes numerical instabilities. In addition, spurious forces are introduced on dislocation pileups due to the sudden injection of a dipole into the existing pileup. To avoid large spurious forces arising from the abrupt introduction of a newly-nucleated dipole, the "latent" nucleating dislocations in the dipole are introduced gradually over the nucleation time t_{nuc} so that the Burger vector and the separation distance of the virtual dipole increase linearly with time as

$$b^{dipole}(t) = b\frac{t}{t_{nuc}}, \quad t < t_{nuc}, \quad \tau > \tau_{nuc} \tag{2.17}$$

$$x^{dipole}(t) = L_{nuc}\frac{t}{t_{nuc}}, \quad t < t_{nuc}, \quad \tau > \tau_{nuc} \tag{2.18}$$

Specifically, the *latent* dislocations are not subject to the mobility law until $t \geq t_{nuc}$, but do contribute to the Peach-Koehler forces on all other dislocations and to the displacements and traction on the boundaries.

Chapter 3

Fatigue from a Short Cracked Particle

A wide variety of structural alloys contain brittle particles dispersed in a ductile metallic matrix. While such particles are sometimes added for structural purposes, often they arise during processing. These particles, or inclusions, are often undesirable byproducts of the material fabrication because fracture can originate by particle cracking followed by propagation into the surrounding ductile matrix. In particular, under cyclic loading conditions, cracks formed during processing or during the initial stages of loading will grow and ultimately lead to failure of the structure or component. Fig. 3.1 shows one example of such fatigue crack growth from a particle in an Al-7075 alloy. The factors governing the propagation of a crack from a brittle particle into a surrounding ductile phase are thus of considerable practical importance for applications of many structural metals.

As a result of the problem's importance, computational and modeling studies of crack growth across an interface have been carried out under both monotonic and cyclic loading conditions, e.g. Suresh et al. (1992), Romeo and Ballarini (1997), Chen (1997), Kim et al. (1997), Siegmund et al. (1997), Wappling et al. (1998), He et al. (2004), Gall et al. (2001). Some studies consider the materials on each side of the interface to deform plastically but with a mismatch in flow strength (Sugimura et al. (1995), Pippan and Riemelmoser (1998), Milan and Bowen (2003)) while other studies consider one phase elastic and the other plastic (Wang and Siegmund (2006)). Heterogeneity in material properties affects crack growth because (i) the mismatch in material properties affects the near-crack-tip stress distribution when the crack tip is near the interface and (ii) there is typically a mismatch in the crack growth resistance of the phases on either side of the interface Suresh (1998). While the focus in previous studies has mainly been on crack growth across or along an interface, our aim is to model the situation depicted in Fig. 3.1 where a crack initiates in a brittle particle and then grows into a ductile matrix. Our interest is in understanding the role of constraints on plastic flow due to the particle and the effect of elastic mismatch on the crack growth, both in the limit of micron-scale particles where plasticity size effects are known to play an important role.

Typically fatigue calculations are carried out within a framework where a fatigue crack growth law, e.g. a Paris law or a Coffin−Manson law, is postulated a priori and the emphasis is on calculating the driving force. While such laws can be calibrated for bulk materials through a suite of experimental studies under controlled loading situations and for long cracks, the resulting laws may not apply in other situations such as near an interface and/or for microstructurally small cracks, in which the plastic fields may be modified due to constraint and size effects. For instance, Gall et al. (2001) use a continuum cyclic plasticity model to compute plastic strain ranges ahead of a cracked particle, but average over a size smaller than 1 mm in front of the crack to obtain the driving force used in a subsequent crack growth law. While providing some guidance, the applicability of the assumed constitutive behavior is questionable. To account differences between small and large scales, continuum models have been developed to move from small cracks to large cracks (McDowell et al. (2003), Xue et al. (2007)), but such models introduce additional parameters to characterize the fatigue behavior which require extensive calibration and employ assumptions whose origins lie in concepts emerging from continuum plasticity. Recent work has avoided

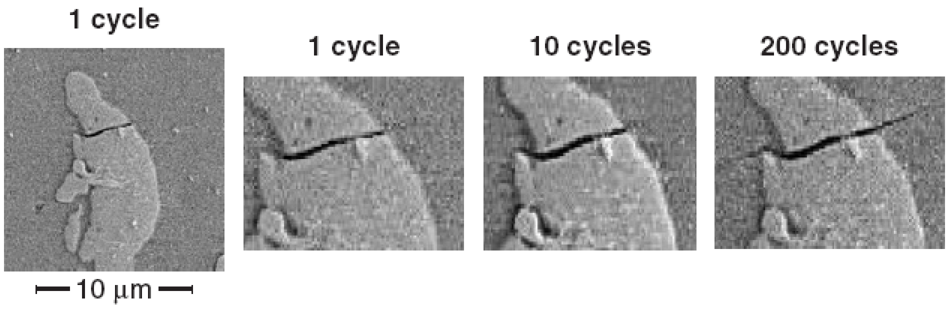

Figure 3.1: Fatigue crack initiating from a micron-scale particle and growing into the Al matrix in Al7075 (Courtesy of Northrop-Grumman Corporation).

assumptions of continuum plasticity by basing the plastic deformation on the creation, motion, and annihilation of dislocations. These discrete dislocation (DD) models have been shown to predict a host of phenomena, such as size effects in yielding, fracture, sliding, indentation, and polycrystals (Nicola et al. (2006), Deshpande et al. (2003a,b), Chng et al. (2006), Widjaja et al. (2007), Balint et al. (2005, 2008)), not accounted for in conventional continuum plasticity. In particular, DD studies of fatigue crack growth have been carried out (Deshpande et al. (2003a,b, 2002), Riemelmoser et al. (1997, 2001), Wilkinson et al. (1998)) that provide insight and guidance into fatigue crack growth problems where continuum plasticity and standard fatigue laws may be inapplicable. Most importantly for our current work is that these DD analyses predict that fatigue crack growth arises naturally under cyclic loading conditions without introducing additional parameters. The DD studies of fatigue in single-crystal materials have shown the existence of a threshold, a Paris power-law regime, striations, scaling with material properties and a short-crack regime Deshpande et al. (2003a,b, 2002).

Here, we use discrete dislocation plasticity to study monotonic and fatigue crack growth in a situation where both microstructure and micron-scale cracks exist, thus combining simultaneously elastic mismatch effects, interface effects, and small-crack effects. Specifically, we analyze the growth of a crack from an initially-cracked elastic particle into a ductile single crystal matrix. Plastic flow in the matrix arises from the motion of discrete dislocations following a set of constitutive rules discussed below. The fracture properties of the ductile material are embedded in a cohesive surface constitutive relation that permits only straight crack growth (Needleman (1987)). A key aspect of the formulation is that the plastic stress-strain response, the evolution of any dislocation structure, and the crack initiation and growth in the ductile matrix, are outcomes of the solution of the boundary value problem. We emphasize that the only distinction between an analysis of monotonic crack growth and crack growth under cyclic loading conditions is in the time dependence of the remote loading; the underlying material is identical. These features are common to prior DD studies of fatigue. The aim of the analyses here is to obtain insight into the effects of microstructural heterogeneity, through the presence of a cracked particle, on fatigue crack growth behavior. We find that the presence of a particle generally accelerates fatigue relative to the same crack in a single crystal, due to both elastic mismatch and plastic constraint effects, as discussed subsequently.

3.1 Geometry and formulation

We consider a planar single crystal reinforced by an elastic particle containing an initial crack, as sketched in Fig. 3.2(a). The formulation and numerical method follow those in Cleveringa et al. (2000), Deshpande et al. (2002, 2003a), except that here the elastic mismatch between the particle and the surrounding matrix gives rise to a polarization stress term.

The crystal matrix is taken to be elastically isotropic with Young's modulus E_m=70 GPa and Poisson's ratio ν_m=0.33, representative values for aluminium. The crystal matrix has three slip systems, with slip planes at an angle $\phi^{(\alpha)}$, α=1, 2, 3 to the x_1-axis, with $\phi^{(1)}$=60°, $\phi^{(2)}$=-60° and $\phi^{(3)}$=0°, as shown in Fig. 3.2a. Potential slip planes are spaced by $100b$ where b is the Burgers vector, b=0.25 nm. The particle is also taken to be elastically isotropic with Youngs modulus E_p and Poissons ratio ν_p=0.33. Initially, the three slip systems are free of mobile dislocations, but dislocations are nucleated from point sources, randomly distributed with a density of $20/\mu m^2$. The dislocation sources mimic Frank-Read sources by nucleating a dipole

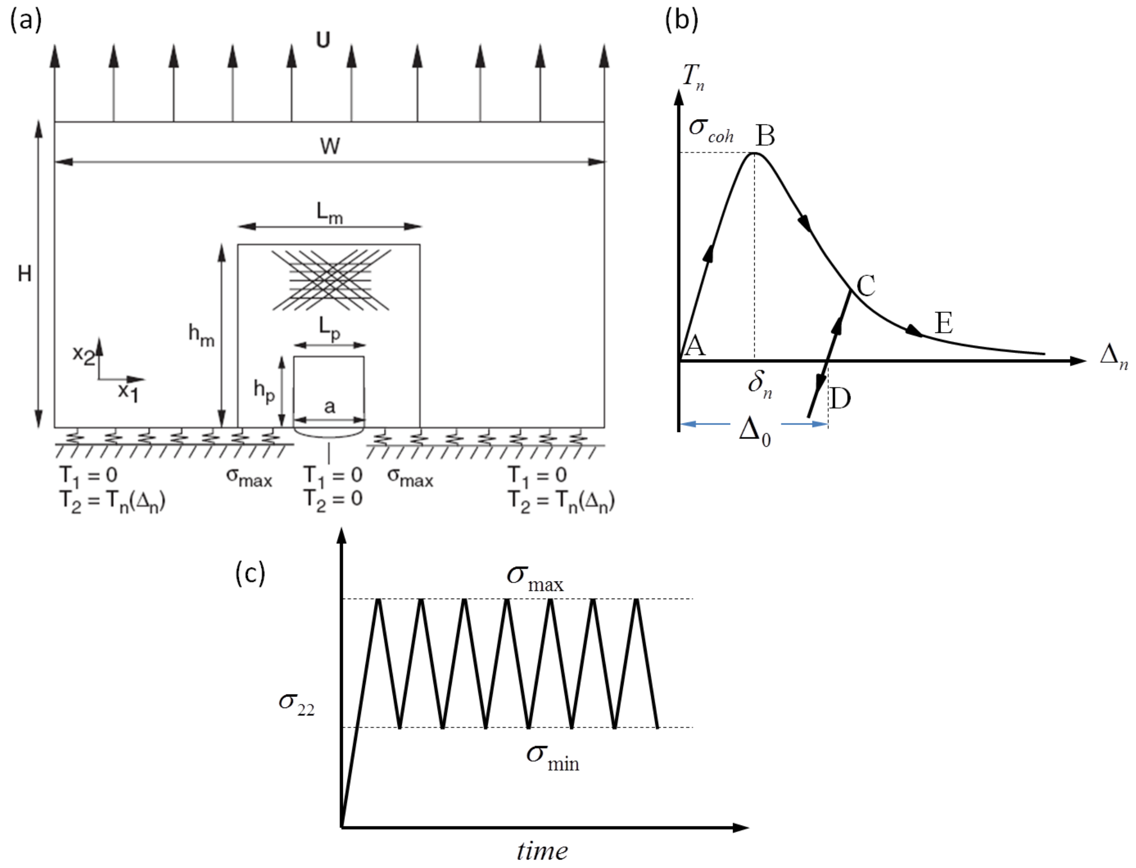

Figure 3.2: Sketch of anlysed specimen with the imposedd boundary conditions. (b) Schematic of the irreversibly cohesive relation. (c) Schematic of the applied stress versus time.

when the Peach−Koehler force on the source exceeds the value $\tau_{nuc}b$ during a period of time t_{nuc}; here τ_{nuc}= 20 MPa and t_{nuc}=10 ns. The long-range elastic interactions between dislocations are accounted for directly in the boundary value problem solution. Short range interactions enter through a set of constitutive rules, of the type suggested by Kubin et al. (1992), for dislocation glide, annihilation, and pinning by obstacles. The glide speed is taken to be linearly related to the Peach−Koehler force with a drag coefficient $B = 10^4$ Pa s, a representative value for several FCC crystals (Paufler (1983)). Dislocations of opposite sign annihilate each other when they come within a critical distance of $L_e = 6b$. There is a random distribution of 50 point obstacles per μm^2, which represent either small precipitates on the slip plane or forest dislocations on out-of-plane slip systems. These obstacles pin dislocations until the Peach−Koehler force attains the obstacle strength τ_{obs}, where τ_{obs}=60 MPa. For computational convenience, dislocation sources and obstacles are restricted to a process window of dimensions $L_m \times h_m$ around the cracked particle with L_m=50 mm and h_m=50 mm (see Fig. 3.2(a)).

The specific boundary value problem analyzed is sketched in Fig. 3.2(a). A rectangular block of height $2H$ and width W contains a centrally-located particle of height $2h_p$ and width L_p. We use W=100 mm, H=500 mm, and $L_p = h_p = a = 10\mu$m with the particle between $L_p/2$ and $L_p/2$ along the x1-direction and between 0 and h_p along the direction x_2. Symmetry about $x_2 = 0$ is assumed so the region analyzed occupies $-W/2 \leq x_1 \leq W/2$ and $0 \leq x_2 \leq H$. This block is subjected to tensile loading through a prescribed displacement rate $\dot{U}(t)$ on the top surface where $\dot{(\,)}$ denotes time differentiation. The imposed stress σ is then calculated as

$$\sigma = \frac{1}{W}\int_{-W/2}^{W/2} T_2(x_1, H)dx_1 \; . \tag{3.1}$$

and, under cyclic loading conditions, has the time variation sketched in Fig. 3.2(c). For a homogeneous elastic material, the applied stress σ is related to a Mode-I stress intensity factor as (Tada et al. (2000)),

$$K_I = \sigma\sqrt{\pi a/2} \tag{3.2}$$

Corrections due to the finite ratio of a/W=0.1 are negligible. We note that Eq. 3.2 does not give the local crack-tip K_I in an elastically inhomogeneous material but we nevertheless employ this definition to quantify the level of loading. Crack growth is then modeled through a cohesive surface along x_2=0 in the matrix ($|x_2| \geq a/2$). Along the cohesive surface T_1=0 (from symmetry) while T_2 has a irreversible cohesive relation modeled by specifying unloading from and reloading to the monotonic cohesive function, as illustrated in Fig. 3.2(b) (Deshpande et al. (2001b)), see Chapter 2. Under Mode-I loading conditions, crack growth in an elastic solid initiates at K_I/K_0=1 (Suresh (1998)). The cohesive properties were taken as σ_{coh}=0.70 GPa and $\delta_n = 2b$ giving a work of fracture ϕ_n=1.0 J/m^2 and K_0=0.280 MPa$\sqrt{\text{m}}$. Associated with these parameters is a characteristic cohesive zone size $\delta_c \approx E_m\phi_n/\sigma^2_{coh}$, which is 50 nm for the parameters used here. Since $\delta_c/a \ll 1$, the problems studied here are in the regime of small scale yielding. In addition, the numerical mesh size near the crack tip needs to resolve the length δ_c and so we use a mesh of size 17 nm.

3.2 Results

The presence of the elastic particle influences crack growth due to the effects of (i) the modulus mismatch on the driving force for crack growth; (ii) the change in the evolution of plasticity in the vicinity of the crack tip; and (iii) the blocking of slip at the particle−matrix interface. Here, these effects are investigated separately and

Table 3.1: The three materials analysed.

Material	E_p/E_m	Particle	Dislocation active
A	1	No	N/A
B	1	Yes	No
C	5	Yes	Yes

sequentially by considering the three cases summarized in Table 3.1: (i) material A, an initially-cracked single crystal, which should thus show only small crack effects; (ii) material B, a particle with the same elastic properties as the matrix, $E_p = E_m$ and $\nu_p = \nu_m$ but no dislocation activity in the particle, which should show the effects of slip blocking only; and (iii) material C, a particle that is elastically stiffer than the matrix, $E_p = 5E_m$ but with $\nu_p = \nu_m$, which should show the effects of modulus mismatch and slip blocking acting together. To explore the influence of the specific distribution of sources and obstacles on the response, calculations were carried out for two sets of random distributions having the same densities of sources and obstacles but different specific spatial positions and referred to as, for instance, material $B^{(j)}$ for (j=0,1).

3.2.1 Elastic response

To calibrate our subsequent results on crack growth into plastic materials, we first investigate crack growth into an elastic matrix with no dislocations. These calculations demonstrate the effects of modulus mismatch and crack size versus particle size on the crack growth behavior, which will then be modified when plasticity in the matrix is permitted. For large cracks a/L_p, the critical stress intensity for crack growth should be independent of the particle properties. Fig. 3.3 shows the normalized stress

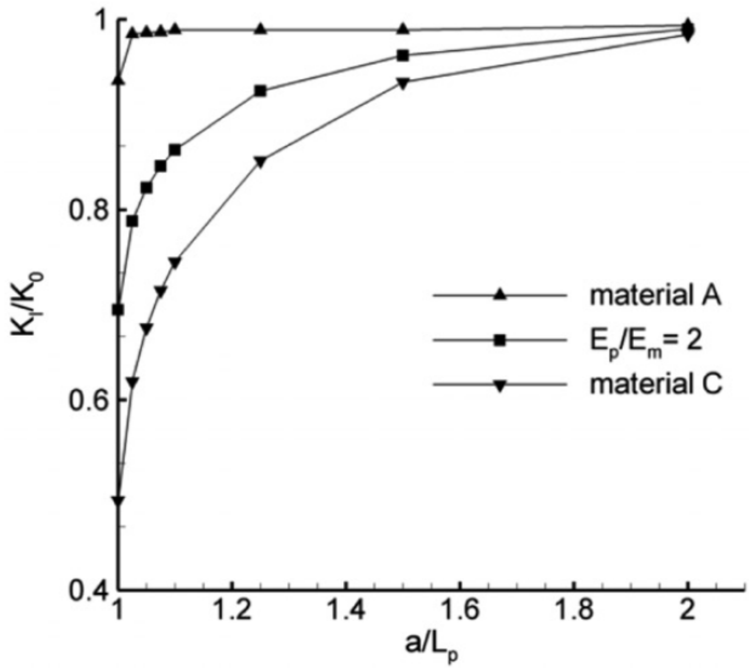

Figure 3.3: Normalized stress intensity for the onset of fracture as a function of initial crack size a for several values of the elastic modulus ratio.

intensity for crack growth (i.e. the so-called R-curve) as a function of the crack size a for several values of the elastic modulus ratio. For a modulus ratio of unity, the crack begins to grow at K_I/K_0=0.935 but after a short amount of growth reaches a value of K_I/K_0=0.985. The onset at 0.935 is attributed to truncating the cohesive relation behind the initial crack tip location and the saturation value of 0.985, just slightly below 1.0, is due to mesh resolution in the cohesive zone. For particle elastic moduli exceeding that of the matrix, crack growth occurs well below K_I/K_0=0.985, with the onset of fracture at K_I/K_0=0.68 for E_p/E_m=2 and K_I/K_0=0.48 for E_p/E_m=5. An uncracked high modulus particle would carry higher stresses than the matrix and thus, when cracked, increases the local crack-tip stress intensity $K_I^{(loc)}$ and lowers the applied stress intensity K_I needed to start fracture. The stress intensity for fracture increases rapidly with increasing initial crack size, relative to the particle size, for cracks up to $\approx a/L_p$=1.2, after which there is a slower increase to the asymptotic value of 0.99. The effect of the cracked particle is thus most significant within 20% of the particle diameter. Thus, elastic modulus mismatch alone provides a significant decrease in fracture resistance and this will also manifest itself in the plastic response under monotonic and cyclic loading.

The above results allow for a calculation of the local stress intensity factor $K_I^{(loc)}$ as a function of the crack size a or crack extension Δa as follows. The local stress intensity factor can be written as $K_I^{(loc)} = f(a)K_I$ where $f(a)$ is a function of crack length. For a homogeneous elastic material in small scale yielding, $f(a) = 1$ and so fracture in the single crystal material occurs when $K_I^{(loc)} = K_I = K_{IC} \approx 0.985K_0$, independent of crack length a. With elastic mismatch, the local stress intensity factor differs from the remote stress intensity factor but at fracture $K_{IC}^{(loc)} = 0.985K_0$ must still hold. Thus, the critical applied stress intensity factor $K_{IC}(\Delta a)$ shown in Fig. 3.3 satisfies $0.985K_0 = f(\Delta a)K_{IC}(\Delta a)$. Solving for $f(\Delta a)$ and substituting, we find the normalized local stress intensity factor in terms of the critical applied stress intensity factor as $K_I^{(loc)}/K_0 = 0.985K_I/K_{IC}(\Delta a)$. Fig. 3.3 for $K_{IC}(\Delta a)$ thus provides a master curve for relating the local and applied intensity factors.

3.2.2 Monotonic loading

A uniform displacement rate $\dot{U}(t)/H = 100/\mathrm{s}$ was imposed, chosen to reduce the computing time required. Under monotonic loading, it was previously found that varying the loading rate by two orders of magnitude did not qualitatively change the crack growth behavior, although a strong tendency was found for increased plastic deformation at lower loading rates (Cleveringa et al. (2001)). The predicted K_I/K_0

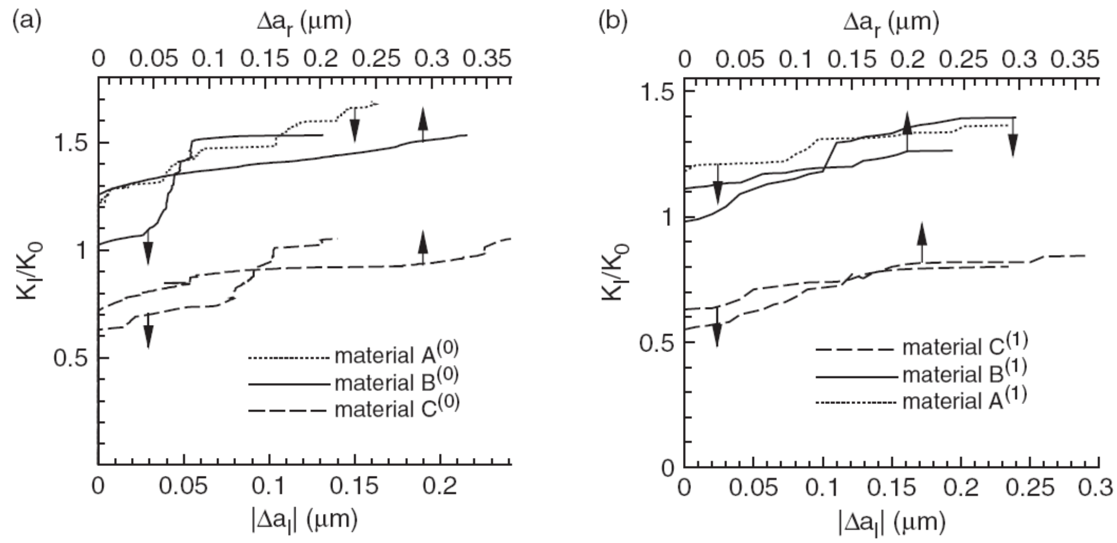

Figure 3.4: Normalized stress intensity K_I/K_0 versus crack extension under monotonic loading. (a) Materials A$^{(0)}$, B$^{(0)}$ and C$^{(0)}$; (b) Materials A$^{(1)}$, B$^{(1)}$ and C$^{(1)}$. The superscripts (0) and (1) refer to realizations 1 and 2, respectively.

versus crack extension are shown in Fig. 3.4(a, b), for materials A$^{(j)}$, B$^{(j)}$ and C$^{(j)}$ with j=0, 1. The superscripts (0) and (1) refer to realizations 1 and 2 of random distributions of dislocation sources/obstacles. Here and subsequently the crack tip location is taken to be the point along the cohesive surface where $\Delta_n = 4\delta_n$. In Fig. 3.4(a), (b), Δa_r is the crack growth in the $+x_1$-direction and Δa_l is the crack growth in the $-x_1$-direction. In all three cases, the amount of crack growth is different for the two crack tips. One reason for this asymmetry is simply that the distribution of sources and obstacles is not symmetric about x_2=0 and another is due to the extreme sensitivity of the dislocation dynamics to small perturbations (Deshpande et al. (2001a)). For the single crystal, material A, crack growth only occurs in the

$-x_1$-direction over the loading range shown. However, the values of $K_I/K_0 \approx 1.20$ at which crack growth initiates at the left crack tip are in good agreement with previous values (Deshpande et al. (2003a)). For material B, where the presence of the particle blocks slip but with no modulus mismatch, crack growth occurs at both crack tips, initiating first on the left at K_I/K_0 $\approx$0.98$-$1.02 and subsequently on the right at K_I/K_0 $\approx$1.1$-$1.26. In material C, where there is a modulus mismatch, the crack growth initiation values are K_I/K_0 $\approx$0.63 and K_I/K_0 $\approx$0.55$-$0.72 for the left and right crack tips, respectively. Thus, both the change in dislocation structure and the stress concentration induced by an elastic mismatch between the particle and the matrix promote the initiation of crack growth.

Normalizing the onset of crack growth in the plastic material by the value obtained in the elastic material (Fig. 3.3) helps to highlight the role of slip blocking by the particle. For material A, the ratio is 1.2/0.94=1.28, for material B the ratios for the left and right crack tips are, on average, $\approx$1.06 and $\approx$1.30, respectively. For material C, the ratios for the left and right crack tips are, on average, both about 1.31. These results suggest that elastic stress concentrations dominate the material response, with slip blocking playing a lesser role. In addition, slip blocking appears more important in driving crack growth for the matched-modulus particle as compared to the higher modulus particle, which responds similarly to the single crystal material when the elastic stress concentration is normalized out. The dislocation distributions for materials $A^{(0)}$, $B^{(0)}$ and $C^{(0)}$ at K_I/K_0=1.07 are shown in Fig. 3.5, along with contours of the opening stress σ_{22}. In Fig. 3.5(a) no particle is present, but for comparison purposes the region occupied by the particle in materials B and C is marked by dashed lines. The stress above the crack is relaxed and dislocations are present in the region above the crack. The difference between the stress distribution and dislocation structure at the two crack tips is evident. Evidence for the sector structure of the stress field as given by the continuum slip solution of Rice (1987a) can be seen. When a particle is present and dislocation glide is blocked, Fig. 3.5(b), the same stress distri-

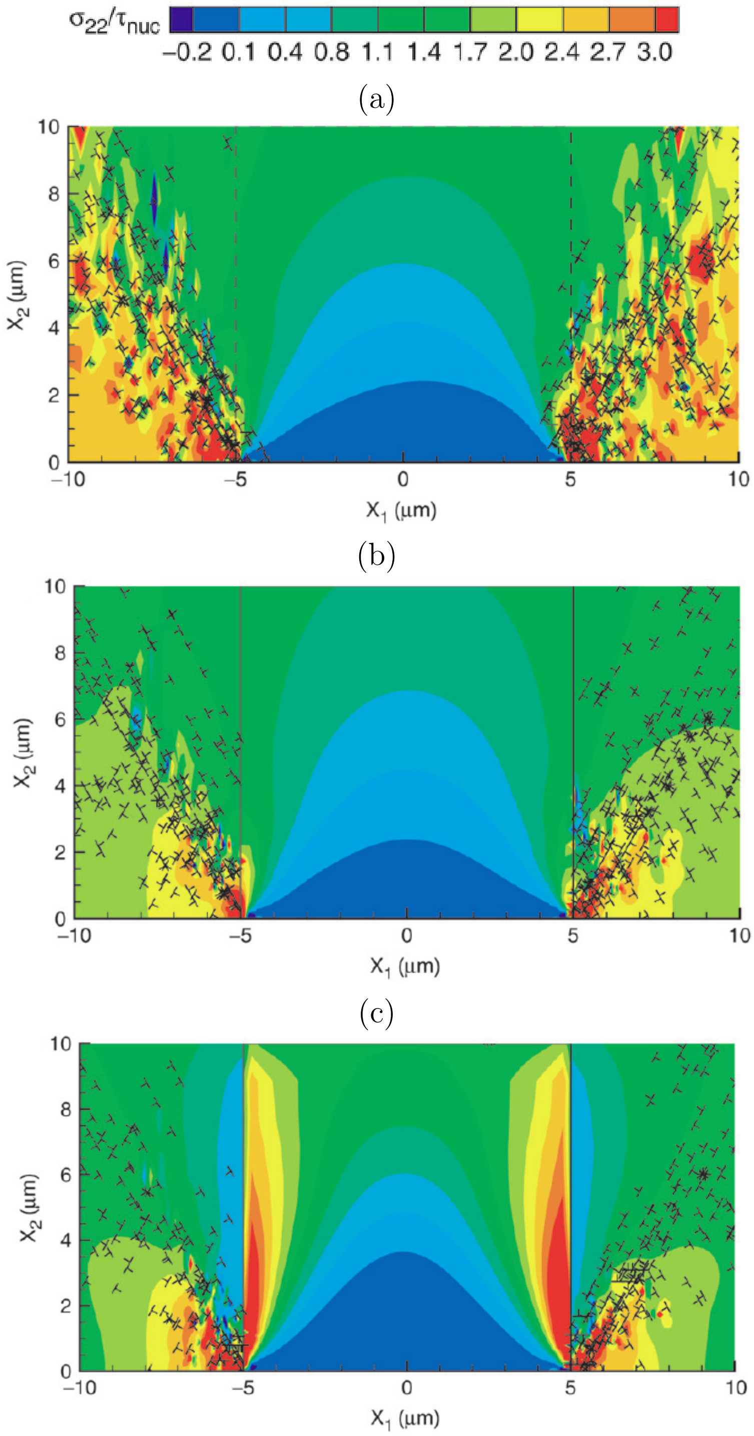

Figure 3.5: Contours of the normalized normal stress, σ_{22}/τ_{nuc}, and dislocation distributions under monotonic loading at K_I/K_0=1.07; (a) Material A$^{(0)}$ (b) Material B$^{(0)}$ (c) Material C$^{(0)}$.

bution is obtained as in the single crystal, albeit with slightly higher stress gradients in the matrix near the two crack tips. With an elastic mismatch between the particle and the matrix, Fig. 3.5(c), high stresses develop along the particle−matrix interface. In this case, the sector stress field structure is lost and the stress concentration in the particle increases and the stress gradients in the matrix near the two crack tips is greater. Moreover, with no elastic mismatch, more dislocations accumulate at the particle−matrix interface than when there is the elastic mismatch.

3.2.3 Fatigue loading

The same three sets of material parameters are used in the cyclic loading calculations as in the monotonic loading calculations in Section 3.2.2. The only difference is in the time dependence of the applied displacement $U(t)$ corresponding to applied σ_{22} which has the form sketched in Fig. 3.2(c). All calculations are carried out with a displacement rate $\dot{U}/H$=100 /s and thus the variation of the cyclic loading amplitude is obtained by increasing or decreasing the frequency of loading between 3.3 MHz and 8 MHz to obtain the desired range of cyclic loading amplitudes. The applied loading is characterized by the stress intensity factor K_I, with the stress varied between σ_{min} and σ_{max} and the corresponding stress intensity factor range $\Delta K = K_{max} - K_{min}$. The load ratio, $R = \sigma_{min}/\sigma_{max}$ is fixed at 0.3.

The DD calculations show fatigue crack growth above a threshold value of ΔK. The crack growth shows a range of behaviors, and we first comment qualitatively. Fig. 3.6 shows the computed crack advance, Δa, versus the number of cycles for ΔK_I near the fatigue threshold found for each material. As for monotonic loading, the crack advance is not symmetric, but it differs from the monotonic loading case. Although crack growth to the left occurs at lower K_I values under monotonic loading, under cyclic loading no crack advance occurs to the left in material A$^{(0)}$ while some growth does occur in materials B$^{(0)}$ and C$^{(0)}$, but stopping after eight cycles and $|\Delta a_l| \approx 0.05\mu$m in material B$^{(0)}$ and after 12 cycles and $|\Delta a_l| \approx 0.10\mu$m in material

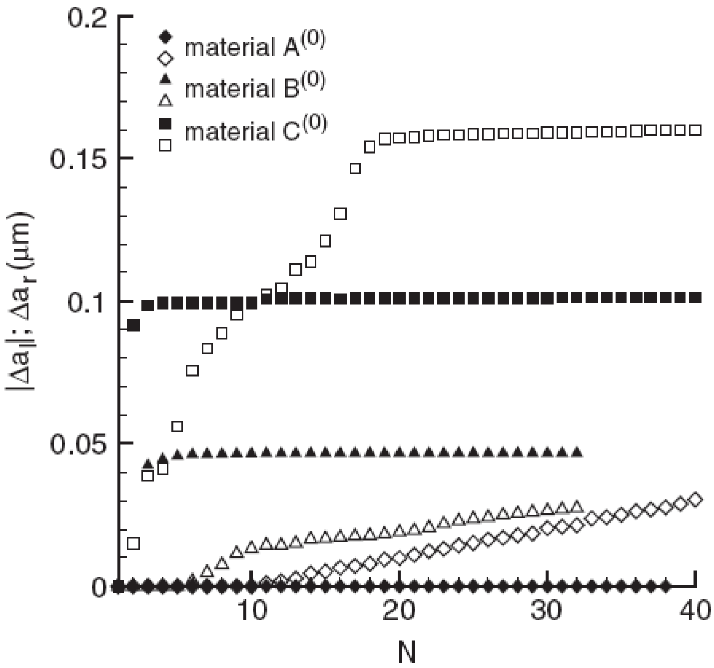

Figure 3.6: Crack advance versus number of cycles. The filled symbols are related to the left crack tip and unfilled symbols are related to the right crack tip. K_I/K_0=0.775, 0.595 and 0.395 for materials $A^{(0)}$, $B^{(0)}$ and $C^{(0)}$, respectively. The superscript (0) refers to realization 1.

$C^{(0)}$. Crack growth to the right, more difficult under monotonic loading, occurs more readily under cyclic loading. In material $A^{(0)}$, $|\Delta a_r|$ begins to increase after 10 cycles at a nearly constant rate. In material $B^{(0)}$, $|\Delta a_r|$ begins to increase after seven cycles at a slightly faster rate than for material $A^{(0)}$, slowing to a lower rate after 10 cycles. In material $C^{(0)}$, $|\Delta a_r|$ shows two distinct regimes: (i) during the first 18 cycles, $|\Delta a_r|$ increases at a rate close to 0.008 μm /cycle; and (ii) between cycle 19 and 40, $|\Delta a_r|$ the rate decreases to a very low rate of about 10^{-4} μm/cycle. The normalized opening stress, σ_{22}/τ_{nuc}, and dislocation distribution are shown in Fig. 3.7 in a region around the cracked particle. For material $A^{(0)}$, dislocations can glide into the material above the crack and relax the stress field. For materials $B^{(0)}$ and $C^{(0)}$, dislocation glide is blocked in the particle, which gives rise, even with no elastic mismatch, to an increased stress concentration above the crack tip that increases with increasing particle modulus. The different stress and dislocation distributions in the vicinity of

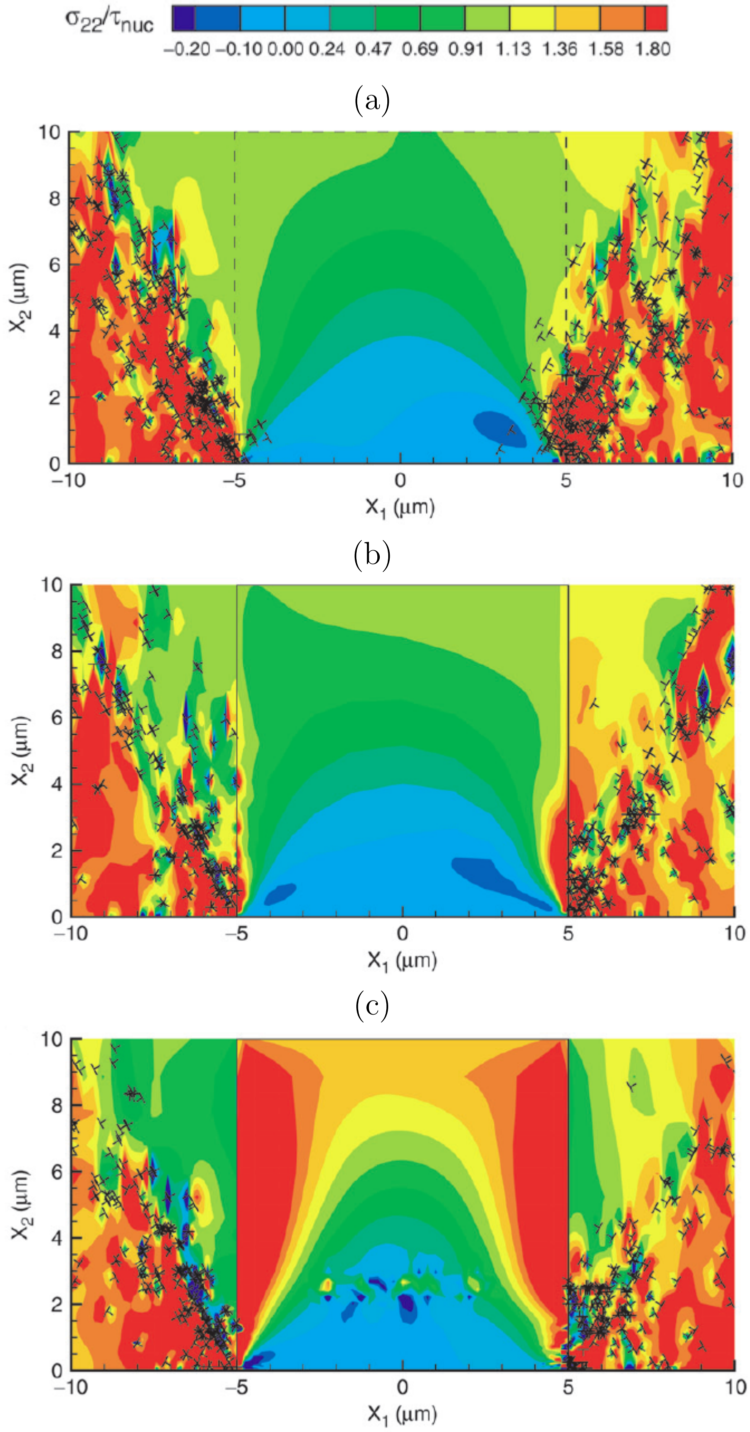

Figure 3.7: Contours of the normalized normal stress, σ_{22}/τ_{nuc}, and dislocation distributions. (a) Material A$^{(0)}$ with $\Delta K_I/K_0$=0.775 (b) Material B$^{(0)}$ with $\Delta K_I/K_0$=0.595 (c) Material C$^{(0)}$ with $\Delta K_I/K_0$=0.395.

the left and right crack tips, which are largely due to the different source and obstacle locations, can also be seen in Fig. 3.7. In comparison to Fig. 3.5, the dislocation distribution under cyclic loading is more concentrated along a 60° slip plane near the right crack tip and along a 120° slip plane near the left crack tip.

3.2.4 Fatigue crack growth rate

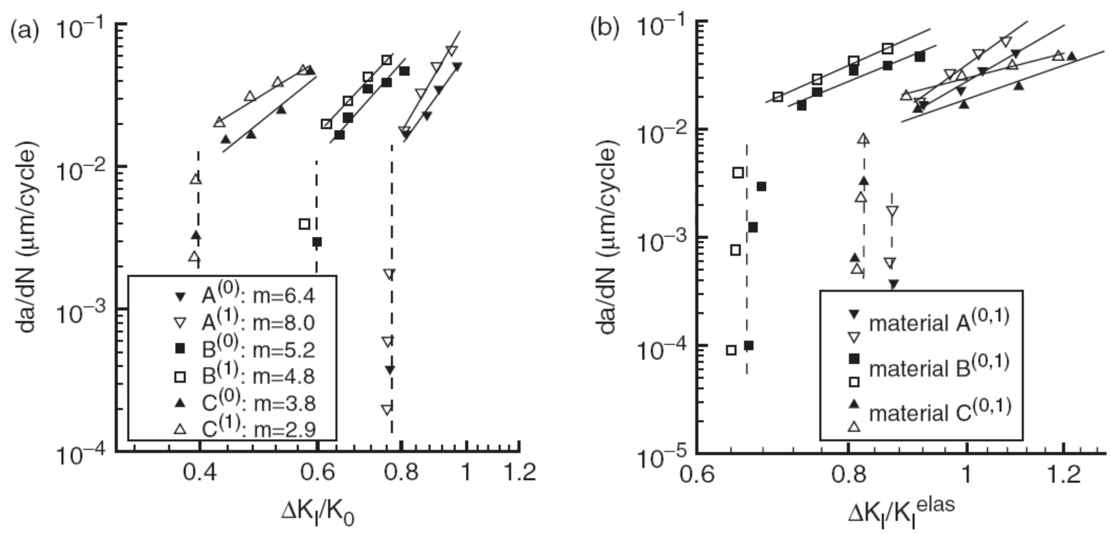

Figure 3.8: (a) Cyclic crack growth rate versus $\Delta K_I/K_0$ for the Mode-I cyclic loading. For materials $\mathrm{A}^{(0,1)}$ and $\mathrm{B}^{(0,1)}$, the crack growth rate represents an average of the crack advance over 10 and 20 cycles for the low and high value of $\Delta K_I/K_0$, respectively. For materials $\mathrm{C}^{(0,1)}$, the crack growth rate represents an average of the crack advance over the number of cycles needed for the crack to reach the critical distance. (b) Cyclic crack growth rate versus $\Delta K_I/K_I^{elastic}$ for the Mode-I cyclic loading. Filled symbols: material $\mathrm{A}^{(0)}$, $\mathrm{B}^{(0)}$, $\mathrm{C}^{(0)}$; open symbols: material $\mathrm{A}^{(1)}$, $\mathrm{B}^{(1)}$, $\mathrm{C}^{(1)}$. m is a Paris exponent

The crack growth rate $\log(\mathrm{d}a/\mathrm{d}N)$ versus the normalized loading $\log(\Delta K_I/K_0)$ for R=0.3 is shown in Fig. 3.8(a) for materials $\mathrm{A}^{(j)}$, $\mathrm{B}^{(j)}$ and $\mathrm{C}^{(j)}$ with j=0, 1, for crack growth on the right side. The crack growth rate is an average of the crack advance over the number of cycles computed. For materials $\mathrm{A}^{(j)}$ and $\mathrm{B}^{(j)}$ the average is over at least 10 cycles for ΔK_I values above the threshold and over 20 cycles for near-threshold values of ΔK_I. As noted above, for material C, the crack growth rates drop dramatically after crack extension exceeds a critical amount Δa_{crit} and so the values of da/dN in Fig. 3.8(a) for materials C$^{(0)}$ and C$^{(1)}$ are averages over the number of cycles needed for the crack to grow to Δa_{crit}. The fatigue threshold is estimated using the procedure in Deshpande et al. (2002) wherein calculations are carried out at decreasing values of ΔK_I until the crack growth rate da/dN is less than or equal to $10^{-2}\mu$m/cycle (10 times larger than used in Deshpande et al. (2002)). The fatigue threshold is then taken as the average of the last two values of the applied ΔK_I. Above the threshold, the crack growth rates are fit to a Paris power-law Paris et al. (1961) of the form

$$\frac{\mathrm{d}a}{\mathrm{d}N} = C_I \left(\frac{\Delta K_I}{K_0}\right)^m \tag{3.3}$$

where m is the Paris exponent and C_I a constant. The fatigue threshold is reduced in the presence of a particle, and further reduced with an increased modulus mismatch. The thresholds are $\approx 0.78K_0$ for material A, $\approx 0.59K_0$ for material B, and $\approx 0.40K_0$ for material C, with only a small difference seen for the two distributions of dislocation sources and obstacles used in the calculations. The Paris exponent decreases when a particle is present, and furthermore decreases with increasing mismatch, as indicated by Fig. 3.8(a). There is a somewhat greater sensitivity of the crack growth in the power-law regime to the specific realization which, although not large in magnitude, leads to a significant variation in the Paris exponent m. Keeping in mind that the crack in material C stops after a critical distance, these results show that a particle reduces the threshold for fatigue but decreases the rate of the crack growth rate. We

Table 3.2: Numerical results for crack growth from a cracked particle, under monotonic loading for an elastic matrix and elasticplastic one and under cyclic loading. The index j refers to the realization number.

	Monotonic		Cyclic		
Materials	$K_I^{elastic}/K_0$	K_I/K_0	$\Delta K_I^{th}/K_0$	K_{max}^{th}/K_0	m
A$^{(j)}$	0.94	$\gg 1.22$	0.78	1.10	6 - 8
B$^{(j)}$	0.94	1.03 - 1.26	0.59	0.83	4 - 6
C$^{(j)}$	0.48	0.62 - 0.72	0.40	0.57	2 - 4

summarize salient values for the various material responses in Table 3.2. For cyclic loading at the fatigue threshold, the maximum stress intensity factor K^{th}_{max} is smaller than the stress intensity factor K_I obtained for the monotonic loading, and larger than the elastic value $K_I^{elastic}$ for materials A and C but smaller than $K_I^{elastic}$ for Material B. The dislocations thus shield the crack tip under monotonic loading, but the dislocation structures formed under cyclic loading provide less shielding. The net shielding remains positive for materials A and C, because the threshold remains above $K_I^{elastic}$, but is actually negative for Material B (anti-shielding). Net anti-shielding in fatigue has also been seen by Pippan and Weinert (1998).

We now evaluate the fatigue results to attempt a decoupling of elastic and plastic effects on the fatigue crack growth. To do so, we first normalize the fatigue crack growth data against the critical stress intensity for crack growth in the elastic matrix problem (e.g. Fig 3.3), $\Delta K_I/K_I^{elastic}$, as shown in Fig. 3.8(b). Since $K_I^{elastic} \approx K_0$, the results for materials A and B are changed only slightly. However, the $\mathrm{d}a/\mathrm{d}N$ versus ΔK_I curves for material $\mathrm{C}^{(j)}$ shift upward substantially, with the normalized fatigue threshold $\Delta K_I/K_I^{elastic}$ of material $\mathrm{C}^{(j)}$ being comparable to that of material $\mathrm{A}^{(j)}$. These results again indicate that slip blocking gives an anti-shielding effect for both monotonic and fatigue crack growth and that elastic mismatch increases the local stress intensity at the crack tip but the dislocation structures formed by the slip blocking and image stress fields cause shielding of the crack tip under both monotonic and cyclic loading conditions. Recall that crack growth in materials B, C can be abruptly halted after growth out to a critical distance. We now examine this further. The crack growth rate as a function of the crack advance is plotted in Fig. 3.9(a) for material $\mathrm{B}^{(0)}$, in Fig. 3.9(b) for material $\mathrm{C}^{(0)}$ for values of the cyclic amplitude around the fatigue threshold, and in Fig. 3.9(c) for materials $\mathrm{C}^{(0)}$ and $\mathrm{C}^{(1)}$ for several values of the cyclic amplitude ΔK_I in the Paris power-law regime. Below the fatigue threshold, the crack growth rate versus crack advance is similar in materials $\mathrm{B}^{(0)}$ and $\mathrm{C}^{(0)}$ and, as noted previously, drops dramatically after a critical crack advance. For

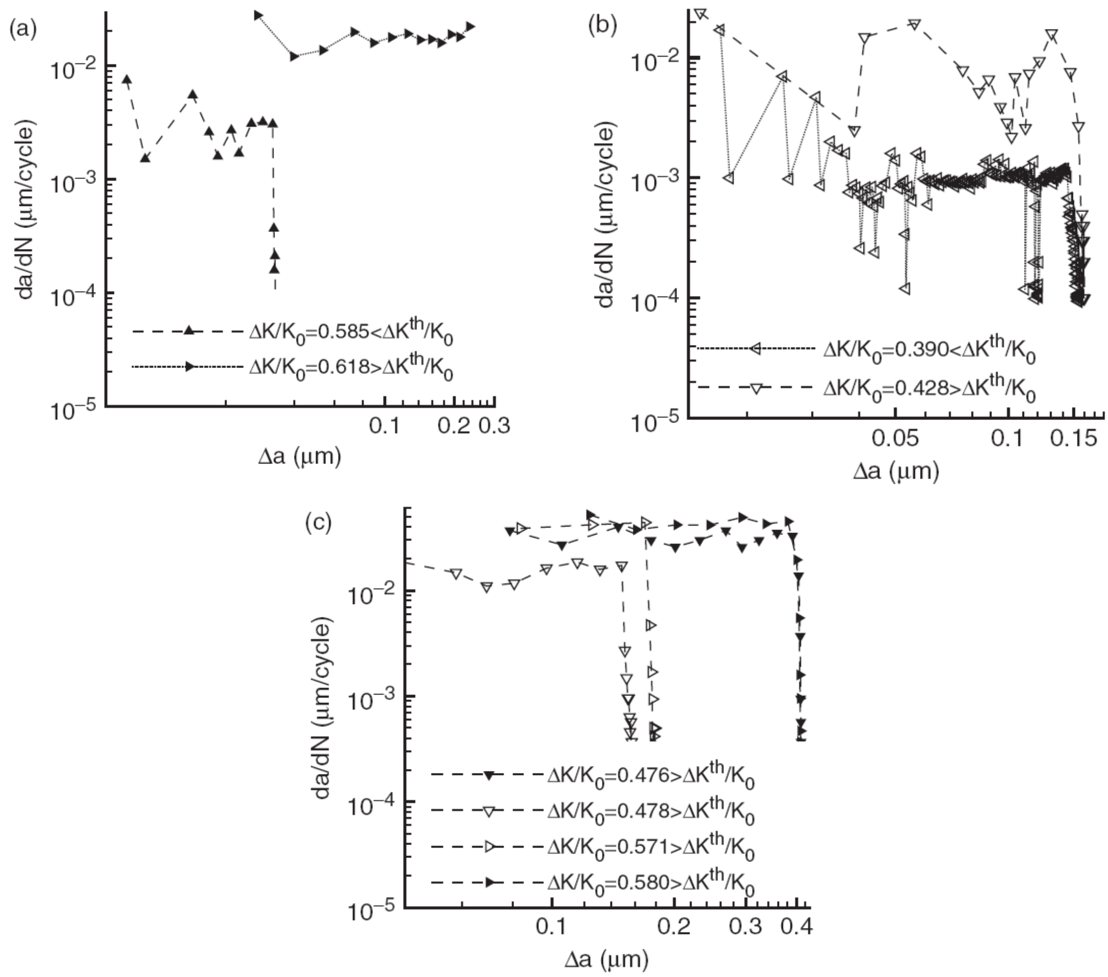

Figure 3.9: Crack growth rate versus crack advance for (a) material B$^{(0)}$ and (b) material C$^{(0)}$ around the fatigue threshold, and for (c) materials C$^{(1)}$ (filled symbols) and C$^{(0)}$ (unfilled symbols) for several values of ΔK_I in the Paris regimes.

material B$^{(0)}$, Δa_{crit}=0.033μm, while it is much larger at Δa_{crit}=0.15 μm in material C$^{(0)}$ and Δa_{crit}=0.40 μm in material C$^{(1)}$, showing sensitivity to the source/obstacle distributions. Above the fatigue threshold, the crack growth is qualitatively different, still dropping dramatically in material C$^{(0)}$ after a critical distance while being nearly constant in material B$^{(0)}$.

We believe the reason that cracks stop growing is that the local stress intensity amplitude $\Delta K_I^{(loc)}$ driving growth is decreasing with crack growth due to either changes in slip blocking or elastic mismatch effects, or both, and can decrease below a threshold value $\Delta K_I^{(loc)th}$. Since for larger crack growth, we expect that the crack growth rates for materials A, B, and C will converge, the existence of a unique threshold is not unreasonable, and so we consider $\Delta K_I^{(loc)th}$ to be a material parameter. We envision that the $\Delta K_I^{(loc)}$ is increased, relative to the applied ΔK_i, by (i) a slip blocking contribution ΔK_I^{sb} and (ii) the elastic stress concentration factor found previously for elastic fracture, $0.985\Delta K_I/\Delta K_{IC}(\Delta a)$, so that

$$\Delta K_I^{(loc)} = \frac{0.985K_0\Delta K_I^{th}}{\Delta K_{IC}(\Delta a)} + \Delta K_I^{sb} \tag{3.4}$$

With a threshold $\Delta K_I^{(loc)th} = \frac{0.985K_0\Delta K_I}{\Delta K_{IC}(\Delta a)} + \Delta K_I^{sb}$, a crack loaded at ΔK_I will halt after an amount of crack growth Δa satisfying Eq. 3.4. For material A, the local and applied stress intensity amplitudes are equal, $\Delta K_I^{(loc)} = \Delta K_I$ and so we can immediately estimate $\Delta K_I^{(loc)th} = 0.78K_I$. Then, for material B with no elastic stress concentration, we have $\Delta K_I^{(loc)th} = \Delta K_I^{th} + \Delta K_I^{sb}$ and so can estimate $\Delta K_I^{sb} = \Delta K_I^{(loc)th} - \Delta K_I^{th}$ since $\Delta K_I^{th} = 0.59K_0$ for material B. For material C, both slip blocking and an elastic stress concentration play a role and lead to crack growth at lower applied loads but with halting of the crack after larger amounts of growth. For material C we account for the elastic stress concentration through the factor $f(a)$ and so can estimate the slip blocking as $\Delta K_I^{sb} = \Delta K_I^{(loc)th} - 0.985K_0\Delta K_I/\Delta K_{IC}(\Delta a)$ using the measured values of ΔK_I and Δa at which cracks stop. Table 3.3 summarizes the results of this analysis on materials A, B, C. The estimated slip blocking for material C is generally smaller than for material B and decreases at higher applied ΔK_I. In one case, the estimated slip blocking becomes negative. This suggests that the slip blocking effect decreases as the crack grows more than a few tenths of a micron from the particle and/or is influenced by image stresses due to the particle-matrix elastic modulus mismatch. This limited influence of slip blocking is consistent with our discussion above for monotonic loading. Overall, our results are reasonably interpreted through the consideration of a $\Delta K_I^{(loc)}$ that is affected by:

(i) slip blocking, which gives an anti-shielding effect for small crack extension;

Table 3.3: Summary of the numerical analysis. Lines 4−7 refer to materials $C^{(0,1)}$ in the Paris power-law regime as given in Fig. 3.9(c).

Material	$\Delta K_I/K_0$	Δa	K_{IC}/K_0	$\Delta K_I^{(loc)th}/K_0$	$\Delta K_I^{sb}/K_0$
A	0.78	-	0.985	0.78	-
B	0.59	-	0.985	0.78	0.19
C	0.428	0.15	0.63	0.78	0.11
	0.476	0.4	0.72	0.78	0.13
	0.478	0.16	0.635	0.78	0.04
	0.571	0.18	0.64	0.78	-0.10
	0.580	0.4	0.72	0.78	-0.01

(ii) elastic mismatch, which gives a stress concentration that decreases with crack growth;

(iii) interactions between the above two factors, which influences the dislocation structure that develops, and is reflected in fluctuations of the estimates above.

The first two factors act to reduce the value of the applied ΔK_I necessary to initiate and continue fatigue crack growth, relative to a single crystal material.

3.3 Discussion

A number of prior studies exist on the role of particles in modifying fatigue crack growth in metals. Based on a continuum crystal plasticity model, Bruzzi et al. (2001) estimated the state of stress within the matrix and incorporated the stress gradient along a predefined crack path into investigation of the effect of reinforcing particles on a small fatigue crack, Bruzzi and McHugh (2004). The existence of such a gradient of stress is important because it increases the driving force at the crack tip and thus accelerates the crack growth close to the interface, Pippan et al. (2000), Wang and Siegmund (2006). We see the same effect here when there is elastic mismatch, while slip blocking may add an additional contribution. Jiang et al. (2003) experimentally studied fatigue crack propagation normal to an elastically-matched but plastically mismatched bimetallic interface under a four-point bending condition. They observed fatigue crack acceleration over a few tenth of micrometers beyond the interface when the crack propagated from a hard (high yield stress) phase into a soft (lower yield stress) phase, followed by a reduced growth. A similar result was obtained numerically by Wang and Siegmund (2006) using a cohesive framework to model crack propagation through an elastically-matched, plastically-mismatched interface. These results are qualitatively similar to our results for material B, except that our hard phase is strictly elastic. In contrast to the continuum framework, however, we observe fatigue with maximum loads below the elastic fracture limit, indicating short-crack and discrete plasticity effects. We also observe stochastic effects such as asymmetry in the crack growth, and a sensitivity of the growth rates and loads to the distribution of obstacles and sources. The fatigue threshold and the crack growth rate characterize the propagation of a crack during a fatigue experiment. From the literature, it appear that the only common feature is that fatigue crack growth behavior is different for single and multiphase materials, and that an increase or a decrease of the fatigue threshold is strongly dependent on the material properties Narasaiah and Ray (2006). Tanaka et al. (2000) present results showing that ΔK_I^{th} tends to be larger for reinforced as compared to unreinforced alloys at the maximum tensile stress level. Such an increase of the fatigue threshold in presence of reinforcements is also observed by Milan and Bowen (2004) in the case of an Al matrix reinforced by different volume fraction of SiC particles. On the other hand, for 16% and 21% Al_2O_3 particle reinforced aluminium alloys, Pippan and Weinert (1998) conclude experimentally that the fatigue threshold of the particle reinforced alloy is smaller than the one obtained for the unreinforced material, in agreement with this study. Literature data further suggest that the presence of reinforcements tends to increase the crack growth resistance (inverse of the Paris exponent) as compared non-reinforced material. Chen et al. (2001) concluded that the crack growth rate decreases with increasing particle size. Milan and Bowen (2004) characterized separately the crack growth resistance of unreinforced and reinforced aluminium alloys, concluding that the addition of SiC particles increases the fatigue crack growth resistance at near threshold and Paris-power law regimes. This latter effect of reinforcement on the crack growth resistance is reproduced by the calculations presented in this study. The reduced Paris exponent may be attributable to the higher dislocation density close to the crack and particle in material C as compared to material B (Fig. 3.7(b,c)) because an increase in plastic dissipation tends to decrease the Paris exponent in ductile materials, Suresh (1998).

3.4 Conclusions

Crack growth from small initially-cracked elastic particles into a ductile metal material has been analyzed using discrete dislocation plasticity to characterize the inelastic deformation in the matrix at micron-scales and using a cohesive model for fracture. Analysis of crack growth under fatigue loading reveals the following general features:

- The particle reduces the threshold value of ΔK and the Paris power-law exponent, relative to a single crystal material.
- Slip blocking at the particle−matrix interface gives rise to a dislocation structure with increased anti-shielding relative to the single crystal material.
- Stress concentrations due to elastic mismatch increase the local stress intensity factor further and thus reduce the applied stress intensity factor at which crack growth is observed.
- The elastic stress concentrations decay with increasing crack length, leading to halting of crack growth near and above the threshold value of ΔK after some critical distance of crack growth.

Chapter 4

Fracture in Plastically Anisotropic Metals

The dislocation core structure in an atomic lattice dictates that a finite stress, the Peierl stress, is required to move a dislocation through the perfect lattice Nabarro (1947). Experiments Caillard (2010), Castany et al. (2007), Kruml et al. (2002), Spence and Koch (2001) and many computer simulations Aubry et al. (2011), Khater and Bacon (2010), Nogaret et al. (2010), Leyson et al. (2010), Xiang et al. (2008), Tapasa et al. (2007) demonstrate these atomic effects in a variety of materials. In FCC materials, the Peierls stress is generally low and, given the many identical slip systems, the initial plastic flow stress is fairly isotropic. In HCP systems, the Peierls stress varies widely among slip systems, with basal and/or prism slip being relatively easy, similar to FCC systems, but pyramidal slip being far more difficult, leading to significant plastic anisotropy. In BCC Fe, the lattice resistance for screw dislocations is particularly high, with dislocation motion occurring due to double-kink nucleation and spreading at the atomic scale. Due to the atomic nature of the Peierls stress, modeling of dislocations at larger scales usually treats the Peierls stress as a "friction" stress - i.e. a constant background resistance to dislocation motion - within a dislocation mobility law Kubin et al. (1992), Hirsch et al. (1997), Kubin et al. (1998), Chen et al. (2003). The influence of mobility on fracture has been probed mainly in conjunction with the brittle-ductile transition (BDT) where dislocations can shield or anti-shield the crack tip, influencing cleavage and crack-tip dislocation emission (Hirsch et al. (1997)), with kinetic effects due to the dislocation glide mobility as a function of temperature. At the continuum scale, the Peierls stress and dislocation mobility enter indirectly through a rate-dependent flow stress, and plastic anisotropy is captured using crystal plasticity. However, these conventional plasticity models possess no internal length scales and so do not predict fracture when the yield stress is too low or the underlying material cohesive strength is too high (Tvergaard and Hutchinson (1993), Tvergaard (2001)). Dislocation-based models for fracture demonstrate some limitations of the continuum models (Van der Giessen and Needleman (1995), Cleveringa et al. (1997, 1999, 2000), Van der Giessen et al. (2001), Deshpande et al. (2003a), Nicola et al. (2005), O'Day (2005), Chakravarthy and Curtin (2010b,a, 2011a)) and recent work by one of these authors indicates that fracture toughness depends on the dislocation obstacle spacing, which is an internal material length scale absent from traditional plasticity models.

Here, we extend the prior work on dislocation-based fracture modeling to include the effects of both a Peierls stress and plastic anisotropy. We are motivated by recent work on the fracture of single-crystal Zn by Catoor and Kumar (2008). In that study, crack growth along the basal plane was studied for two crack growth directions, $[2\bar{1}\bar{1}0]$ (orientation 1) and $[10\bar{1}0]$ (orientation 2), and complementary FEM crystal plasticity simulations were performed. In orientation 1, one basal slip system and two symmetric pyramidal slip systems are active. In orientation 2, two basal slip systems and four symmetric pyramidal slip systems are active but, due to their symmetric arrangement with respect to the crack front, the out-of-plane plastic displacements due to dislocations cancel and it is possible to evaluate this orientation as an "in-plane" problem, assuming latent hardening effects are minimal. The in-plane/projected Burgers vector and resolved shear stress driving pyramidal dislocation motion is considerably smaller in orientation 2 than in orientation 1, indicating a higher in-plane flow stress for orientation 2, and thus a higher applied Mode-I stress intensity to initiate and continue plastic flow around the crack tip. The FEM simulations indicate that the accumulated total plastic strain due to pyramidal slip is indeed smaller in orientation 2 as compared to orientation 1, while the plastic strain due to basal slip is independent of orientation. Experimentally, orientation 2 shows lower toughness, which was rationalized by Catoor and Kumar (2008) by considering a maximum crack tip opening stress criterion for crack growth, and ignoring any influence of basal slip on this opening stress. The FEM models did not allow crack growth, and so could not be compared directly with the experimental crack growth results. The effect of basal/pyramidal interaction on crack growth thus remains open, and modeling of crack growth in such plastically anisotropic systems has not been investigated. One goal here is to examine the effect of in-plane Burgers vector and in-plane Peierls stress on the fracture in materials with plastic anisotropy in the basal/pyramidal Peierls stress.

The experimental observations in Catoor and Kumar (2008) also show that new basal-plane microcracks can nucleate a few microns away from the existing crack tip. Subsequently the ligament formed between the macro and micro cracks can retard the crack growing until the ligament is sheared off. A number of prior experiments studying microcrack initiation in pure Zn single crystal also exist. Deruyttere and Greenough (1956) and Gilman (1958) showed that plastic slip on the basal plane can reduce the cleavage resistance of initially-uncracked Zn single crystals, with the critical normal stress depending on the amount of prior basal plastic slip. Parisot et al. (2004) investigated cleavage fracture in Zn coated steel sheet under equibiaxial expansion, plane strain tension, and simple tension, and obtained a critical basal normal stress to initiate cleavage. These studies consider only dislocations on basal planes, although Stofel (1962) pointed out that pileups of dislocations on basal planes cannot provide a general explanation for fracture initiation in Zn single crystal. Stofel thus proposed a fracture initiation model based on the interaction of basal and non-basal edge dislocations. A second goal here is to shed light on possible microscopic origins of this basal microcrack nucleation.

To gain insight into the role of plastic anisotropy for the basal cleavage in HCP-like materials, we pursue here a dislocation-based study of the deformation and fracture in such systems. We first extend the standard 2d-DD models and algorithms of Van der Giessen and Needleman (1995) to include a Peierls stress, and analyze the tensile response of the DD materials to verify that the Peierls stress determines the material yield stress. We then model mode I crack growth, using a new robust DD/Cohesive-Zone (DD/CZ) model Chakravarthy and Curtin (2011a), in systems with varying Peierls stress and pyramidal/basal plastic anisotropy for cracks propagating parallel to the easy-slip basal planes. We find that the fracture toughness depends primarily on the yield stress measured normal to the crack plane and not on the plastic anisotropy, and that flow along the basal planes occurs but it does not influence crack growth. We then analyze the fracture results using the concept of stress-gradient plasticity, where a local stress gradient acting over the nucleating dislocation dipoles modifies the apparent flow stress relative to the value in the absence of a stress gradient. We show that the trends in fracture toughness obtained here for materials with flow controlled by a Peierls stress can be unified with prior results for an entirely different material in which flow stress is controlled by dislocation obstacles through the stress gradient concept. We thus demonstrate that although the physical material length scale may change from system to system, the effect of stress gradients over the operative material length scale is a strong determinant of the fracture toughness. This new insight helps unify the understanding of fracture at the discrete dislocation level. Our simulations then also show the occurrence of localized tensile stress concentrations in a several-micron-scale region around the main crack, due ultimately to the discreteness of the dislocation structures that form, and suggest an origin for the basal microcracking observed in experiments.

The remainder of this section is organized as follows. Section 4.2 briefly reviews the framework of 2d-DD modeling of plasticity and then presents the implementation of a Peierls stress model. Result for plane-strain tension of Peierls-controlled material flow are presented and discussed in Section 4.3. Simulation of Mode-I crack growth is presented in section 4.4 and the dependence on Peierls stress and plastic anisotropy is demonstrated and discussed. The unification of the present results with prior 2d-DD studies of fracture via the Stress Gradient Plasticity concept is also discussed in this section. Section 4.5 addresses the issue of microcrack nucleation. Our main conclusions are briefly summarized Section 4.6.

4.1 Peierls stress implementation

Recently, several algorithms have been developed to make the DD model robust over a wider set of material parameters as mentioned in Chapter 2. Chakravarthy and Curtin (2011a). Implementation of a Peierls stress τ_P first involves modification of the dislocation mobility law (see Eq. 2.16), by treating the Peierls stress as an internal friction in the standard manner. Specifically, the magnitude of the glide velocity v of is related to the glide force as in Eq. 2.16. Thus, after nucleation, a dislocation will not move until the Peach-Koehler force reaches $\tau_P b$. Simultaneously, there are no obstacles introduced in the material to otherwise control disocation motion or influence the macroscopic flow stress. Modifications to the nucleation algorithm are, however, necessary to avoid spurious features associated with successive nucleation of dipoles. Once a dislocation dipole is nucleated at distance $L_{nuc}/2$ on each side of the source, the shear stress on the source is $-3\tau_{nuc}$. Without a Peierls stress, the dipole quickly widens and the stress on the source decreases so that another dislocation dipole of opposite sign is *not* nucleated. With a Peierls barrier, the dislocations remain at the original positions, triggering nucleation of an opposite-sign dipole that then subsequent annihilates the original dipole, leading to no net nucleation. To circumvent this spurious situation, we extend the nucleation length to $2L_{nuc}$, and the time period to $2t_{nuc}$, so that upon nucleation of a dipole the shear stress acting on the source is

$-\tau_{nuc}$ and becomes $> -\tau_{nuc}$ in the very next load increment. With further loading, the shear stress on the source can again reach τ_{nuc} before the Peierls stress is reached in the original dislocations. Specifically, at an applied loading of $2\tau_{nuc}$, the stress on the source is τ_{nuc} and the stress on the first pair of nucleated dislocations is $2.5\tau_{nuc}$. Thus, if $\tau_P \geq 2.5\tau_{nuc}$ then a second dipole is nucleated and can artificially push the original dipole dislocations at stresses below τ_P and generate anomalous flow. Since τ_{nuc} is a statistical quantity (typically a mean of $\bar{\tau}_{nuc}$ and standard deviation $0.2\bar{\tau}_{nuc}$), it is not unusual to have $\tau_P > \tau_{nuc}$ for the weaker sources that control the flow. Hence, we introduce an absolute condition that the source cannot operate if a prior dislocation dipole remains pinned at the $+/-L_{nuc}$ positions due to the Peierls stress. We consider below tensile specimens where the basal planes are non-active slip planes with respect to the applied load. Tests reveal, however, that when a sufficient number of pyramidal dislocations are generated, the basal sources can be triggered. These basal dislocations then interact with the pyramidal dislocations and change the macroscopic flow stress. For materials where flow is controlled by obstacles, such close interactions arise infrequently so that a very small minimum interaction distance $2b$ can be used. For materials where motion is controlled only by a Peierls stress, such interactions are more frequent and cause spurious flow. We thus use a minimum interaction distance of $6b$ and largely eliminate spurious basal nucleation and its consequences.

4.2 Plane strain tension

4.2.1 Algorithms, material parameters, and validation

To verify that the algorithms discussed briefly above do lead to a material wherein the flow stress is controlled by the Peierls stress, we perform plane strain tension tests for a range of material properties. A rectangular specimen of dimensions $2W \times 2H$, with W=15 μm and H=5 μm is assigned three slip systems, at $\theta^{(1)}$=120° and $\theta^{(2)}$=60° for pyramidal planes and $\theta^{(3)}$=0° for basal planes, as shown in Fig. 4.1. The Burgers vectors are b^P for pyramidal dislocations and b^B for basal dislocations. All slip plane systems have equal slip spacing $d = 100b^B$. A uniform finite element mesh of 360×120 quadrilateral elements is used to obtain the corrective solution. The tensile direction is aligned to the x_1-axis and a prescribed displacement U at $x_1 = \pm W$ and traction free boundaries on $x_2 = \pm H$ are imposed. A time step Δt=0.05 ns is used and, unless otherwise stipulated, a loading rate of $\dot{U}/W$=2000/s is used to obtain a strain of 0.001 in 10,000 time steps. The tensile stress is computed as the averaged stress along $x_1 = +W$. The expected yield stress due to slip on the pyramidal planes is τ_P/S, where S is Schmid's factor=0.433 for the two active pyramidal slip systems. Source strengths τ_{nuc} are chosen from a Gaussian distribution with standard deviation of $0.2\bar{\tau}_{nuc}$ with a time period of nucleation t_{nuc} = 25 ns for all slip systems. Material properties are chosen to mimic HCP zinc, with Young's modulus E=108 GPa, Poisson's ratio ν = 0.25, and with anisotropic slip properties listed in Table 4.1 as measured in 99.99% zinc single crystals by Stofel (1962), Pope (1967) and Blish (1967). We also consider isotropic materials for comparison, as indicated in 4.1. In Table 4.1, basal and pyramidal values are denoted by superscripts "B" and "P", respectively.

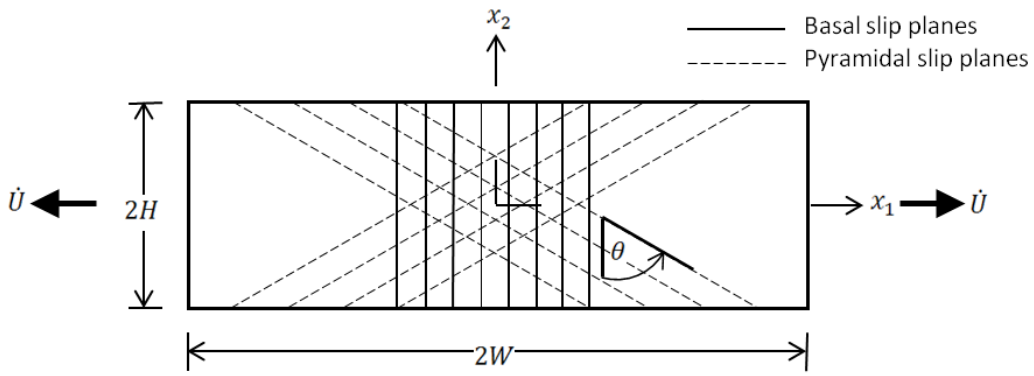

Figure 4.1: Geometry and boundary of tension problems with $\theta^{(1)}$=120° and $\theta^{(2)}$=60° for pyramidal planes and $\theta^{(3)}$=0° for basal planes.

In the absence of explicit work-hardening mechanisms, the stress-strain behavior in these materials is expected to be elastic/perfectly-plastic. The tensile flow stress should be controlled by the Peierls stress on the active slip systems, i.e. the pyramidal

Table 4.1: Isotropic and anisotropic properties of materials studied here; $\bar{\tau}_{nuc}$=50 MPa for all cases

<table>
<tr><th></th><th>τ_P^B (MPa)</th><th>τ_P^P (MPa)</th><th>b^B (nm)</th><th>b^P (nm)</th><th>B^B $\times 10^{-4}$(Pa.sec)</th><th>B^P $\times 10^{-4}$(Pa.sec)</th></tr>
<tr><td rowspan="7">Anisotropic</td><td rowspan="3">30</td><td>30</td><td rowspan="7">0.266</td><td rowspan="7">0.561</td><td rowspan="7">0.78235</td><td rowspan="7">2.10375</td></tr>
<tr><td>60</td></tr>
<tr><td>90</td></tr>
<tr><td rowspan="3">60</td><td>60</td></tr>
<tr><td>120</td></tr>
<tr><td>180</td></tr>
<tr><td>90</td><td>90</td></tr>
<tr><td rowspan="3">Isotropic</td><td colspan="2">30</td><td colspan="2" rowspan="3">0.266</td><td colspan="2" rowspan="3">0.78235</td></tr>
<tr><td colspan="2">60</td></tr>
<tr><td colspan="2">90</td></tr>
</table>

planes. Therefore, we perform tension simulations mainly for a fixed basal strength τ_P^B=30 MPa but also show that the flow stress is largely independent of the basal Peierls stress. The tensile response is linear until dislocations are nucleated and, once a sufficient stress is attained, dislocations can move against the Peierls barrier and cumulatively generate macroscopic plastic flow. However, the nominal flow stress is influenced by dislocation interaction effects, which are magnified in the anisotropic material due to the larger Burgers vector for pyramidal slip. These effects then also depend on some of the microscopic material or simulation parameters. We thus start by demonstrating and minimizing some of these interaction effects.

Fig. 4.2 shows the stress-strain behavior for several values of the minimum interaction distance r_c. For $r_c = 2b^B$, there is a marked stress drop below the nominal Peierls-controlled flow stress, as compared to $r_c = 6b^B, 10b^B$. This is accompanied by an increase in the number of dislocations on non-active the basal planes (see Fig. 4.2(b)) and a decreased number of pyramidal dislocations (see Fig. 4.2(c)) remaining in the sample as interaction forces drive them out of the sample surfaces. In this section, we use $r_c = 6b^B$, which is also consistent with the critical in-plane annihilation distance L_e.

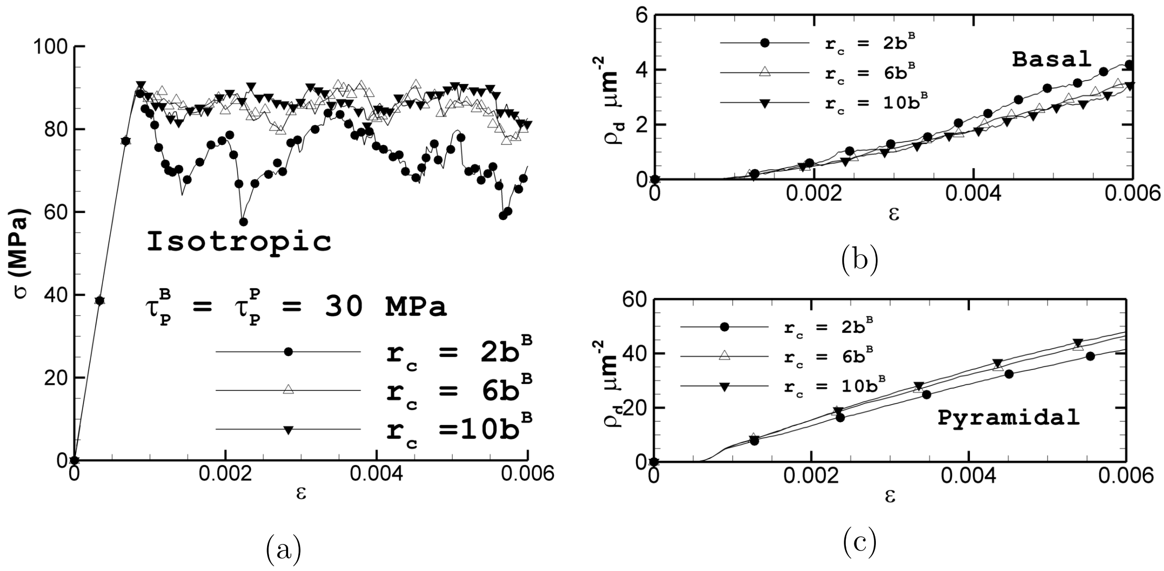

Figure 4.2: Tensile responses for isotropic materials with τ_P=30MPa for several minimum interaction distances, showing anomalous softening for the smallest value:(a) stress-strain curves (b) the dislocation densities on basal slips (c) the dislocation densities on pyramidal slips.

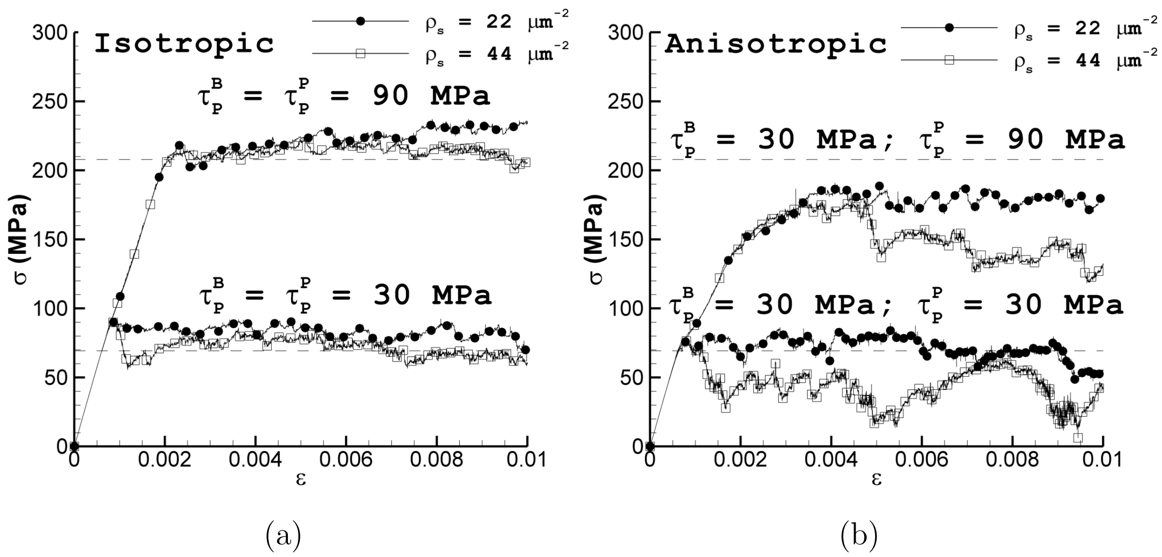

Figure 4.3: Effect of source density (ρ_s) on stress-strain curves for the cases of τ_P^P= 30 and 90 MPa (a) with isotropic properties (b) with anisotropic properties, and $\bar{\tau}_{nuc}$= 50MPa, $100b^B$slip spacing and strain rate($\dot{\epsilon}$)=2,000 s^{-1}.

Interaction effects are also related to the source density ρ_s. The initiation of plastic deformation is largely independent of the source density, since dislocation interactions are limited when the dislocation remain in dipoles near the sources. But, as shown in

Figs. 4.3a, 4.3b, a higher source density leads to a notable softening for the anisotropic materials while little change is observed for isotropic materials. The relatively large fields created by the pyramidal dislocations, due to their larger Burgers vectors, drive more sources to operate, leading to softening. For all further simulations, we use ρ_s=22 μm^{-2} to avoid this softening in the anisotropic materials.

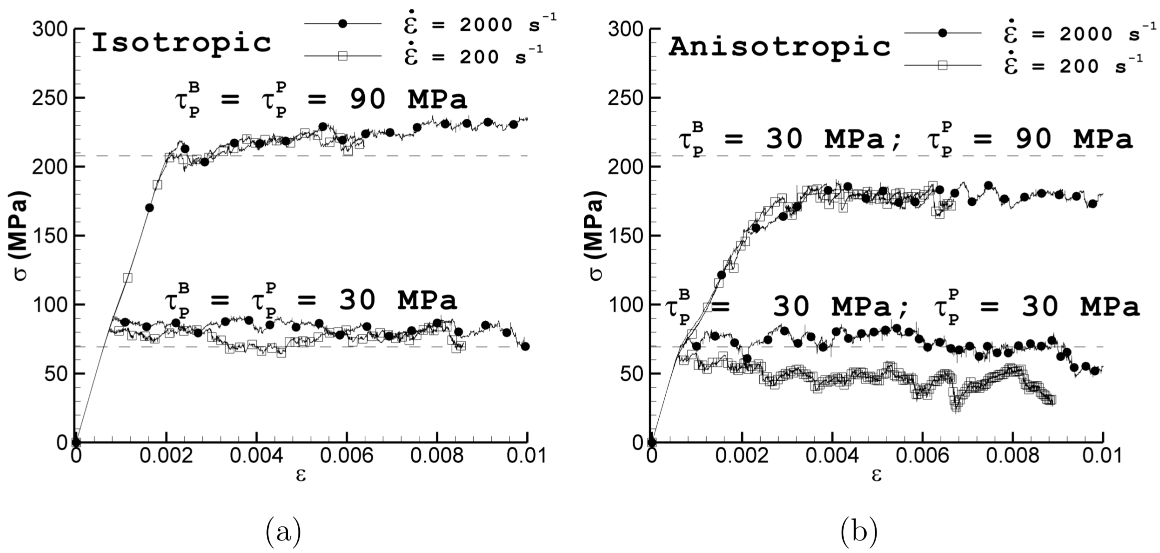

Figure 4.4: Effect of strain rates ($\dot{\epsilon}$) on the stress-strain responses for the cases of τ_P^P= 30 and 90 MPa (a) with isotropic properties (b) with anisotropic properties, and $\bar{\tau}_{nuc}$= 50MPa, 100b^Bslip spacing and source density (ρ_s)=22 μm^{-2}.

Since the dislocation mobility itself is also anisotropic, we have investigated the influence of loading rate on the tensile response. Stress-strain curves for isotropic and anisotropic specimens with strain rates ($\dot{\epsilon}$) of 2000s^{-1} and 200s^{-1} are shown in Fig. 4.4 for several different values of τ_P^P. Only the anisotropic material with a low Peierls stress shows a strain rate sensitivity, with a lower flow stress at the lower strain rate. In this case, there is more time available for dislocation activity to effectively trigger the nucleation and motion of dislocations by the high stress field caused by passing dislocations. This leads to a high density of dislocations, especially in non-active slip systems. Hence, for the remainder of our study we use a strain rate of 2000 s^{-1} to ensure that the plastic flow stress can be estimated for all cases of τ_P^P.

4.2.2 Tensile response

With parameters selected above to ensure that the flow stress is largely controlled by the Peierls barrier and, as importantly, that the materials exhibit no anomalous softening behavior, we now investigate the response of a wider spectrum of materials having an anisotropic Peierls-controlled plasticity, corresponding to the material parameters shown in Table 4.1.

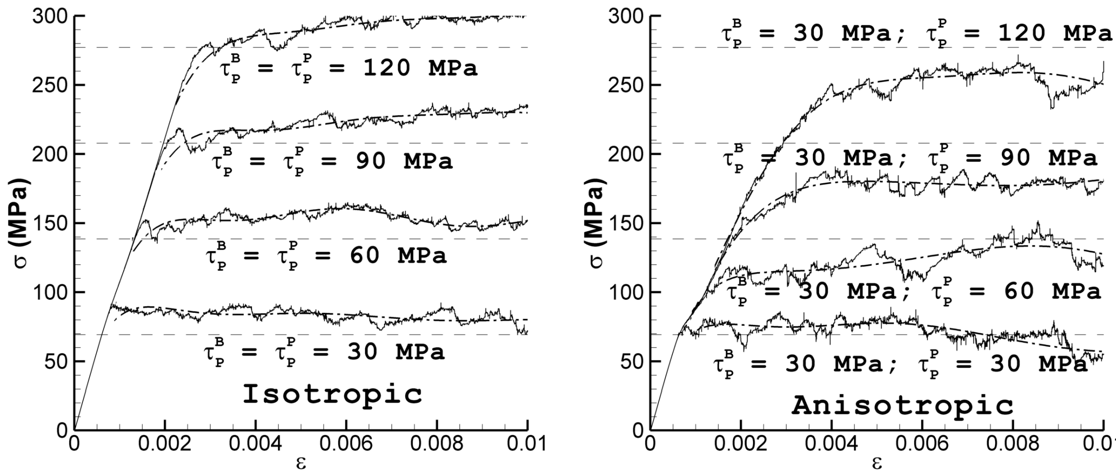

(a) (b)

Figure 4.5: Stress-strain curves for materials with τ_P^B= 30 MPa and various of τ_P^P= 30, 60, 90 and 120 MPa: (a) for isotropic materials (b) for anisotropic materials. Dash lines indicate expected flow stresses associated with τ_P^P; Dash-dotted lines are guides to the eye.

Fig. 4.5 shows the stress-strain tensile response for a range of materials. The dashed lines indicate the expected tensile flow stress for the specified τ_P^P for each case. For the isotropic cases, Fig. 4.5(a), the initial plasticity occurs a bit below the expected value but the flow stress increases with further straining until it slightly exceeds the expected flow stress. For the anisotropic cases, Fig. 4.5(b), there is a wider region of microplasticity prior to steady flow and then a roughly-constant flow stress that is slightly lower than the expected stress. This decrease is attributed to the remaining dislocation interaction effects caused by the larger pyramidal Burgers vectors in the anisotropic case. The emergence of a steady flow stress below that determined by the τ_P^P suggests the creation of a steady-state dislocation density and associated steady dislocation interaction stress. This effect may be manifested in the interpretation of real experiments if the flow stress under multiple-slip conditions does not correspond to the values derived from single-slip tests, in materials where the Burgers vectors are large enough to induce significant interaction effects inside the deforming material. Tests using basal Peierls stresses of $\tau_P^B = 60, 90$ MPa were performed for several values of the pyramidal Peierls stress. The results shown in Fig. 4.6 indicate that the basal Peierls stress does not significantly change the overall tensile response, and the dislocation densities in the two slip systems are also not affected. Since the applied resolved shear stress on the basal planes is zero in this orientation, the basal slip is generated only by interactions with the pyramidal dislocations. Basal slip does not contribute to the elongation of the sample, but could influence the stresses on the pyramidal dislocations and modify the flow stress. The absence of any significant dependence on the basal strength indicates that such interaction effects are negligible.

In the isotropic materials, the flow stress slightly exceeds the estimate based on the Peierls stress alone. This is attributed to a contribution to the flow stress from the source strength. Since the source strength is stochastically distributed, there is no obvious operative value. We thus use the simulation results on the isotropic materials to derive a value for the effective or operative source strengths, as follows. For a nucleated dipole, the total shear stress on each of the two dislocations in the dipole is comprised of the applied shear stress and the attractive shear stress due to the other dislocation as $\tau_{tot} = \tau_{app} - \dfrac{A}{2L_{nuc}}$ where $A = \dfrac{\mu b}{2\pi(1-\nu)}$. Dislocation glide begins when $\tau_{app} - \dfrac{A}{2L_{nuc}} = \tau_P^P$ and so the yield condition for the first glide of the dislocation dipole is

$$\tau_y = \tau_P^P + \frac{A}{2L_{nuc}} \; or \; \tau_y = \tau_P^P + \frac{\tau_{nuc}}{2} \tag{4.1}$$

This flow stress is always higher than the flow stress predicted from the pyramidal

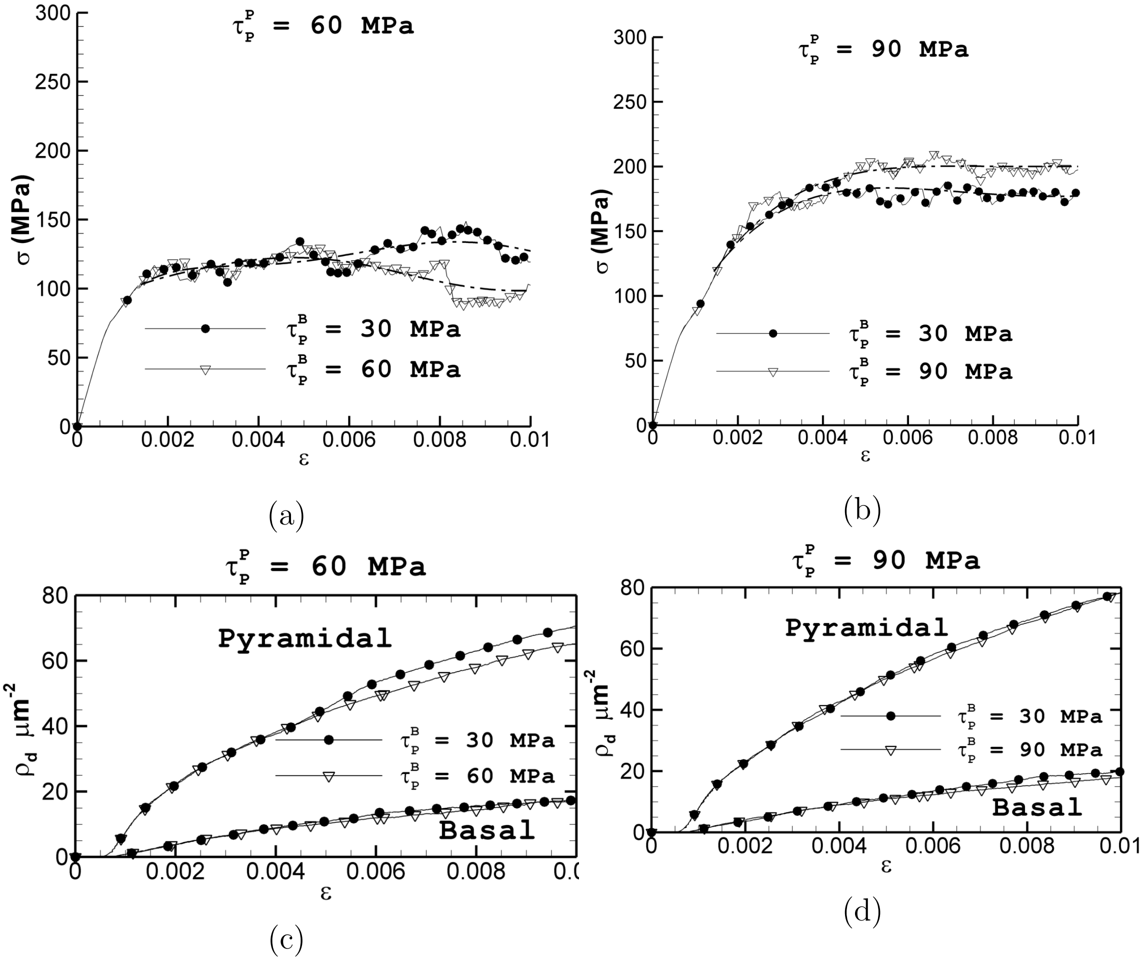

Figure 4.6: A comparison of stress-strain curves for anisotropic materials with different basal Peierls stress; (a) $\tau_P^P = 60$MPa with $\tau_P^B = 30$ and 60 MPa; (b) $\tau_P^P = 90$ MPa with $\tau_P^B = 30$ and 90 MPa (c) dislocation densities for $\tau_P^P = 60$ MPa with different $\tau_P^B = 30$ and 60 MPa (d) dislocation densities for $\tau_P^P = 90$ MPa with $\tau_P^B = 30$ and 90 MPa. Dash-dotted lines in (a) and (b) are guides to the eye.

Peierls stress alone as a result of the self-interaction of the dipole, $\tau_{nuc}/2$. Using the measured flow stresses in the isotropic materials, where dislocation interactions are negligible, the tensile flow stress generally exceeds the Peierls value by ≈20 MPa, which should equal $\tau_{nuc}^{eff}/\,(2 \cdot 0.433)$ where τ_{nuc}^{eff} is the shear strength of the effective, or actually operating, sources. We thus deduce τ_{nuc}^{eff} =17 MPa, indicating that the weakest operating sources have strengths 3 standard deviations below the mean value $\bar{\tau}_{nuc}$ =50 MPa, roughly comparable to previous estimates (Chakravarthy and Curtin

(2010a)). A corresponding value for the effective, or actually operating, source nucleation length is then $L_{nuc}^{eff} = A/\tau_{nuc}^{eff} = 0.297\mu m$. This length scale will be useful in interpreting the results of our fracture tests, to which we now turn our attention.

4.3 Mode-I crack growth

We now examine the effects of plastic anisotropy on the Mode-I crack growth in materials where the flow stress is controlled by a Peierls stress. An infinitely long crack in a two-dimensional single crystal is subjected to a far-field Mode-I stress-intensity loading, as shown in Fig. 4.7, by applying prescribed displacements corresponding to the isotropic, linear elastic mode I stress-intensity field (Deshpande et al. (2003a) and Cleveringa et al. (2000)). Symmetry about the crack plane is used so that only the

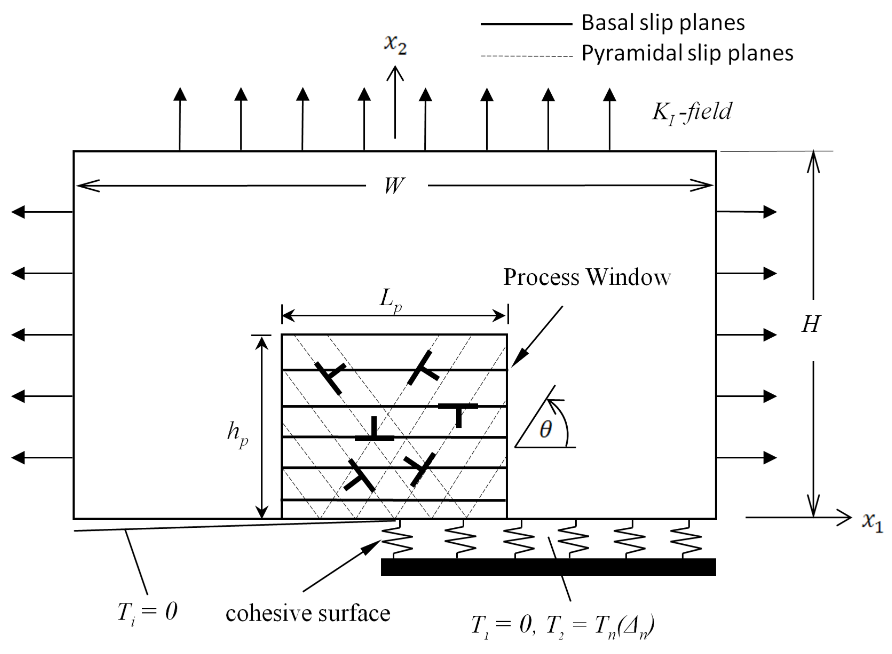

Figure 4.7: Schematic of the Mode-I crack problem with the imposed boundary conditions.

upper half of the crystal is directly simulated. The initial crack tip is located at the origin x=y=0 and the surface x<0, y=0 is traction-free. Crack growth is modeled using a cohesive zone model that extends along the crack plane x>0, y=0. We use values for the cohesive properties of σ_{coh}=2 GPa and δ_n=0.18394 nm, giving a work of fracture ϕ_n=1 J/m^2 and $K_0 = 0.335$ MPa$\sqrt{\text{m}}$. A new superposition technique of O'Day and Curtin (2005) is used, as described in Chapter 2 (Chakravarthy and Curtin (2011a)). In addition, the singular stress fields and displacement fields for each dislocation are computed using the half-space solution for $x_2 > 0$ (Freund (1993)). During crack growth, a mesh adaption scheme is employed that maintains full resolution at the tip of the current crack Chakravarthy and Curtin (2011a). While a dislocation is free to glide anywhere in the sample domain of $W \times H = 1000 \times 500\mu\text{m}^2$, all dislocation sources are contained within a process window of size $L_p \times h_p = 30 \times 30\mu\text{m}^2$ centered on the original crack tip position. The material properties are exactly those considered in the tension tests of section 4.3, and summarized in Table 4.1; the tensile flow stress along the 0° line for each material is thus known and obtained from the data in Fig. 4.5 and Fig. 4.6 using the 0.2% offset yield stress construction.

With increasing applied Mode-I loading, dislocation plasticity is initiated around the crack tip and, at some point, the crack begins to move forward with increasing applied load. The applied Mode-I loading versus the amount of crack growth is the "crack resistance" or "R-curve" that characterizes the toughening. At a sufficiently high load, the crack will grow with no further applied load, and this load level represents the fracture toughness K_{IC} of the material. The R-curves for various materials having different yield stresses and plastic anisotropy are shown in Fig. 4.8, with each sub-figure showing results for four different random distributions of the dislocation sources to demonstrate the purely stochastic variations in the fracture behavior; some cases of high toughness do not show the final fracture stage for brevity. The fracture toughnesses in Fig. 4.8 are characterized by the value of the pyramidal Peierls stress, from which the tensile yield stress can be approximated. Fig. 4.8(a-e) and 4.8(f-h) are carried out using anisotropic properties and isotropic properties, respectively, as given in Table 4.1. Overall the toughness tends to decrease with increasing the yield stress, with lower yield stresses showing a large variation of crack initiation and tough-

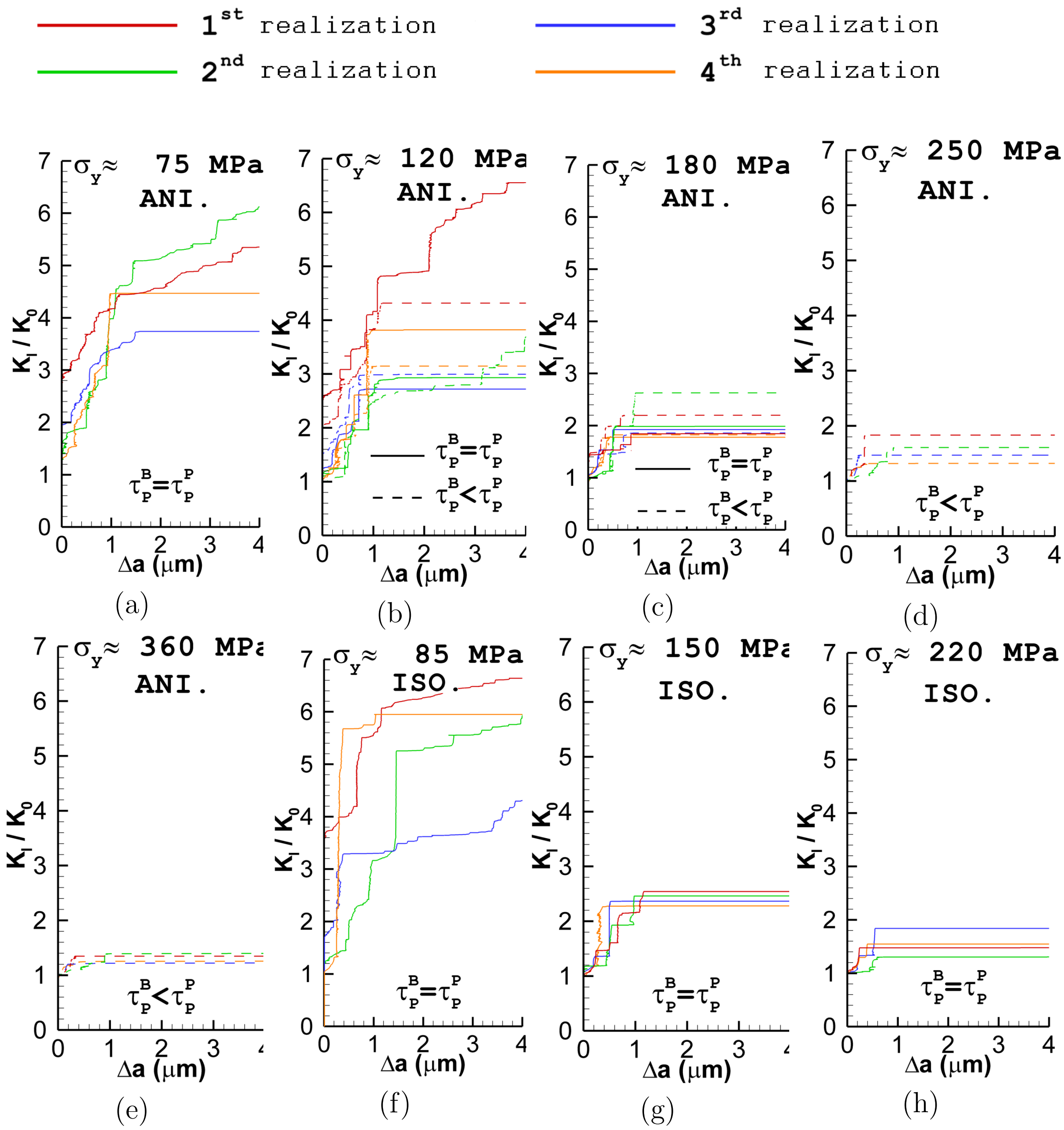

Figure 4.8: Mode-I crack growth resistance curves for four realizations of source/obtacle randomness in various cases of yield stresses denoted by (σ_y: τ_P^B, τ_P^P) in MPa with anisotropic slip properties (ANI.); (a) 75: 30, 30 (b) 120: 60, 60 (solid lines) and 120: 30, 60 (dashed lines) (c) 180: 90, 90 (solid lines) and 170: 30, 90 (dashed lines) (d) 250: 60, 120 (e) 360: 60, 180 and with isotropic slip properties (ISO.); (f) 85: 30, 30 (g) 150: 60, 60 (h) 220: 90, 90.

ness, since they are closer to purely brittle behavior. The dashed lines in Fig. 4.8(b,c) denote materials with a lower basal Peierls stress, which according to Fig. 4.6 have the nearly the same tensile yeild stress in the direction normal to the crack plane as the corresponding materials with the higher basal Peierls stress. The R-curves and toughnesses are similar in cases of τ_P^P=60 MPa and only slightly tougher for cases of τ_P^P=90 MPa, as illustrated in Fig. 4.8(b,c), so that the toughness is primarily controlled by the yield stress with minimal anisotropy effects. We further examine the

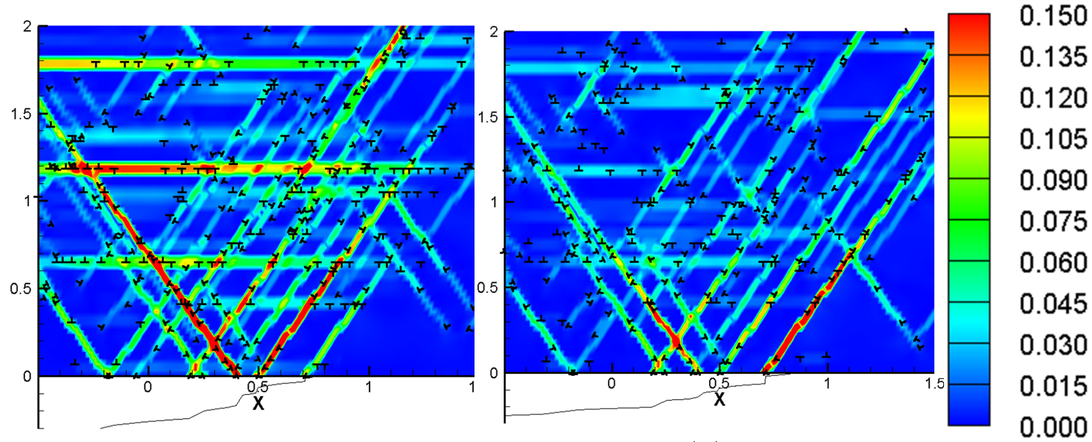

(a) (b)

Figure 4.9: Contours of the total plastic slip, $\sum_{i=1}^{3}|\gamma_i|$, from DD simulation and crack opening profiles (magnified 10 times) close to the critical fracture toughness for anisotropic materials with τ_P^P=60MPa and two different basal Peierls stresses: (a) τ_P^B= 30MPa and (b) τ_P^B= 60MPa. (All distance are in microns)

influence of anisotropy on the slip by analyzing contours of total plastic slip, defined as $\sum_{i=1}^{3}|\gamma_i|$ where γ_i is the resolved shear strain from the dislocations on slip planes with angle $\theta_{(i)}$. Total plastic slip is shown Fig. 4.9(a) and 4.9(b) for two cases with the same pyramidal properties but differing basal strength τ_P^B. There is more basal slip for a lower basal Peierls stress, but this does not influence the crack growth. The insensitivity of the toughening to the basal slip can be understood by examining dislocation shielding/anti-shielding. Basal dislocations are predominantly nucleated in a wedge region above the crack between the lines at 60° and 120° emanating from the initial crack front, where the crack stress field generates a sufficient resolved shear stress. However, Fig. 4.10 shows contour plots of the shielding/anti-shielding due to an individual dislocation as a function of position and Burgers vector Lin and Thomson (1986) which indicate that such basal dislocations have a very small effect on the crack tip stress intensity compared to dislocations on the pyramidal slip planes at $\theta^{(1)} = 120°$ and $\theta^{(2)} = 60°$. Thus, basal slip has little effect on the crack behavior. Once the crack starts growing (to the right) the basal dislocations are left behind in a plastic wake but with decreasing shielding ability. Thus, any effect of basal slip on crack growth is indirect through its influence on the pyramidal slip.

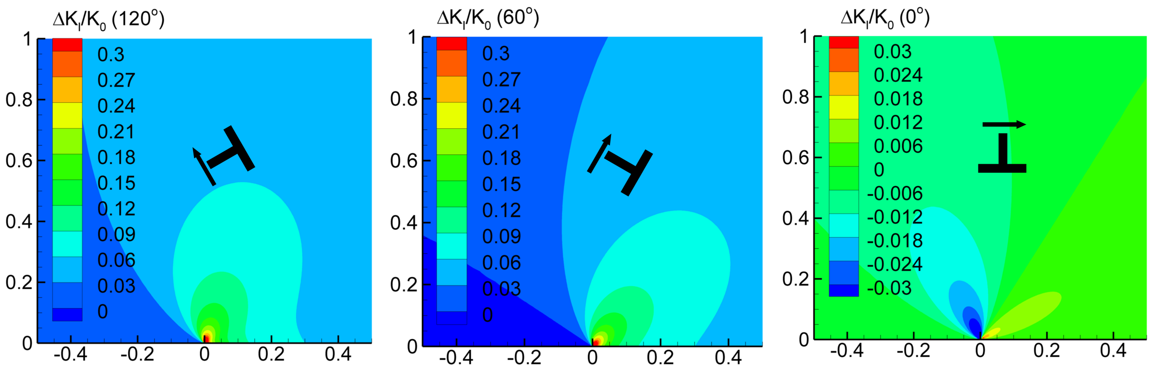

(a) (b) (c)

Figure 4.10: Normalized Mode-I crack shielding contribution as a function of position for: (a) $\theta^{(1)}$=120° (b) $\theta^{(2)}$=60° (c) $\theta^{(3)}$=0° where the *anisotropic* material properties ($|b^B| < |b^P|$) are used as in Table 4.1

The normalized fracture toughness versus normalized yield stress σ_y/σ_{coh} for all cases in Table 4.1, with four statistical realizations for each material type, is shown in Fig. 4.11. In general, the fracture toughness increases as the yield stress decreases, with both isotropic and anisotropic cases following the same trend qualitatively and quantitatively. The general trend is not surprising because the plastic zone size, and hence plastic dissipation, are increased with decreasing yield stress. The statistical variations in fracture toughness among the four realizations exhibit more variation at lower yield stresses, in part because of the much larger number of dislocations and possibility of wider variations in local crack-tip conditions driving the onset of rapid crack growth. Compared to the statistical variations, any systematic trends in fracture toughness due to anisotropy (i.e. τ_P^P/τ_P^B) are negligible.

Also shown in Fig. 4.11 are the fracture toughnesses computed using the same numerical 2d-DD methods but for materials where the yield stress is controlled by ob-

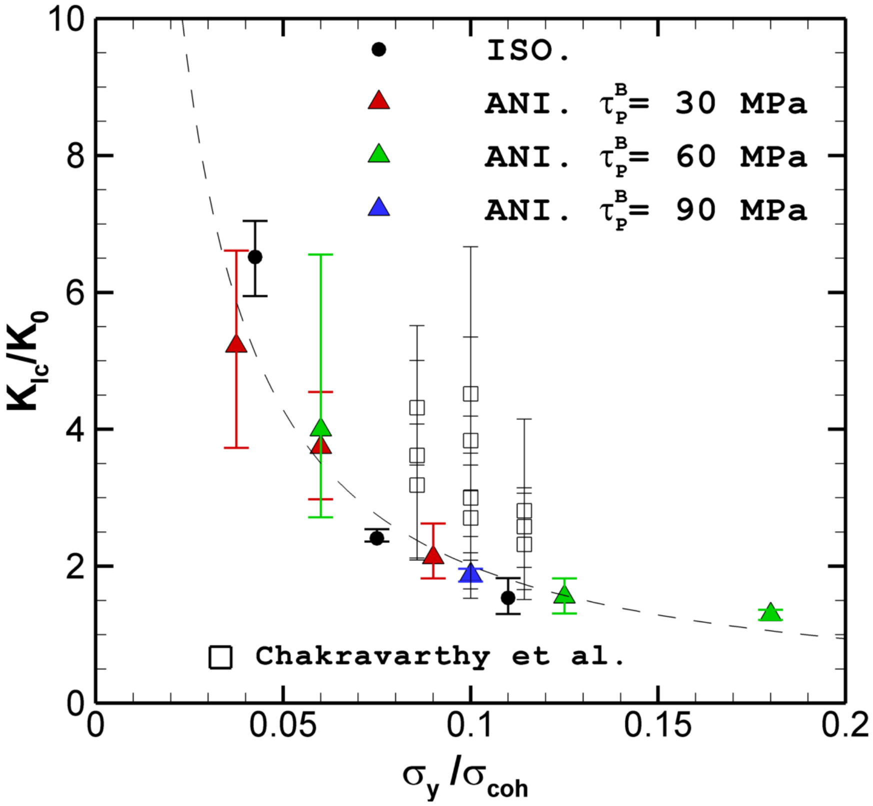

Figure 4.11: Normalized fracture toughness K_{Ic}/K_0 versus yields stress σ_y for all cases in Table 4.1 (filled symbols) and for the obstacle controlled yield (non-filled symbols) from Chakravarthy and Curtin (2010b). Error bars show the variation of 4 statistical random realizations of source points. The dash line is the guide line for all data.

stacles to dislocation motion. These materials have both high strength (σ_y=600MPa-800MPa) and higher cohesive strength (σ_{coh}=7 GPa Chakravarthy and Curtin (2010b), and show much higher toughness than the present materials where the yield stress is controlled by a Peierls stress. In the obstacle-controlled-strength cases, materials with the same yield strength but different internal average obstacle spacing have different toughnesses. These comparison show that the internal mechanisms of strengthening are crucial in determining the macroscopic material toughness, i.e. toughness is not determined by yield strength alone.

Chakravarthy and Curtin (2010b) showed that the toughness in the obstacle-controlled materials could be understood by considering the operation of the source-obstacle dislocation pile-up configurations in the presence of a stress gradient. The effective yield stress σ'_y due to the crack-tip stress field could be related to the tensile yield stress as

$$\sigma'_y = \frac{\sigma_y}{(1 - \chi L_{obs}/4)} \tag{4.2}$$

where L_{obs} is the average spacing between dislocation obstacles and χ is the normalized magnitude of the stress gradient at the dislocation sources closest to the crack tip. They further explored and validated this "Stress Gradient Plasticity" concept in a recent publication Chakravarthy and Curtin (2011b). Here, the yield stress is controlled by the Peierls stress and there are no dislocation pile-ups. There thus seems to be no analog to the obstacle spacing L_{obs}. However, we show below that there is a stress-gradient effect with the material length scale L_{nuc} and that the toughness data of Chakravarthy et al. and of the present study can be unified through the "Stress Gradient Plasticity" concept.

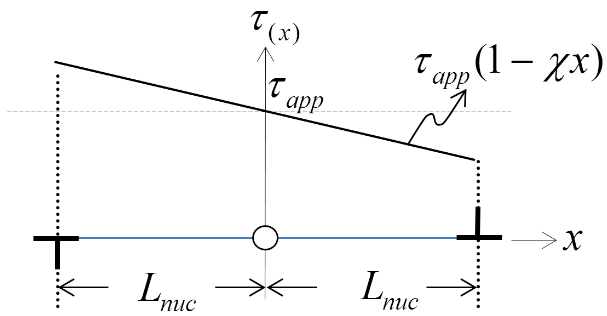

Figure 4.12: A simple model for the yield stress controlled by Peierls stress with applied shear stress on a dislocation dipole with gradient χ(always positive) as a function of x and resolved shear stress at source point (x=0),τ_{app}.

We consider a dislocation source in the presence of an applied linear stress gradient given by $\tau(x) = \tau_{app}(1 - \chi x)$, where $\chi > 0$ and τ_{app} is the stress at the position $x = 0$ of the source (Fig. 4.12). Once a dipole is nucleated at $\tau_{app} = \tau_{nuc}$, the dislocations on the left and right of the source at $x = \pm L_{nuc}$ are subjected to higher and lower stresses, respectively. With increasing applied stress, each dislocation will glide when

$$\tau_{app}\left(1-\chi x\right)-\frac{A}{2L_{nuc}}\geq\tau_P. \tag{4.3}$$

The dislocation on the left is subjected to a higher applied shear stress and so will glide first and move away from the source. However, the dislocation on the right side remains under a lower stress, and cannot move away nor can the source operate further. Thus, there is no significant plasticity. Plasticity can ensue only after the dislocation on the right side moves. The applied stress required to start glide of the dislocation on the right side therefore controls the apparent yield stress. If the gradient is large enough, then the dislocation on the left side moves far away and exerts no stress on the remaining dislocation. The apparent shear yield stress (for a sufficient gradient) is thus given simply by

$$\tau_y'=\frac{\tau_P}{(1-\chi L_{nuc})} \tag{4.4}$$

The tensile yield stress follows using the Schmid factor and, in the presence of the stress gradient, is always larger than the tensile yield stress. Eq. 4.4 differs from Eq. 4.2 by a factor of 4 due to the absence of a pile-up and due to definitions of L_{obs} and L_{nuc}. Whether Eq. 4.4 is a true "Stress Gradient" effect or simply reflects the fact that operation of the source is controlled by the stress at a distance L_{nuc} away may be a semantic issue, but the general fact that internal length scales and stress gradients influence the yield stress remains clear.

We apply the "Stress Gradient Plasticity" concept to interpret the fracture results as follows. Following Chakravarthy et al., the stress gradient χ at distance r from the tip of the mode-I crack is given by

$$\chi=abs\left[\frac{d}{dr}\tau_{r\theta}\right]\frac{1}{\tau_{r\theta}}=\frac{0.5}{r} \tag{4.5}$$

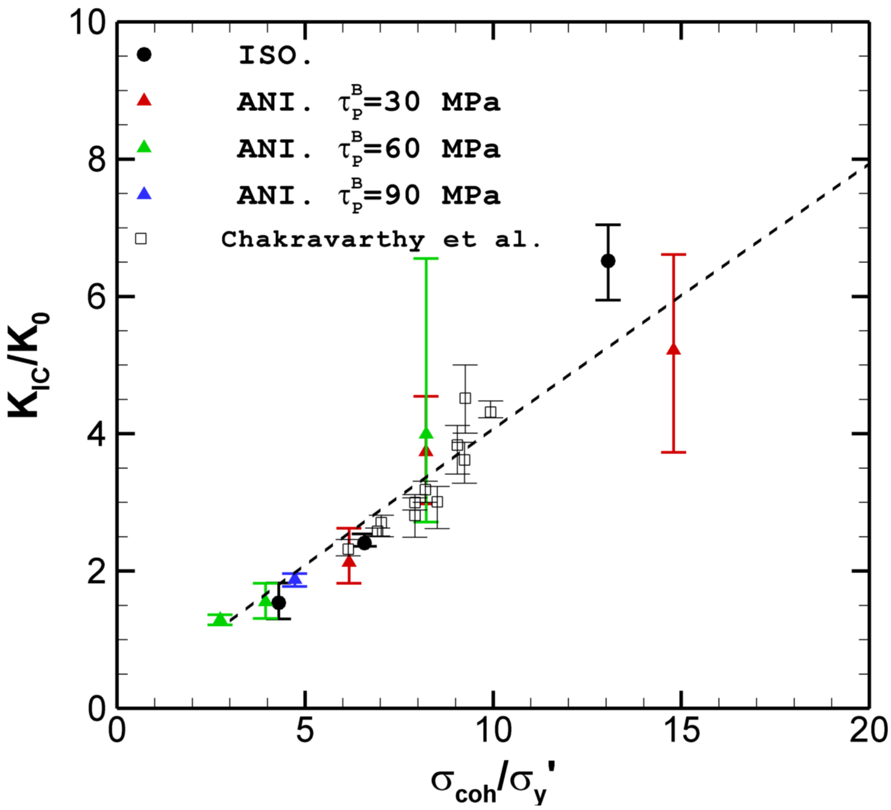

Figure 4.13: Fracture toughness K_{IC}/K_0 versus σ_{coh}/σ'_y for materials with yield controlled by the Peierls stress (solid circle and solid delta symbols from Fig. 4.11) and for materials with yield controlled by obstacle $\rho_s = 66\mu m^{-2}$(square symbols) in Chakravarthy and Curtin (2010b) where σ'_y is the appropriate "stress gradient" yield stress near the crack tip. Dash line is to guide the eye.

since $\tau_{r\theta} = \dfrac{K_I}{\sqrt{2\pi r}} f(\theta)$. The relevant distance r is then the typical distance of the sources nearest to the crack tip, $r = 1/\sqrt{\rho_s}$ where ρ_s is the source density. Since tensile flow and dislocation shielding are controlled by the pyramidal slip planes, r should actually only reflect these sources so that $r = (2\rho_s/3)^{-1/2}$. The relevant value of L_{nuc} is the effective value L_{nuc}^{eff} computed earlier in interpreting the data on isotropic tensile flow. Interaction effects that cause the yield stress in the anisotropic materials to be below those in the isotropic materials are attributed to interaction effects, which are assumed to only influence the local applied stress on the source so that L_{nuc}^{eff} applies to all isotropic and anisotropic systems. The relevant apparent yield stress under the action of the stress gradient created by the crack tip field is then

$$\frac{\tau_y'}{\tau_y} = \frac{\tau_P^P}{(1 - \sqrt{\frac{\rho_s}{6}} L_{nuc}^{eff})(\tau_P^P + \frac{\tau_{nuc}^{eff}}{2})} \tag{4.6}$$

where τ_y is the yield stress under a uniform stress field. All the quantities entering Eq. 4.6 above are material parameters fixed in our simulations and are not adjustable. Noting that $\tau_y'/\tau_y = \sigma_y'/\sigma_y$, the predicted fracture energy K_{IC}/K_0 versus the inverse normalized stress-gradient-modified yield stress $\sigma_{coh}/\sigma_{y'}$ is shown in Fig. 4.13 for both the present data, with Eq. 4.6 controlled by the Peierls stress, and the data of Chakravarthy, with Eq. 4.2 controlled by the obstacles. Both sets of data now collapse onto a single curve. The "Stress Gradient Plasticity" concept, suitably generalized, thus provides a unifying picture for the fracture of two very different types of materials. This result further strengthens the finding of Chakravarthy and Curtin (2010b, 2011b) that the internal material length scales determining the flow stress in a given material are also the physical length scales responsible for some "gradient" plasticity effects.

4.4 Microcrack formation

As noted in the introduction, microcrack initiation a few microns away from the existing crack tip on the parallel basal planes, leading to the ligament formation and additional toughening, is reported by Catoor and Kumar (2008). Microcrack nucleation has also been reported in other literature Deruyttere and Greenough (1956), Gilman (1958), Parisot et al. (2004), Stofel (1962), but its origins remain unclear. Here, we examine the normal stresses that are created on the basal planes within the DD simulations, and suggest an origin for the stress concentrations that are necessary to drive basal microcracking.

Fig. 4.14(a) shows one *typical* example of the distribution of tensile stress normal

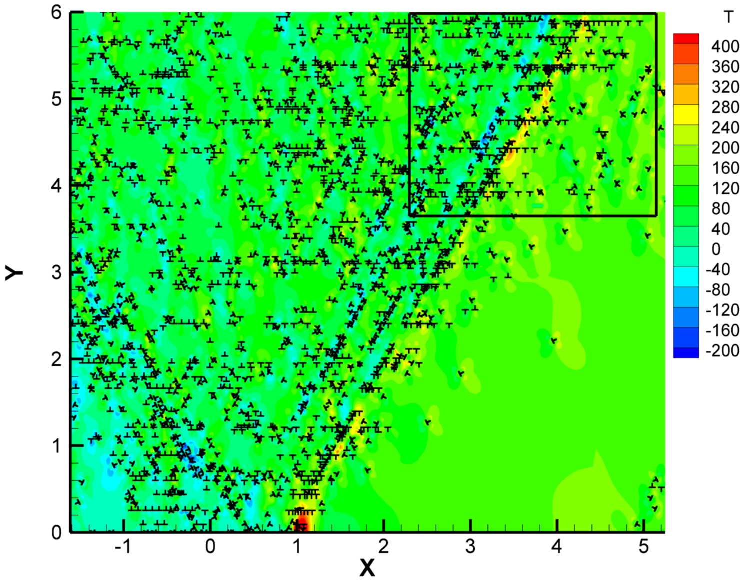

(a)

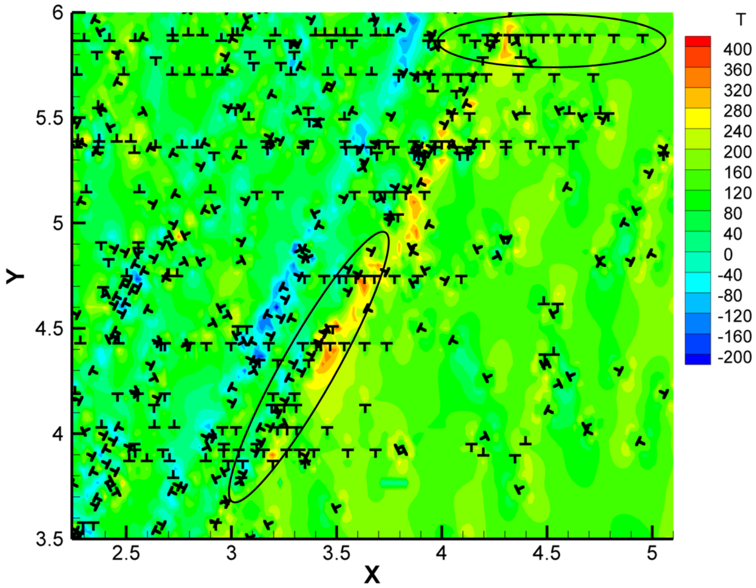

(b)

Figure 4.14: Normal stress contours, σ_{yy} (MPa) and dislocation distribution at K_I/K_0 = 4.4 with the crack tip x= 0.96 microns for an *anisotropic* material with τ_P^B = 30 MPa, τ_P^P = 30 MPa for the 4^{th} realization. (a) total normal stress field over a large scale, showing local stress concentrations microns from the crack tip along the 60° line; (b) total normal stress field in a region around a stress concentration, with the two circled regions indicating instances of long queues of positively-signed 60° dislocations and of negatively-signed 0° dislocation that aggregate around the 60° line.

to the basal planes as predicted from the simulations. Overall, on a large scale, the stress fields are replicating something similar to the constant-sector stress fields in the regions (0°-54.74°, 54.74°-90°, 90°-125.26°, 125.26°-180°) predicted by Rice (1987b) for a perfectly-plastic material. At the boundaries between the constant-stress sectors, some sort of structure must exist to effect the transition in stress. In the Rice model, this structure is a kink band, which can also be seen in DD predictions for a BCC-like geometry Van der Giessen et al. (2001). Drugan (2001) carried out an analysis similar to that of Rice but without requiring a kink band. DD predictions for an FCC-like geometry do not, however, agree with the Rice prediction of slip activity on 0° that concentrates in a kink band at 90°. Constant-stress sectors have been measured experimentally for single crystals by Crone and Shield (2001) for FCC and Shield and Kim (1994) for BCC, with some evidence of a kink band in the BCC case. In the DD simulations, we observe some intense dislocation structure along the 60 degree slip plane emanating from the local crack tip. Most importantly for microcracking, however, is that we also observe very local stress concentrations in various regions along/near this 60-degree line. These local stress concentrations are on the order of a few hundred MPa. When combined with the applied crack tip field also of a few hundred MPa, the local tensile stresses can reach 400 MPa at these locations. Such local stress concentrations occur in all of our simulations. This level of stress may still be insufficient to nucleate microcracks, which depends on the cohesive strength of the basal planes (likely on the order of a few GPa; we use 2 GPa here for our fracture simulations), but the fact that high stress concentrations exist suggests that they could be responsible for basal microcrack nucleation.

We now examine the origins of the observed local stress concentrations. Fig. 4.14(b) shows long lines of basal dislocations, but not densely packed, around the 60° line. These are formed due to the crack tip stress field, which drives negative-signed basal dislocations toward the 60° line from both sides of the line. Fig. 4.14(b) also shows a large number of positively-signed 60° pyramidal dislocations along the 60° line. These are presumably formed due to dislocations nucleated by sources near the crack tip, for which the oppositely-signed dislocations exit through the crack faces, and by oppositely-signed dislocations from further sources along the same slip plane(s) annihilating some of the positively-signed dislocations, leaving remaining positively-signed dislocations at further distances. At some locations, there are intersections of the accumulated basal and pyramidal dislocations, which is a geometry proposed by Stofel to generate prism dislocations and damage accumulation. We have calculated the interactions between basal and prism dislocations as they approach one another, and find that they are generally repulsive so that a high local dislocation density is not formed. Here, as seen in Fig. 4.14, the tensile stress concentration observed along the 60° line is not generated by such basal/pyramidal interactions. Therefore, the local stress concentrations are due to some other mechanism.

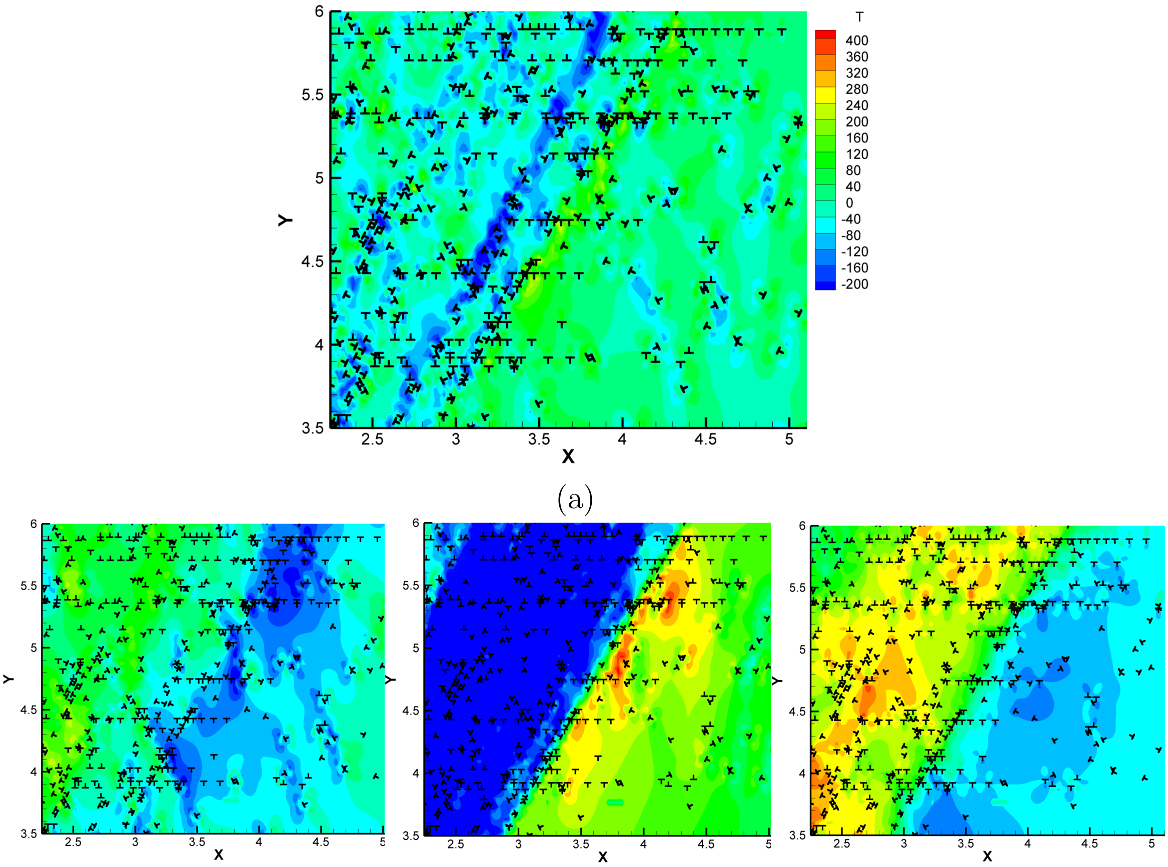

(a)

(b) (c) (d)

Figure 4.15: Contribution of dislocations on each individual slip system to the local σ_{yy} stress concentrations (MPa) shown in Fig. 4.14(b): (a) σ_{yy} due to all dislocations (120°+60°+0°); (b) σ_{yy} due to the 120° pyramidal slip system; (c) σ_{yy} due to the 60° pyramidal slip system; (d) σ_{yy} due to the basal slip system.

We therefore proceed by computing the stresses generated by each of the three separate types of dislocations, basal 0° 60° and 120°, as shown in Fig. 4.17. As seen clearly in Fig. 4.17, a high tensile stress field is generated along much of the 60° line by the queues of 60° dislocations while the basal dislocations contribute a small compressive stress in this region and the pyramidal dislocations on the 120° plane other slip contribute rather large compressive stresses along this line. The net magnitude of the dislocation field (0°+60°+120°) is typically compressive, as illustrated in Fig. 4.17(a). Hence the overall net tensile stress is generally lower, tending toward the values of the continuum sector solutions (Fig. 4.14). However, the cancellation of positive and negative stress concentrations is not complete, leading to residual local stress concentrations. In other words, the stress concentrations appear due to the stochastic and discrete nature of the discrete dislocation fields. On the whole, the dislocations collectively generate a large-scale response consistent with the expected continuum fields. But along the sector boundary, where significant cancellation would be required, there remain isolated locations where the tensile stresses are much larger than the continuum values. The DD simulations therefore suggest that microcrack nucleation occurs preferentially along the pyramidal direction emanating from the current crack tip, and at locations that are random and can be found several microns away from the crack tip. We have arrived at these conclusions through analysis of many of our simulations, see Fig. 4.16-Fig. 4.25.

The magnitude of the stress concentrations is expected to depend on the accumulation of pyramidal slip along the 60° lines. Such pyramidal slip is controlled by the source strengths and the Peierls barrier, with lower values encouraging more slip. The values used here are relatively high compared to real Zn, suggesting that larger stress concentrations could be generated in real Zn. Our simulations also neglected explicit crack-tip dislocation emission along the pyramidal planes, which would further enhance pyramidal slip and also blunt the crack, leading to higher loading and more plasticity. This factor would thus also drive toward higher local stress concentrations. Thus, while we do not have sufficiently high, or quantitatively accurate, levels of stress, the general mechanism of formation of local stress concentrations is identified and we have some rational for possible higher local stress concentrations in real Zn.

4.5 Summary

We have explored fracture in HCP-like single crystals, such as Zinc, using a 2d-DD model with a Peierls stress approach to control the plastic anisotropy associated with basal and pyramidal slip. Our results lead to the following conclusions:

- The fracture toughness scales inversely with the tensile yield stress, largely independent of the plastic anisotropy, so that increasing Peierls stress on the pyramidal planes gives decreasing resistance to crack growth;

- The observations of Catoor and Kumar (2008) of lower crack tip plastic strains, higher stresses, and lower toughening for their "orientation 2" in Zn is due to the higher in-plane yield stress in this orientation, probed here by varying the in-plane pyramidal Peierls stress. This is consistent with continuum FEM-level analyses in Catoor and Kumar (2008);

- Basal slip occurs extensively around the crack tip but it does not significantly influence crack growth along the basal planes, consistent with results of Catoor and Kumar (2008). The basal slip is driven by the applied crack tip field, and is necessary in certain regions to help generate the necessary sector-like solutions, but the basal dislocations in these regions do not provide significant crack shielding;

- Analyzing the fracture results within the framework of Stress Gradient Plasticity concepts shows that the equilibrium dislocation dipole spacing serves as an internal material length scale for controlling fracture toughness. Furthermore, the fracture toughness of materials with a Peierls stress and no obstacles and of materials with obstacles and zero Peierls stress can be unified through the Stress Gradient Plasticity concept, demonstrating the general feature that internal material length scales can control fracture;

- Microcrack nucleation along basal planes parallel to the main crack may be a consequence of tensile stress concentration that exist along the 60° line emanating from the crack tip, due to incomplete cancellation of dislocation stress fields in structures that are attempting to generate the constant stress sectors expected from continuum-level analysis. The stress concentrations are thus a direct consequence of the discreteness of the dislocation plasticity.

Our conclusions above serve to corroborate continuum analyses, to provide physical rationals for the role of basal slip and occurrence of basal microcracking, and to demonstrate that dislocation-level phenomena play a key role in determining macroscopic material fracture response, through both Stress-Gradient concepts and the discreteness of dislocation plasticity.

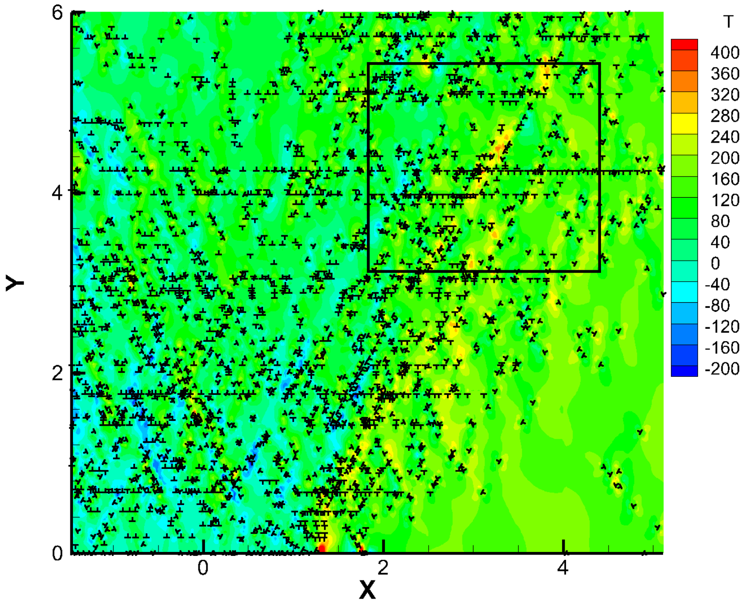

(a)

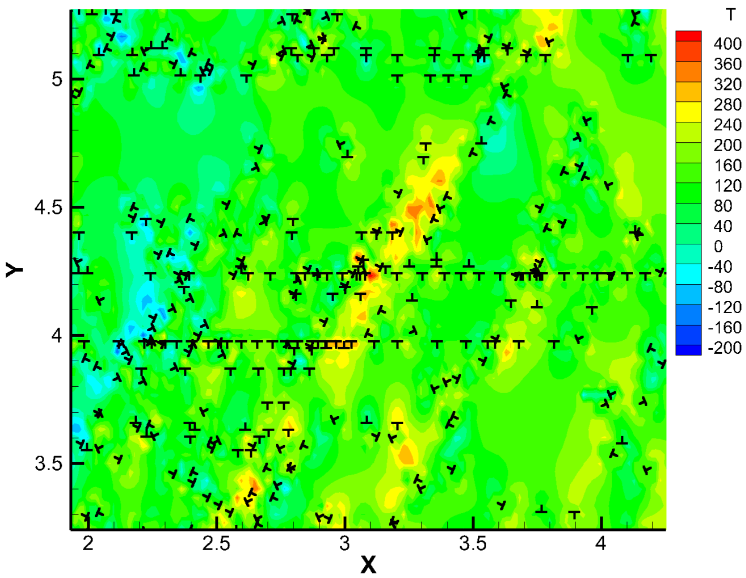

(b)

Figure 4.16: Normal stress contours, σ_{yy} (MPa) and dislocation distribution near toughness for an *anisotropic* material with $\tau_P^B = 30$ MPa, $\tau_P^P = 30$ MPa for the 1^{st} realization. (a) total normal stress field over a large scale, showing local stress concentrations microns from the crack tip along the 60° line; (b) total normal stress field in a region around a stress concentration.

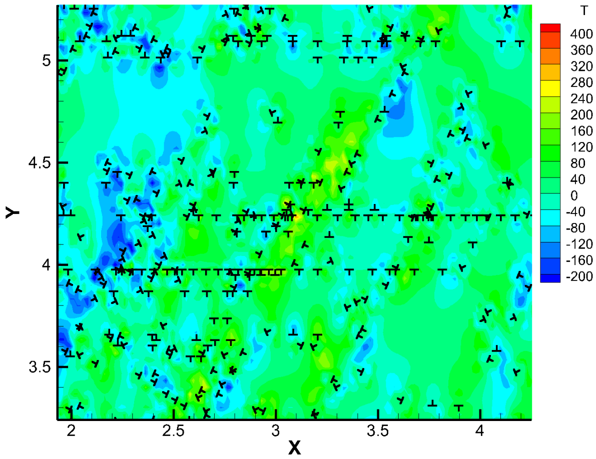

(a)

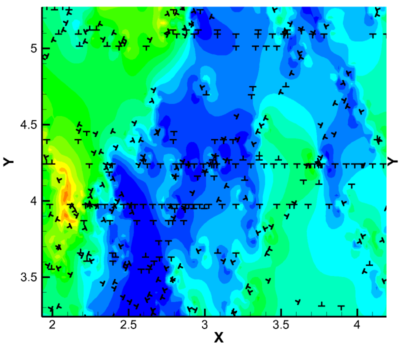

(b)

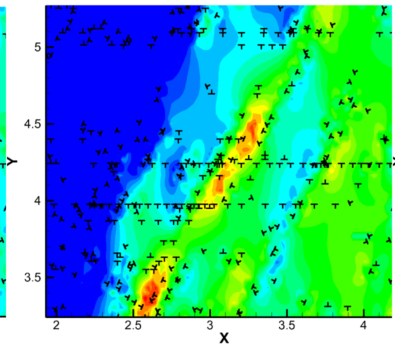

(c)

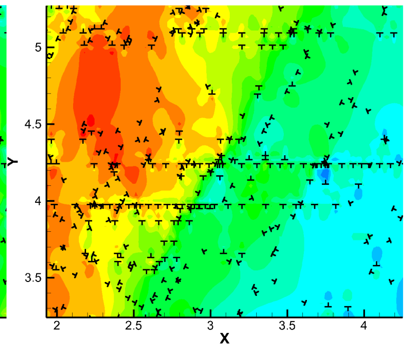

(d)

Figure 4.17: Contribution of dislocations on each individual slip system to the local σ_{yy} stress concentrations (MPa) shown in Fig. 4.16(b): (a) σ_{yy} due to all dislocations (120°+60°+0°); (b) σ_{yy} due to the 120° pyramidal slip system; (c) σ_{yy} due to the 60° pyramidal slip system; (d) σ_{yy} due to the basal slip system.

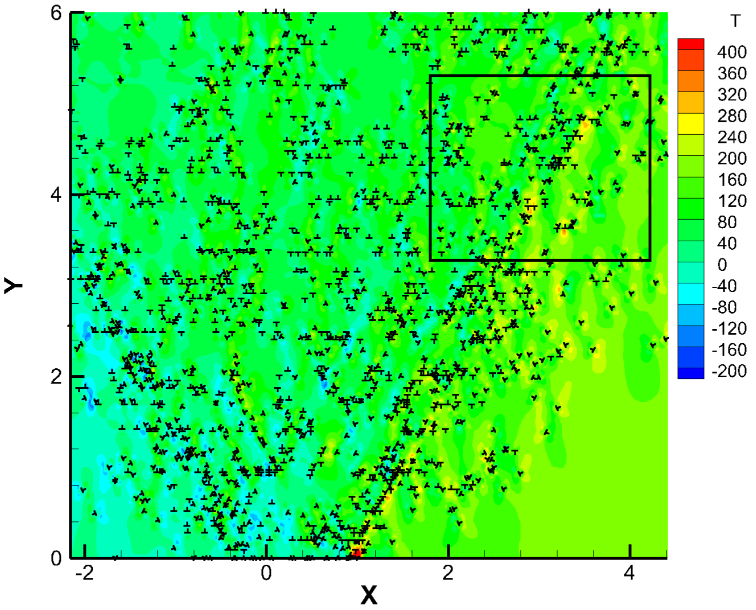

(a)

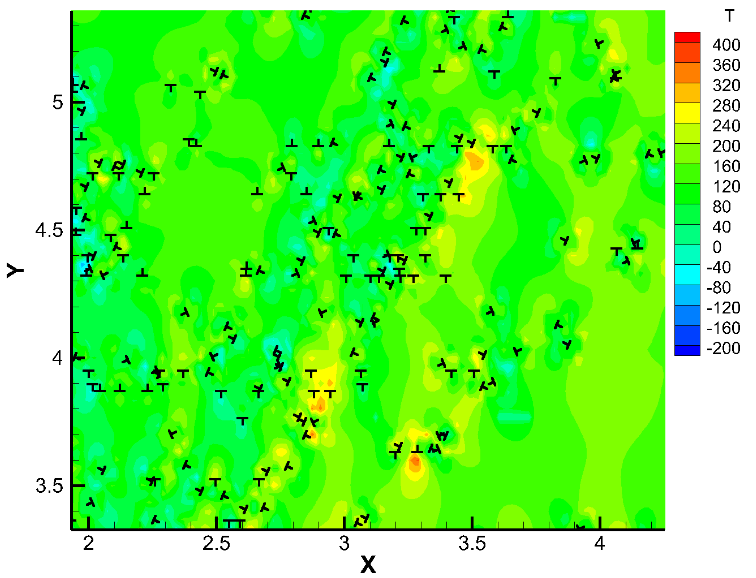

(b)

Figure 4.18: Normal stress contours, σ_{yy} (MPa) and dislocation distribution near toughness for an *anisotropic* material with $\tau_P^B = 30$ MPa, $\tau_P^P = 30$ MPa for the 2^{nd} realization. (a) total normal stress field over a large scale, showing local stress concentrations microns from the crack tip along the 60° line; (b) total normal stress field in a region around a stress concentration.

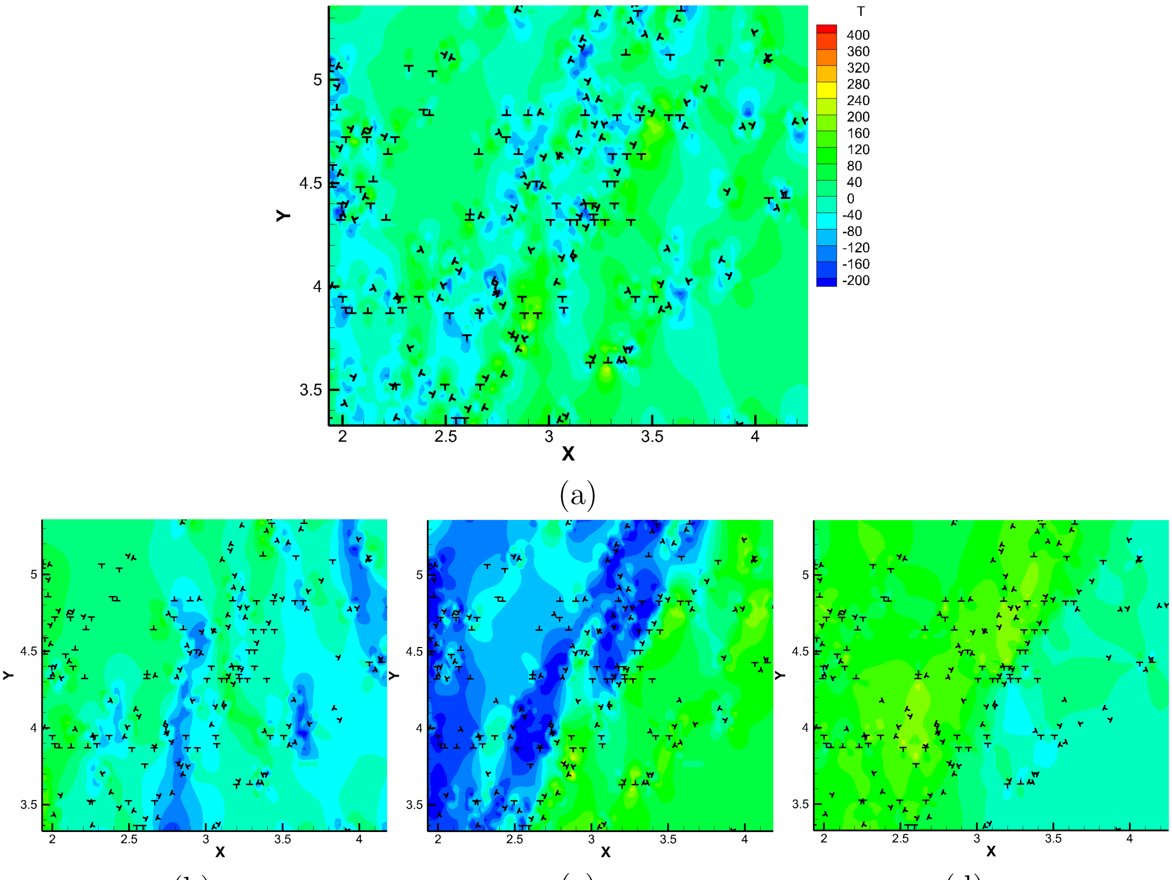

Figure 4.19: Contribution of dislocations on each individual slip system to the local σ_{yy} stress concentrations (MPa) shown in Fig. 4.18(b): (a) σ_{yy} due to all dislocations (120°+60°+0°); (b) σ_{yy} due to the 120° pyramidal slip system; (c) σ_{yy} due to the 60° pyramidal slip system; (d) σ_{yy} due to the basal slip system.

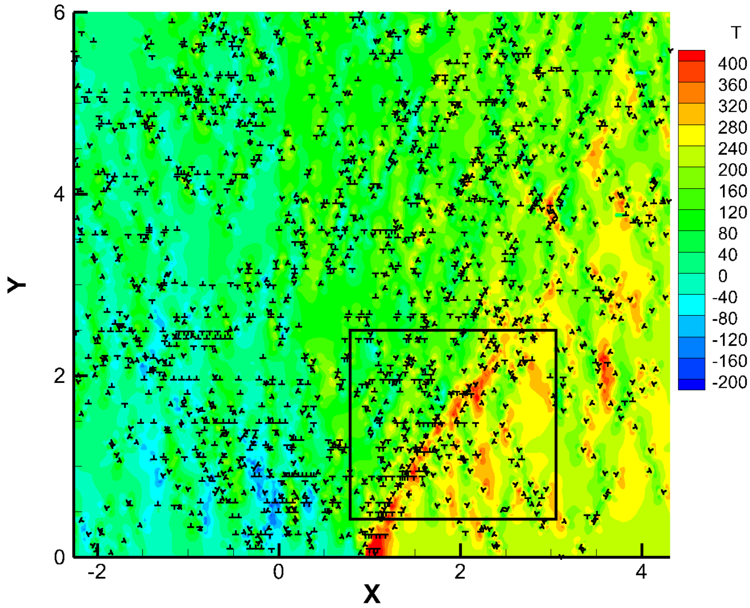

(a)

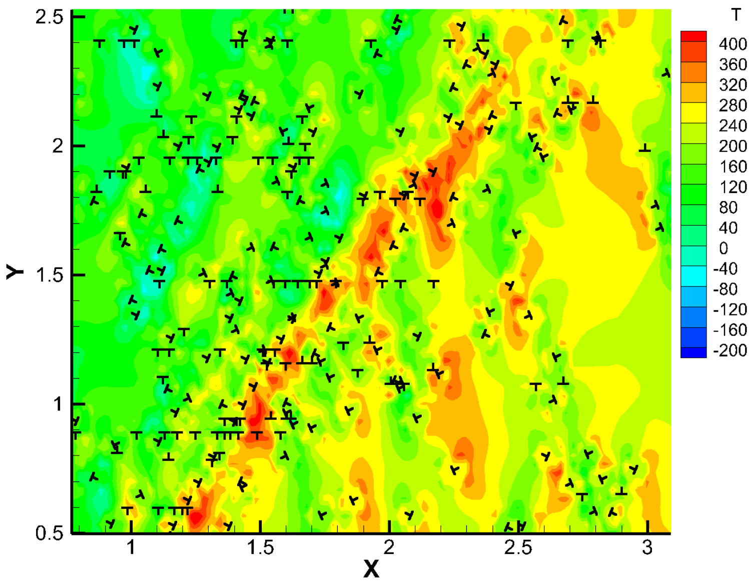

(b)

Figure 4.20: Normal stress contours, σ_{yy} (MPa) and dislocation distribution near toughness for an *anisotropic* material with $\tau_P^B = 30$ MPa, $\tau_P^P = 60$ MPa for the 4^{th} realization. (a) total normal stress field over a large scale, showing local stress concentrations microns from the crack tip along the 60° line; (b) total normal stress field in a region around a stress concentration.

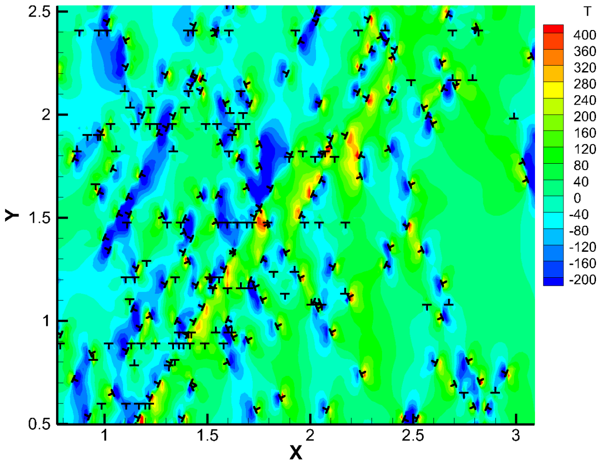

(a)

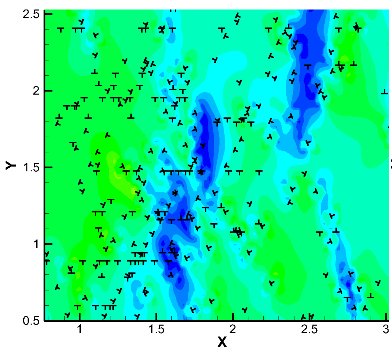

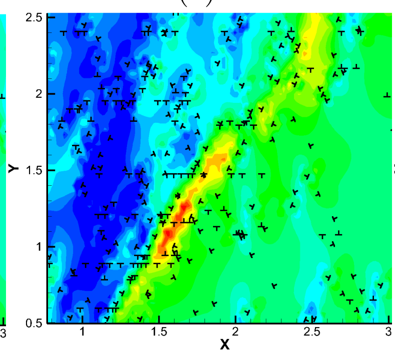

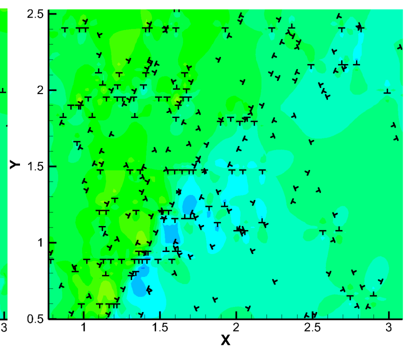

(b) (c) (d)

Figure 4.21: Contribution of dislocations on each individual slip system to the local σ_{yy} stress concentrations (MPa) shown in Fig. 4.20(b): (a) σ_{yy} due to all dislocations (120°+60°+0°); (b) σ_{yy} due to the 120° pyramidal slip system; (c) σ_{yy} due to the 60° pyramidal slip system; (d) σ_{yy} due to the basal slip system.

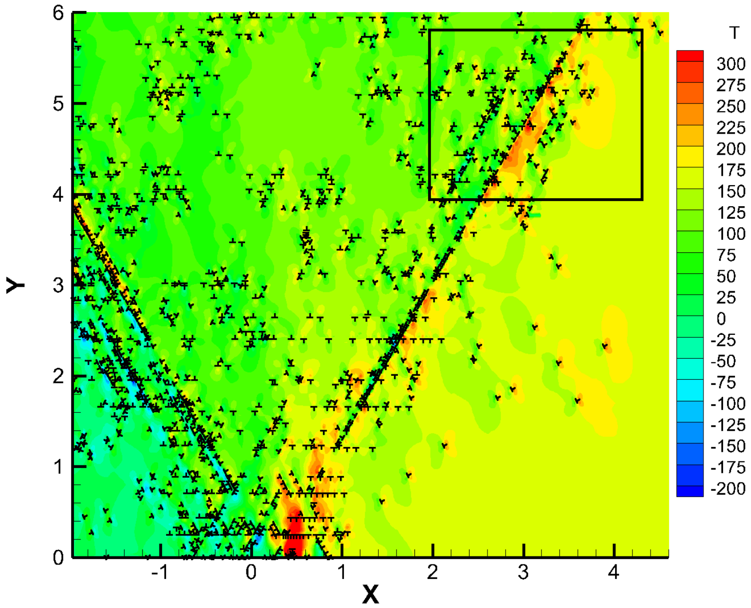

(a)

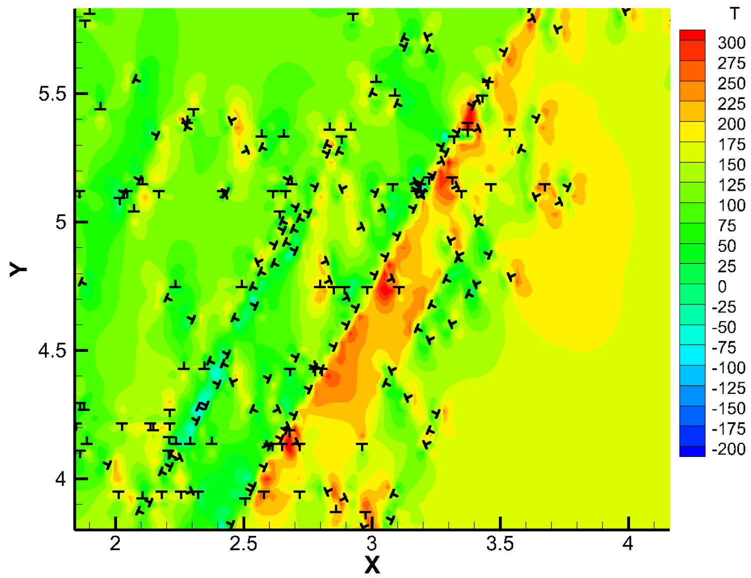

(b)

Figure 4.22: Normal stress contours, σ_{yy} (MPa) and dislocation distribution near toughness for an *isotropic* material with $\tau_P^B = \tau_P^P = 30$ MPa for the 4^{th} realization. (a) total normal stress field over a large scale, showing local stress concentrations microns from the crack tip along the 60° line; (b) total normal stress field in a region around a stress concentration.

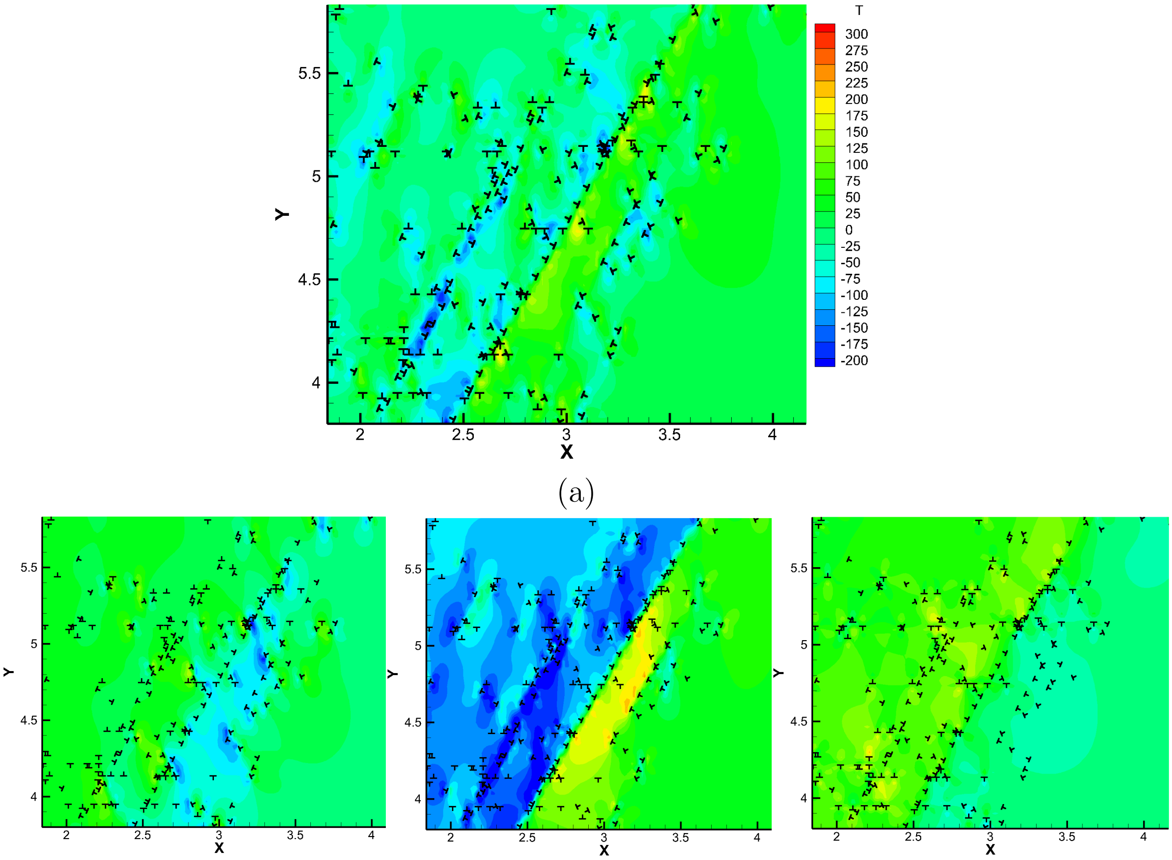

(a)

(b)

(c)

(d)

Figure 4.23: Contribution of dislocations on each individual slip system to the local σ_{yy} stress concentrations (MPa) shown in Fig. 4.22(b): (a) σ_{yy} due to all dislocations (120°+60°+0°); (b) σ_{yy} due to the 120° slip system; (c) σ_{yy} due to the 60° slip system; (d) σ_{yy} due to the 0° slip system.

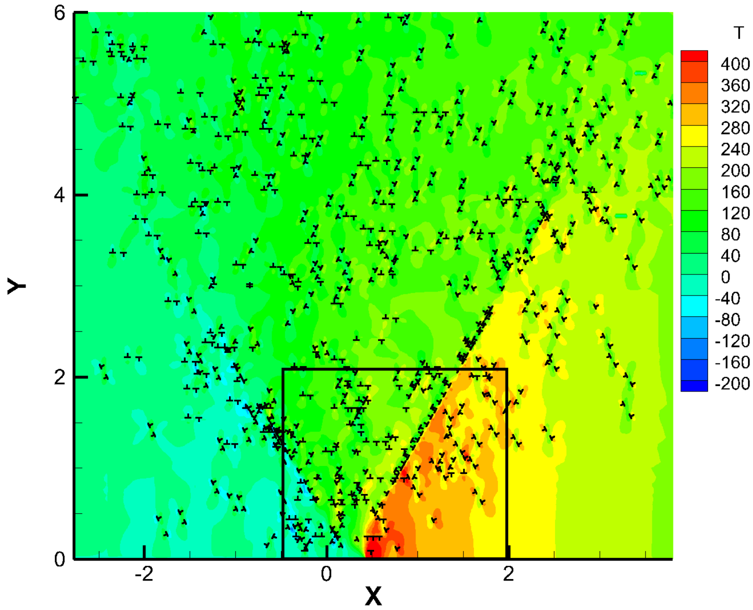

(a)

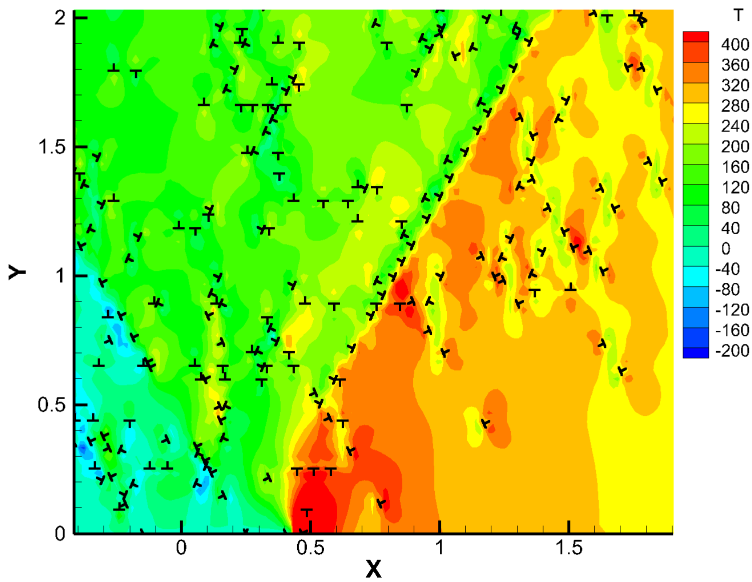

(b)

Figure 4.24: Normal stress contours, σ_{yy} (MPa) and dislocation distribution near toughness for an *isotropic* material with $\tau_P^B = \tau_P^P = 60$ MPa for the 4^{th} realization. (a) total normal stress field over a large scale, showing local stress concentrations microns from the crack tip along the 60° line; (b) total normal stress field in a region around a stress concentration.

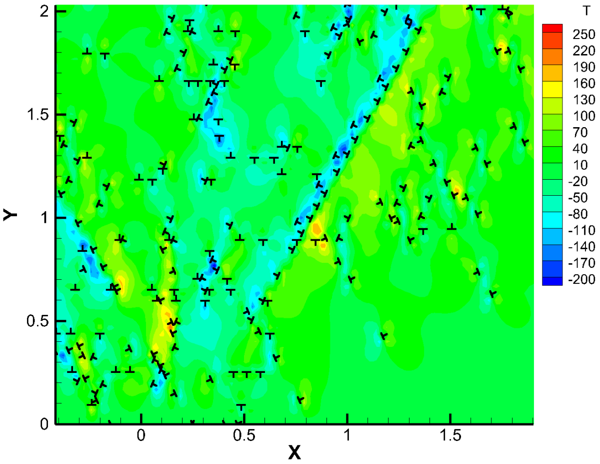

(a)

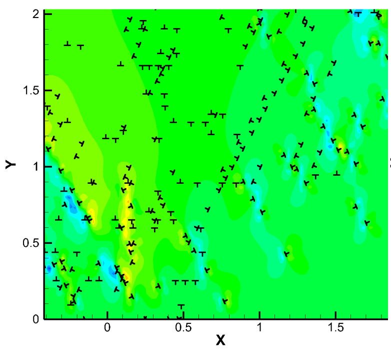

(b)

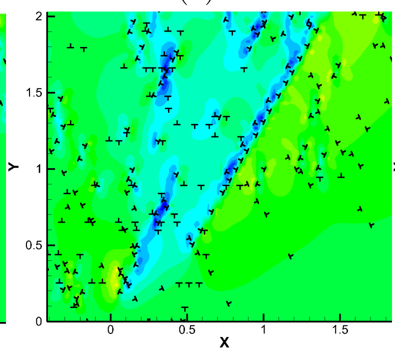

(c)

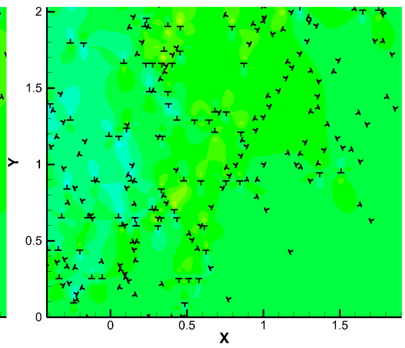

(d)

Figure 4.25: Contribution of dislocations on each individual slip system to the local σ_{yy} stress concentrations (MPa) shown in Fig. 4.24(b): (a) σ_{yy} due to all dislocations (120°+60°+0°); (b) σ_{yy} due to the 120° slip system; (c) σ_{yy} due to the 60° slip system; (d) σ_{yy} due to the 0° slip system.

Chapter 5

Scalings of Fracture Toughness with Material Properties

In Chapter 3, fatigue crack growth of a cracked particle in aluminum alloy matrix was investigated. Discrete dislocation demonstrated the effect of various microstructural features including micron-scale cracking, elastic mismatch and the particle−matrix interface. The crystal matrix is taken to be an elastic-perfectly plastic material with mechanical properties resembling aluminum. Plastic deformation is described by the standard discrete dislocation methodology which the yield stress of the matrix material is low, and is controlled by the strength of dislocation sources. Within this framework the aluminum matrix provides yield strength of 20-25 MPa while typical aluminum alloys have yield strength ranging from 200 MPa to 600 MPa. Gaining a quantitative understanding of material description in order to model fracture for realistic material parameters requires new insights and algorithms, Chakravarthy and Curtin (2010a). One key feature of our DD simulation is that the motion of dislocations along slip planes is impeded by obstacles of strength τ_{obs} having average spacing L_{obs}. The simulations demonstrate that macroscopic plastic flow is controlled by dislocation pileups occurring at obstacle leading to a uniaxial yield stress given by

$$\sigma_Y = \frac{1}{S}\sqrt{\frac{4\mu b}{\pi(1-\nu)}\frac{\tau_{obs}}{1.5L_{obs}} + \tau_s^2} \tag{5.1}$$

with S the Schmid factor. This obstacle controlled material model closely resembles precipitation hardened materials with high strength and low strain hardening rates, such as Al-2XXX, Al-6XXX and Al-7XXX alloys. Of most importance, Eq. 5.1 shows that the macroscopic yield stress σ_Y can be held fixed while the internal length scale and obstacle strength can be varied, permitting control of the material length scale L_{obs}.

A cohesive zone model along the crack surface is introduced to model fracture process. A finite element mesh must resolve the high stress and stress gradients in the vicinity of the crack tip as it move along the cohesive zone, Chakravarthy and Curtin (2011a). The minimum element size near the crack tip is limited by a cohesive zone length $\delta_c \sim \frac{E\phi_n}{\sigma_{coh}^2}$ where $\delta_c > 100$ nm and $\sigma_{coh} < 1$ GPa were used in Chapter 3. For realistic material properties the cohesive length is $\delta_n \sim 1$ nm requiring mesh on the Å scale corresponding a cohesive strength $\sigma_{coh} > 5$ GPa. Therefore adaptive meshing is required to move a simple uniform sub-Å mesh to capture crack growth on the order of micrometers.

A new superposition scheme for discrete dislocation plasticity, O'Day and Curtin (2004), is used for a computationally efficient solution of elastically *inhomogeneous* DD problems and the stability of crack opening. With the standard superposition scheme, a polarization stress term due to the elastic mismatch between the particle and the surrounding matrix requires more computational cost on each particle integration points of finite elements. For crack surface with cohesive zone model, the displacement field along the cohesive surface becomes unstable during the incremental solution when the characteristic opening length δ_n is on the order of magnitude of Burgers vector b, which arises when using realistic material properties. The new superposition method is similar to the Eshelby inclusion problem (Eshelby (1961)) where the inclusion stress induced by the dislocations in the matrix is transmitted through the tractions at the inclusion−matrix interface. With a Newton-Raphson (NR) iterative scheme incorporated into the new superposition framework, the instabilities of the displacement field of the cohesive surface can be eliminated.

Closer investigation of crack growth from small crack particles, but now using more realistic material properties under monotonic loading, yields a brittle-like material behavior. The cause of this low fracture toughness for the short crack problem was ambiguous. We attribute it to a combination of high yield stress and elastic properties, such as Young's modulus. These results inspired the further investigation of the Mode-I long crack problems, where previous work had used a Ni-alloy material Chakravarthy and Curtin (2010b) with yield stress and cohesive properties comparable to our material parameters but with a much larger Young's modulus. We then also analyzed the fracture toughness using the classical dislocation shielding of Lin and Thomson (1986) to rationalize the measured fracture toughening. Since the cohesive crack is used in our model which is not an ideal sharp crack, care must be taken to account for any effects due to the cohesive crack model. We thus employed the general solution to dislocation shielding of a cohesive crack proposed by Bhandakkar et al. (2010) as well as that obtained from the sharp-crack Lin-Thomson solution. Our simulations show the fracture toughness has additional dependencies on the product μb and on K_0, which arise through the mutual elastic interaction of the crack and the dislocations, and thus influence the overall evolution of the dislocation structure.

5.1 Short cracked particle in symmetrically-bounded matrix

Certain aspects of the inclusion problem are computationally expensive. The largest expense arises from the calculation associated with the polarization stress term, which must be evaluated at all integration points within the inclusion elements and explicitly requires the stress field from each dislocation. Clearly this can become computationally intensive when either (i) the number of inclusion elements is large or (ii) the number of dislocations is large. The symmetric boundary problem reduces the cost to a quadrant of the full sample, which directly saves on computational time and storage. The microstructure is idealized to the cell shown in Fig. 5.1(a), with each cell

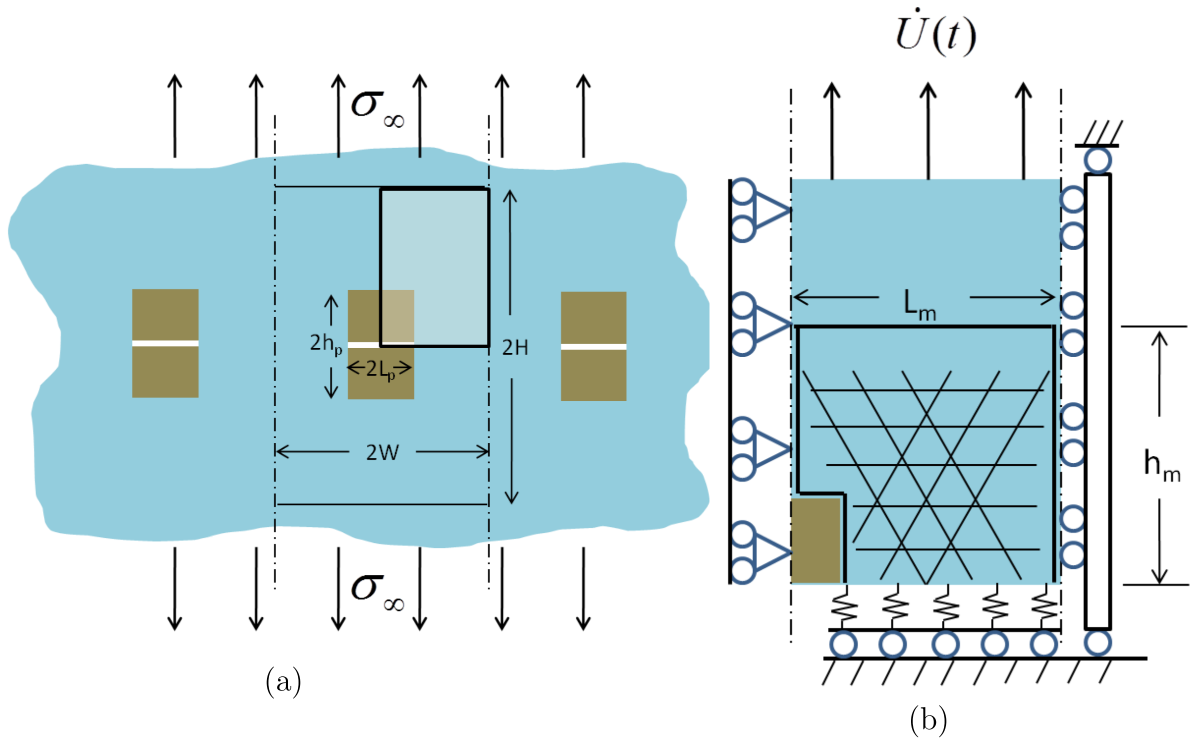

Figure 5.1: (a) Plane strain model of a material containing rectangular particles. (b) Sketch of the analyzed specimen with the imposed boundary conditions.

containing a rectangular elastic particle. Plane strain conditions with infinite bond strength are assumed for all analyses. The rectangular cell of height $2H$ and width $2W$ contains a rectangular particle of height $2h_p$ and width $2L_p$. The specific boundaries of the specimen are given in Fig. 5.1(b). We use $W = 15$ μm, $H = 500$ μm, $L_m = 15$ μm, $h_m = 30$ μm and $L_p = 1.5$ μm, $h_p = 3$ μm with the particle $x = 0 - L_p$

and $y = 0 - h_p$. The symmetric boundary conditions on the cell quadrant are

$$\dot{u}_x = \quad 0 \quad , \quad \dot{T}_x = 0 \quad on \ x = 0 \tag{5.2a}$$

$$\dot{u}_x = \quad \dot{U}_{MPC} \quad , \quad \dot{T}_x = 0 \quad on \ x = W \tag{5.2b}$$

$$\dot{u}_y = \quad \dot{U}(t) \quad , \quad \dot{T}_y = 0 \quad on \ y = H \tag{5.2c}$$

The aggregate is subject to plane strain tension with a displacement rate $\dot{U}(t)$ on the top surface $x = H$. Deformations for which the straight lines bounding each cell remain straight on $x = W$ and for which straight lines connecting the centers of the cells, $x = 0$, remain straight are permitted. To do so, the surface at $x = 0$ is fixed and the displacement along $x = W$ is imposed by the unique boundary condition *multi-point constraints*. The conventional approach to implementing multi-point constraints (MPC) is often obtained by either the Lagrange Multiplier or the Penalty method. Here we use the Penalty method because it does not require extra variables. Implementation of the matrix remains the same, independent of size for the given constraints (see Appendix A). The imposed stress σ_∞ follows as

$$\sigma_\infty = \frac{1}{W} \int_0^W T_y(x, H) dx \tag{5.3}$$

The crack length of the initial cracked particle is $a = L_p$. For multiple cracks in the homogeneous elastic material as in Fig. 5.1(a), the applied stress σ_∞ to Mode-I stress intensity factor, K_I is

$$K_I = \sigma_\infty \sqrt{2W \tan \frac{\pi a}{2W}} \tag{5.4}$$

For all cases, a uniform displacement rate $\dot{U}(t)/H = 250$/s is imposed. Crack growth is modeled through a cohesive surface along $y = 0$ with the initial crack tip located at $x = L_p$. By symmetry $T_x = 0$ along the cohesive surface, T_y has a universal binding form (Rose et al. (1981)). The cohesive properties were taken as $\sigma_{coh} = 5$ GPa and $\delta_n = 0.0736$ nm, yielding a work of fracture $\phi_n = 1$ J/m^2 and K_0=0.28425 MPa$\sqrt{\text{m}}$.

Thus the characteristic cohesive zone size $\delta_c = \pi E_m \phi_n / 8\sigma_{coh}^2$ is 1 nm.

5.1.1 Superposition implementation

Both the inclusion and boundaries can be handled via a superposition of (i) the Discrete Dislocation (DD) sub-problem, subjected to fixed displacement-type boundary conditions and (ii) the Elastic (EL) sub-problem, subjected to the full field boundary condition as illustrated in Fig. 5.2.

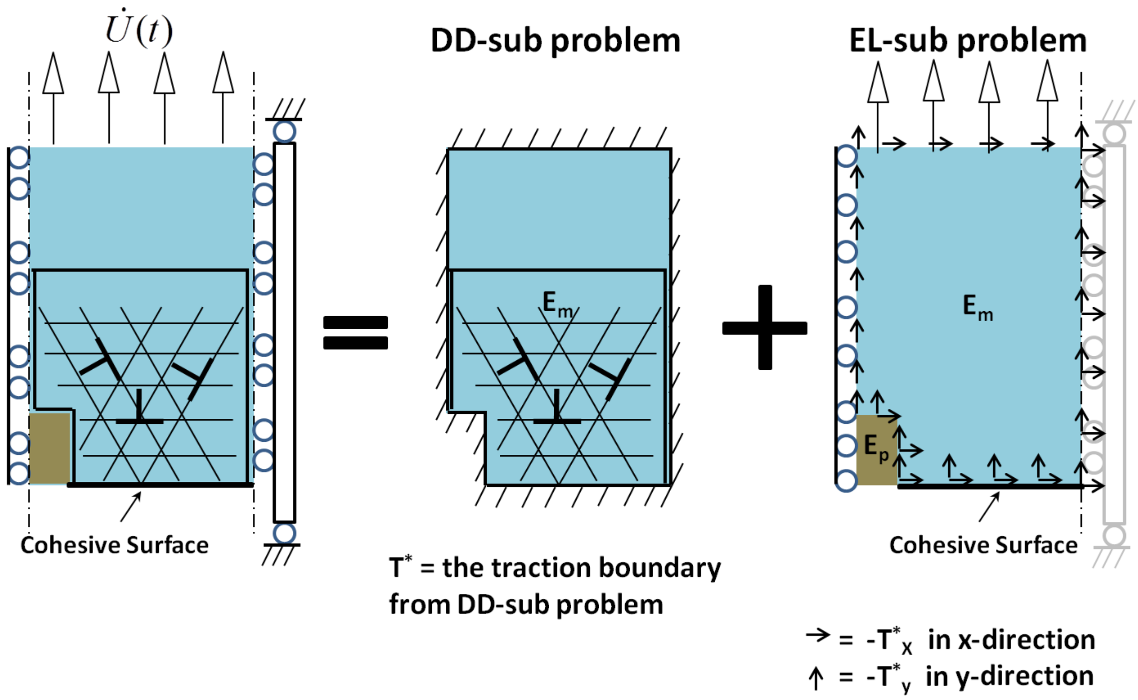

Figure 5.2: An inclusion model problem with symmetric boundaries and the cohesive zone model at the crack surface; decomposition into DD and EL sub-problems.

The DD sub-problem is limited to the area of discrete dislocation activity. The inhomogeneous elastic region is excluded from the sub-problem. The DD sub-problem is subject to zero displacement boundaries, which are enforced universally between the matrix and the inclusion. By keeping the DD sub-problem homogeneous, the polarization stress vanishes. The incremental DD sub-problem follows exactly as described by the standard superposition framework of Van der Giessen and Needleman (1995). A subsequent outcome of the DD sub-problem following each time increment solution is a traction $-\mathbf{T}^*$ along the constrained boundary as a consequence of dislocations in the matrix.

The EL sub-problem is a model of the entire structure excluding dislocations, subjected to all boundary conditions. Contribution of dislocation network in any plastic region is transmitted to the remainder of the structure via an additional body force $-\mathbf{T}^*$ obtained from the DD sub-problem (see Fig. 5.2). At the symmetric boundary, the additional body forces can be omitted normal to the symmetric constraints; the tractions in x-direction $-\mathbf{T}^*_\mathbf{x}$ on the left boundary and the tractions in y-direction $-\mathbf{T}^*_\mathbf{y}$ on the top. The right hand side boundary condition is a unique multi-point constraint (MPC), which is accomplished by internal constraints, the same as the cohesive surface and the inclusion interface. Therefore the additional body force or $-\mathbf{T}^*$ from the DD sub-problem is completely consistent within this framework.

5.1.2 Validation

Before investigating new problems, we first verify the symmetric boundary methodology through a conventional tensile test. A tensile specimen $W \times H = 1000 \times 1000$ μm^2 with a centered rectangular particle $L_p \times h_p = 2.5 \times 5$ μm^2 is illustrated in Fig. 5.3. Typically the influence of symmetric boundaries can produce an image force on dislocations which approach the boundary. For comparison purposes between a full specimen and a specimen quadrant with symmetric boundaries, the resolved shear stress on the fixed dislocation A is verified (see Fig. 5.3). The matrix and the particle are taken to be elastic materials with Young's moduli E_m and E_p, respectively. The dislocation dipoles are symmetric about the x-axis and y-axis in the full specimen, for which the symmetric problem is illustrated in Fig. 5.3 on the right. The fixed dislocations are blocked by obstacles at each site near the dislocations. For the symmetric boundary of the specimen quadrant, the displacement is fixed in the x-direction at the left boundary and is free in the y-direction. Special cohesive elements are used to enforce the symmetry by placing very high cohesive strength along the bottom

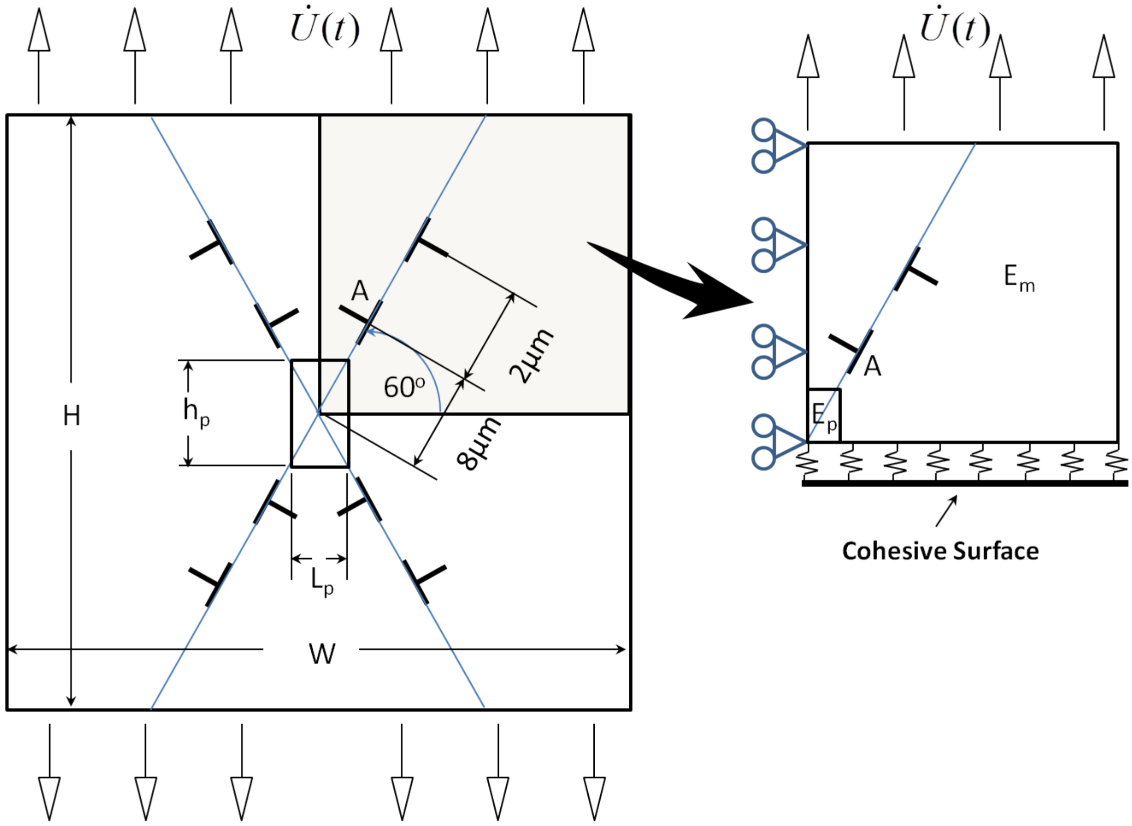

Figure 5.3: A tensile specimen with a centered rectangular particle and dislocations surrounding the particle; a comparison of the boundary effect between the full specimen and the specimen quadrant with symmetric boundaries through the force exerting on the dislocation A.

surface. Only one dislocation dipole is used in this symmetric problem. In the full specimen with the standard superposition framework, the polarization stress needs to be evaluated if there is modulus mismatch, $E_p \neq E_m$. Therefore to include the effect of modulus mismatch into this validation, a particle that is elastically stiffer than the matrix, $E_p = 5E_m$, is also examined. Fig. 5.4 shows the net resolved shear stress acting on the dislocation A. Both modulus ratios yield similar results when comparing the full solution with single quadrant symmetric boundary solution. Moreover the elastic mismatch effect on dislocation A shows that a lower modulus ratio has a steeper slope of $\tau_{RSS}/\sigma^{\infty}$, see Fig. 5.4. This means that the applied load is transferred from the weaker matrix, across the matrix/particle interface, to the stiffer particle resulting in lower net resolved shear stress on the dislocation A. These results confirm

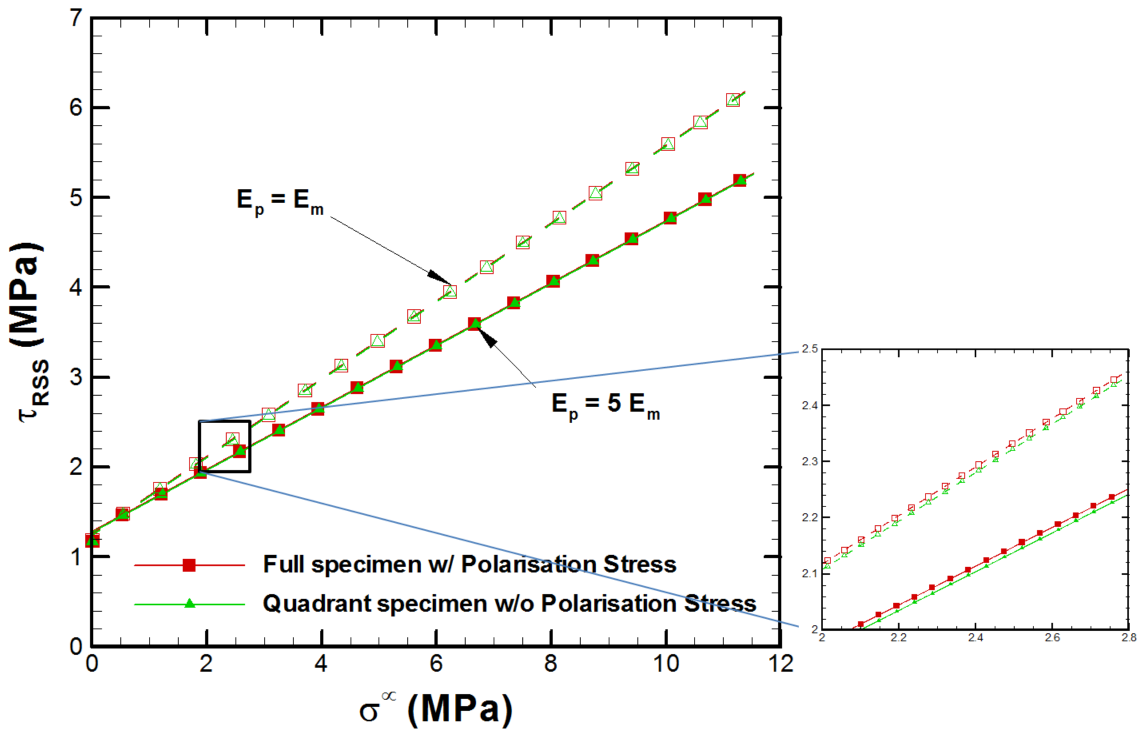

Figure 5.4: resolved shear stress exerting on the dislocation A (see Fig. 5.3) as a function of applied tensile stress for $E_p = E_m$ and $E_p = 5E_m$: comparison of actual boundary condition and the symmetric boundaries.

the validity of these techniques applied to the symmetric boundary.

5.1.3 Adaptive meshing

In previous chapter, the moving mesh method was used in long crack simulations. To avoid computational expense in the decomposition of the stiffness matrix with every remeshing operation, the finite element mesh is fixed while dislocations and all field variables are moved in the opposite direction to the crack growing. This moving mesh framework cannot be applied to the short crack with a symmetric boundary due to the symmetrical crack growth and the fixed particle. Since there are additional stress fields of image dislocations with respect to the line of symmetry, the distance from the crack tip to the symmetric boundary is significant to the development of dislocations around the crack tip. Essentially a fine mesh must be enforced near the boundaries where dislocations approach, i.e. the vicinity of the crack tip and the particle−matrix interface, to obtain the precise $\mathbf{T}^*$ from the DD sub-problem. The standard adaptive meshing method involving remeshing is thus required in order to keep the fine mesh near the particle−matrix interface and near the moving crack tip.

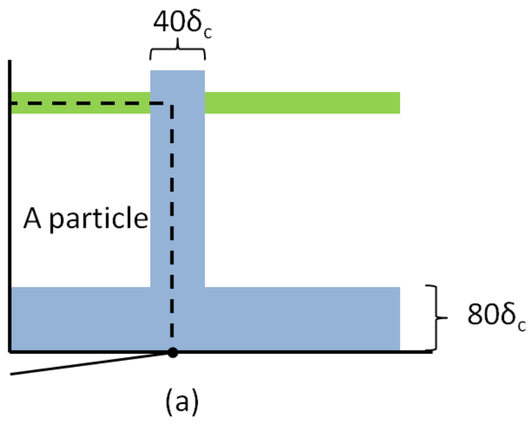

Figure 5.5: Schematic illustration of remeshing for a cracked particle in the matrix problems with symmetric boundaries (a) the initial mesh where the crack tip is at the interface of a particle and the matrix (b) remeshing according to the current crack tip.

In our specific case with a cracked particle, a uniform mesh size of $\Delta x = \delta_c/4$ is employed over a region that extends $40\delta_c$ ahead of the initial crack tip along the horizontal axis and $80\delta_c$ above the crack surface along vertical axis, shown in Fig. 5.5(a) as blue strip. The mesh size increases smoothly with increasing distance to the crack tip. The uniform mesh is extended for $10\delta_c$ along the particle−matrix interface, represented by the green strip in Fig. 5.5(a). Initially this uniform mesh is only placed at the top particle−matrix interface since the right interface is enclosed by the uniform mesh of the crack tip. Once the crack tip moves forward, the crack tip and the particle−matrix interface are not in the same position. Then another meshing structure is required which is demonstrated in Fig. 5.5(b). Here, the right interface has extended the uniform mesh for $10\delta_c$ at the particle−matrix interface and the width of the uniform mesh at the crack tip is about $40\delta_c$. This type of remeshing is implemented to operate automatically when the crack grows forward at some distance. The actual mesh is illustrated in Fig. 5.6(a) and 5.6(b) for the crack tip at the particle−matrix interface and for the crack tip moving away from the particle−matrix interface, respectively.

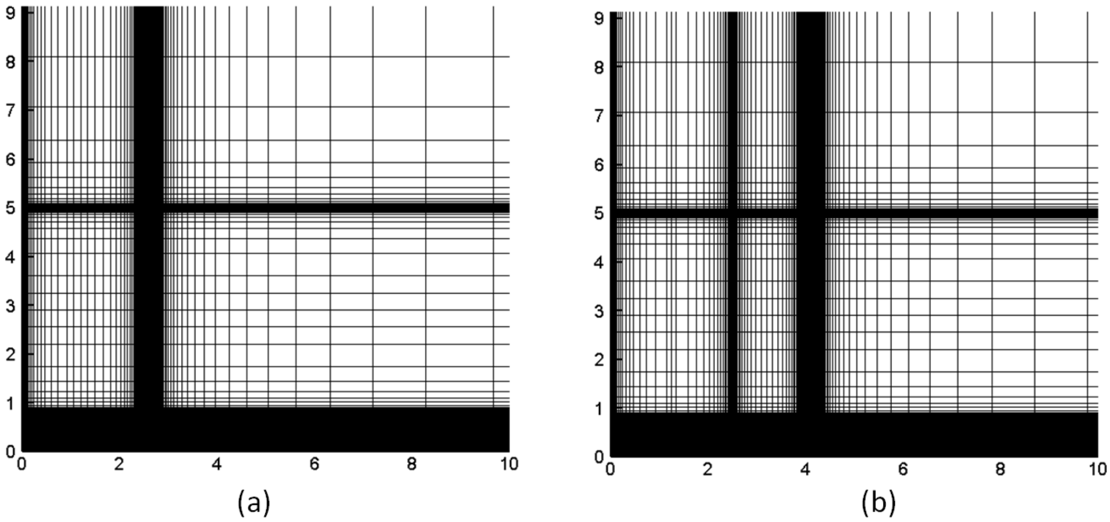

Figure 5.6: Adaptive mesh movement as the crack tip moving away from the particle (a) the initial mesh where the crack tip is at the interface of a particle and the matrix, at $x = 2.5$ μm (b) remeshing according to the current crack tip, at $x = 4$ μm.

5.1.4 Results

In this section we investigate the toughness with the more-realistic matrix material properties summarized in Table 3.1: (i) material A, an initially cracked single crystal (ii) material B, a cracked particle with the modulus ratio $E_p/E_m = 1$ and (iii) material C, a cracked particle with the modulus ratio $E_p/E_m = 5$. So, we first consider the material A under monotonic loading to study the toughness of a single crystal with a short crack.

The material properties and the material description for the DD simulation performed in Chapter 3 are used in this section except that the matrix yield stress σ_Y is 500 MPa which is controlled by the obstacle spacing $L_{obs} = 100$ nm and $\tau_{obs} = 517.52$ MPa according to Eq. 5.1. Fig. 5.7 shows the R-curve of material A compared to a brittle-like material. Unexpectedly, material A with the yield stress of 500 MPa exhibits brittle behavior. In material A, small amount of crack growth occurs before reaching the critical stress intensity K_0. It is possible that the local stress concentrations from the dislocations which are pinned nearby the crack tip increase the stress level leading the crack to grow. Once the crack tip moves forward, the stress level at the former tip position is still greater than the current tip position. Then the crack tip position could take place at the former position due to opening sensitivity in the cohesive zone law. This is a numerical error in calculations when defining the tip, especially when a sharp-peaked $(T - \Delta)$ law is used, i.e. very high cohesive strength (σ_{coh}) and very small characteristic opening length (δ_n). In the simulations, the stress intensity factor is computed from the applied tensile stress following Eq. 5.3. Unstable crack growth exhibits a slope in $K_I/K_0 - x$ plot that is relevant to a given loading rate. Lower loading rates decrease the slope. Although higher Young's modulus of 170

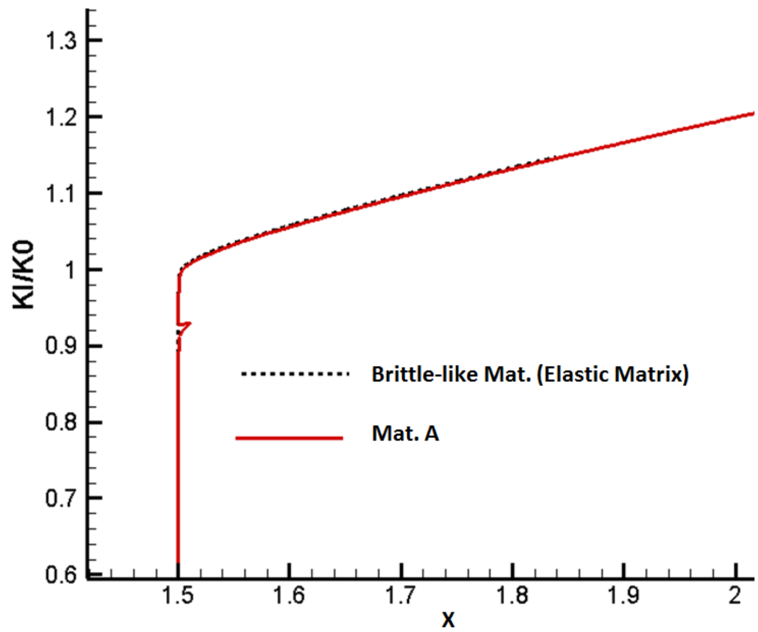

Figure 5.7: Normalized stress intensity K_I/K_0 versus crack position(μm) of single crystal under monotonic loading for material A(a red solid line) and elastic material (black dashed line).

MPa is used to follow the material properties in Chakravarthy and Curtin (2010b), the fracture toughness of the material with high yield stress is still equal to K_0. From the simulation, such a higher yield stress matrix has lots of pileup dipoles in which the dislocations cannot pass through the obstacles. Consequently the plastic dissipation is much less since the dislocation dipoles and/or pileup dipoles themselves do not significantly shield the crack tip. The question is then what causes the low fracture toughness for the short crack problem with high yield stress? In Chakravarthy and Curtin (2010b) Ni-alloy material was investigated for Mode-I long crack problem where the yield stress and cohesive properties are similar to our material parameters, except with the Young's modulus being higher. The fracture toughness for materials with yield stress of 500 MPa was more than K_I/K_0 =5. The results stimulate us to further examine the toughness of materials with such high yield stress but lower Young's modulus for the long crack problem alone. Finally we found, as discussed below, that the modulus of material has a significant effect on fracture toughness through μb and K_0 when the yield stress and cohesive properties are held fixed.

5.2 Scaling in fracture toughness

Here we choose a long crack problem of Mode-I to obtain the fracture toughness for materials A-E, each with parameters as listed in Table 5.1. The primary parameters varied are the Young's modulus E, the fracture energy ϕ_n, and the Burgers vector b. Material A is a baseline material where the Young's modulus is 170 GPa while a Young's modulus of 72 GPa is used for materials B-E. Material B is the material used in the previous section. The 2d-DD model with the obstacle-controlled yield based on the evolution of dislocation pileups is used. Dislocations pinned at obstacles can escape when the resolved shear stress on the dislocation is greater than the obstacle strength. If the density of the obstacles and/or strength of the obstacles are higher than that of the sources, we anticipate that the formation of pileups at the obstacle controls the flow. This is one key feature of controlling the macroscopic plastic flow so that the uniaxial tensile yield stress can be predicted by Eq. 5.1 for a given obstacle spacing L_{obs} and obstacle strength τ_{obs}. L_{obs} is a material length scale in this model. The fracture energy ϕ_n in material C is changed from 1 to 2.3611 J/m^2 to hold K_0

the same as in material A. Both material B and C have the same μb but with a value different from material A. Materials D and E have E=72 GPa but have the same μb as in material A by using a larger b= 0.59 nm. In material E, the fracture energy and b are changed to hold both K_0 and μb the same as in material A.

From Wei and Hutchinson (1997)'s SGP Mode-I crack growth in a homogeneous materials, the SGP is controlled by the parameter l, representing the length over which non-uniform straining contributes to material hardening (l=0 corresponds to the size-independent continuum plasticity). When l is small relatively to other characteristic lengths (such as plastic zone size at R_0) hardening due to strain gradients is expected to be negligible. Clearly a ratio of L_{obs}/R_0 for material A-E are greater than 1. Consequently the strain gradient within the internal length scale L_{obs} strongly influences the fracture toughness. Chakravarthy and Curtin (2010b) show that the fracture toughness decreases with increasing L_{obs}. Therefore, L_{obs}=100 nm is fixed for all materials A-E, and the yield stress is varied by changing the obstacle strength only. In Chakravarthy and Curtin (2010b), a master curve of fracture toughness

Table 5.1: Material properties for material A-E: $\overline{\tau}_{nuc}$=50 MPa, L_{obs}=100 nm, ρ_s=66 /μm^2 used for all materials and in each yield stress σ_Y, τ_{obs} obtained from Eq. 5.1 and $R_0 = \frac{1}{3\pi(1-\nu^2)}\frac{E\phi_n}{\sigma_Y^2}$.

	Material	A	B	C	D	E
	E(GPa)	170	72	72	72	72
	b(nm)	0.25	0.25	0.25	0.59	0.59
	μb(Pa·m)	15.977	6.7669	6.7669	15.977	15.977
	ϕ_n(J/m^2)	1.0	1.0	2.3611	1.0	2.3611
	K_0(MPa$\sqrt{m}$)	0.43678	0.28425	0.43678	0.28425	0.43678
σ_Y=500 MPa	τ_{obs}(MPa)	219	518	518	219	219
	R_0(nm)	81	34	81	34	81
σ_Y=600 MPa	τ_{obs}(MPa)	321	758	758	321	321
	R_0(nm)	56	24	56	24	56
σ_Y=700 MPa	τ_{obs}(MPa)	442	1042	1042	442	442
	R_0(nm)	41	18	41	18	41

versus σ_{coh}/σ'_Y was obtained where σ'_Y is the near-crack-tip yield stress due to the non-uniform stress field. The near-crack-tip yield stress in our cases (L_{obs}=100 nm) is about equal to the yield stress with zero gradient. From the master curve, the fracture toughness can be approximated from σ_{coh}/σ'_Y = 5 GPa/500 MPa = 10 giving K_{IC}/K_0 $\approx$5. With the lower Young's modulus, μb and K_0 are decreased but τ_{obs} is increased. We believe that the change of K_0 does not affect the normalized fracture toughness, K_I/K_0 and the effect of varying μb on the yield stress is accounted for by altering τ_{obs} from Eq. 5.1. So, the fracture toughness is expected to be similar for all materials with the same yield stress and the same L_{obs}. Each material has four realizations of random source/obstacle distribution for each yield stress to illustrate the stochastic variations in the fracture behavior. Fig. 5.8 shows R-curves for material A-E. In each realization, the distribution of sources and obstacles is exactly the same for each yield stress where the obstacle strength is varied only. Fig. 5.8(a-d), (e-h) and (i-l) are results of yield stress 500 MPa, 600 MPa and 700 MPa, respectively. Overall the fracture toughness tends to decrease as the yield stress increases. Interestingly, only materials A and E approach the expected toughness from the master curve in Chakravarthy and Curtin (2010b), although the toughnesses in some realizations cannot reach the expected value due to stochastic variations, particularly for realization 4. Also, the R-curves of materials A and E tend to follow each other in all cases. The fracture toughnesses for materials B, C and D never approaches the expected value. However, the fracture toughnesses are nonetheless similar for each source and obstacle distribution. This implies that the toughening is strongly influenced by both μb and K_0.

In an attempt to extract material parameters that are important to fracture toughness, we tried using the dimensionless analysis using the dimensionless groups in Deshpande et al. (2003b), such as $\phi_n/(\sigma_Y b)$, etc., but those dimensionless groups cannot introduce any interesting trends on the toughness in our materials A-E. Probably there are not enough variations of μb and K_0 to characterize the toughness, and the variation of fracture toughness for each random distribution is large. Therefore data

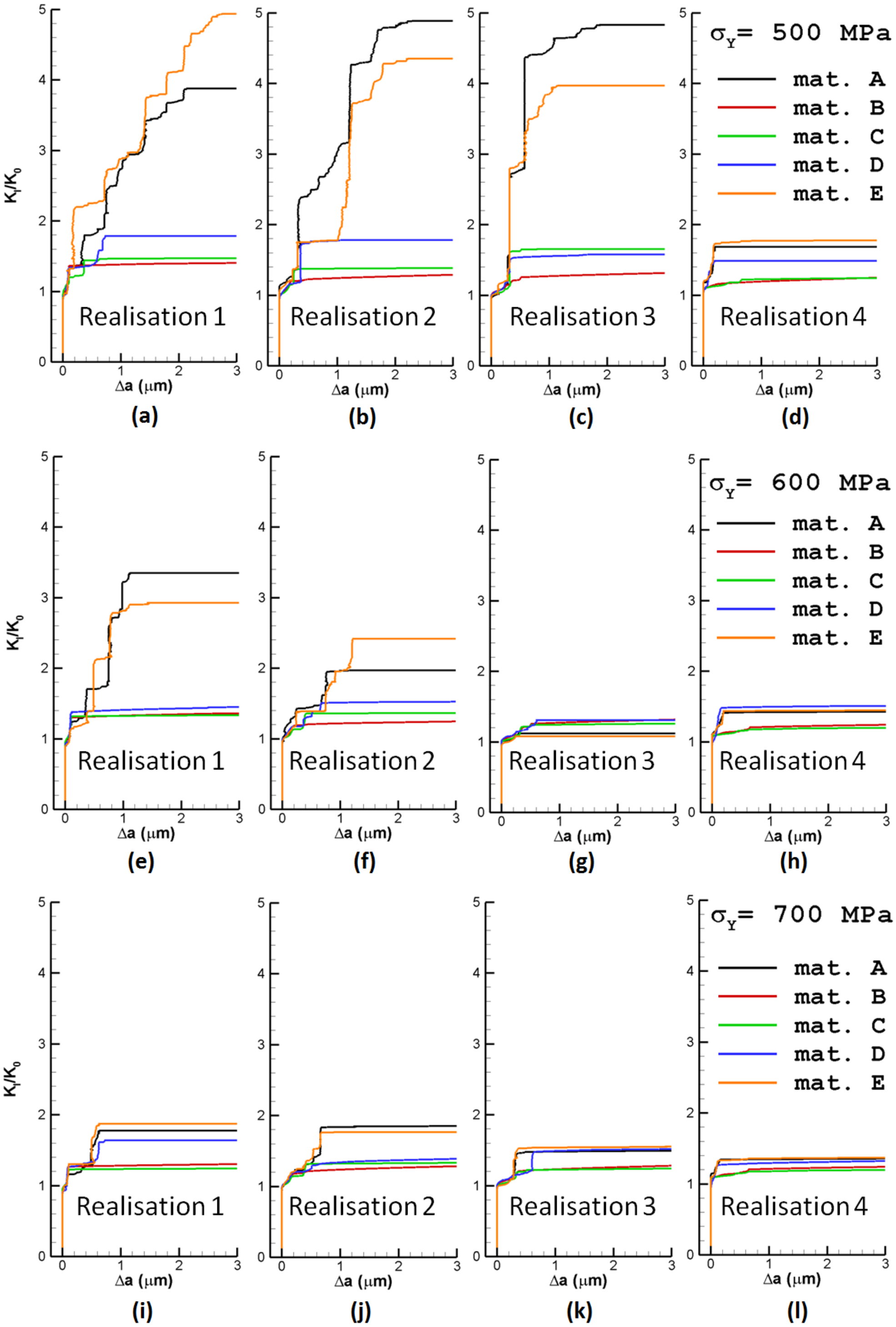

Figure 5.8: Mode-I crack growth of material A-E in various cases of yield stress for four realizations; (a)-(d) σ_Y= 500 MPa ;(e)-(h) σ_Y= 600 MPa; (i)-(l) σ_Y= 700 MPa.

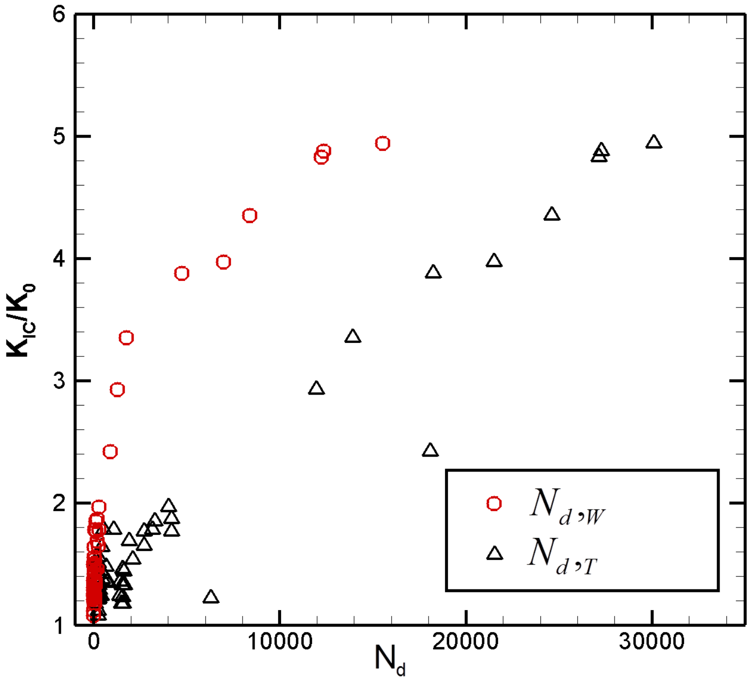

Figure 5.9: The normalized fracture toughness as a function of the number of dislocations (N_d). $N_{d,W}$ and $N_{d,T}$ are the number of dislocations in the plastic zone and in the entire specimen, respectively.

analysis is difficult. However, it is clear that μb and K_0 play an important role in material toughening even though we have not found the underlying reason for these dependencies.

As regards Lin and Thomson (1986), the crack tip shielding that gives rise to the toughness depends only on the number of dislocations and the dislocation positions with respect to the crack tip. From the dislocation shielding solution of Lin and Thomson (1986), the effective stress intensity factor K^{eff} at the crack tip is expressed as

$$K_I^{eff} = K_I^{\infty} - \Delta K_I^{LT} \tag{5.5a}$$

$$\Delta K_I^{LT} = \sum_{j=1}^{N_d} \frac{\mu b}{2(1-\nu)\sqrt{2\pi R_j}} f_1(\phi_j, \theta_j) \tag{5.5b}$$

$$f_1(\phi_j, \theta_j) = \sin\theta_j \cos(\phi_j - 3\theta_j/2) + 2\sin\phi_j \cos(\theta_j/2) \tag{5.5c}$$

where K^{∞} and ΔK_I^{LT} are stress intensity factor from the externally imposed loading and dislocation shielding, respectively. N_d is the number of dislocations shielding the crack. In Eq. 5.5, R is the distance to the dislocation from the crack tip, θ is the angle measured from the tip and ϕ is the slip angle. $f_1(\phi_j, \theta_j)$ is a function of angular dependence of shielding with respect to the tip. The crack is said to be shielded by dislocations when ΔK_I^{LT} >0 and anti-shielded when ΔK_I^{LT} <0. Crack growth occurs when K_I^{eff} reaches a critical value K_0. Fracture toughness, K_{IC}, is the applied stress intensity factor, K^∞, at which the unstable crack growth occurs without any load increase. From Eq. 5.5 the dislocations shielding in all simulations can also be computed through $K_I^\infty - K_0$.

Fig. 5.9 shows the plot of K_{IC}/K_0 as a function of the number of dislocations for material A-E in various yield stresses. $N_{d,W}$ and $N_{d,T}$ are the number of dislocations in the plastic zone and in the entire specimen, respectively. The number of dislocations in the plastic zone is counted within the plastic zone radius including a plastic wake, see Fig. 5.10. The plastic radius R_p is given as

$$R_p = \frac{1}{3\pi} \frac{K_I}{\tau_Y^2} \tag{5.6}$$

where $\tau_Y = S\sigma_Y$ and S is the Schmid factor. For our cases with S=0.433, this plastic zone radius extends about 5 times by using τ_Y instead of an apparent isotropic σ_Y to avoid zero dislocation in counting. It shows that the dislocation shielding depends on the number of dislocations and the smooth curve of $K_{IC}/K_0 - N_d$ can be obtained when counting a number of dislocations in the plastic zone only, as seen in Fig. 5.9. If μb and K_0 only influence the fracture toughness through the dislocation population, the toughness could be computed directly from the instantaneous dislocation structure at the unstable point of crack growth. From Lin-Thomson solution, Eq. 5.5, the applied stress intensity from dislocation shielding (K^{LT}) is obtained by

$$K^{LT} = K_0 + 2\Delta K^{LT} \tag{5.7}$$

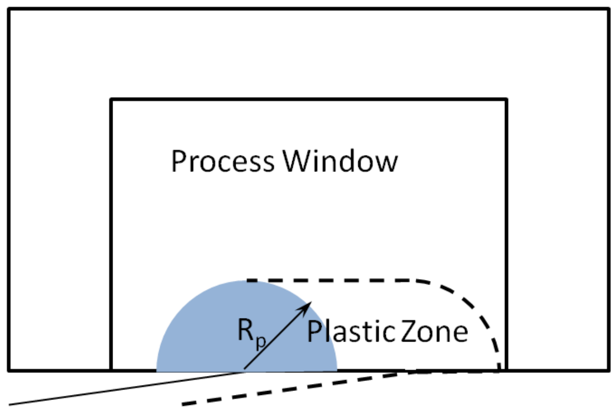

Figure 5.10: The plastic zone for the crack extension including a wake layer (within the dashed line). $R_p = \frac{1}{3\pi}\frac{K_I}{\tau_Y^2}$ is used to extend on purpose of non-zero dislocations counting.

The factor of 2 reflects on the symmetry of dislocation structure to the crack plane. Fig. 5.11 demonstrates that overall fracture toughness computed from dislocation shielding are in good agreement with the toughness from the DD simulations. The deviation of fracture toughness among dislocation zone size is increased as the toughness increasing. In Fig. 5.9, despite the fact that the total number of dislocations are twice as large as those within the plastic zone, those additional dislocations surrounding the plastic zone have a small effect on the crack shielding, around 10-15% of the total shielding. This suggests that most plastic dissipation comes from the dislocations within the plastic zone while the dislocations outside the plastic zone are in the form of pileup dipoles which have small shielding effect. There is one peculiar data point at low toughness where a huge difference in dislocation shielding is found between counts of the total dislocations and the dislocations inside the plastic zone. The reason is that the total number of dislocations in this low toughness regime is very small and the plastic zone size is also very small, so that there are only a few dislocations in the vicinity of the crack tip. Thus, the small shielding by further dislocations plays a much larger role in this one case.

Recently, Bhandakkar et al. (2010) proposed a general approximate solution to dislocation shielding of a cohesive zone crack based on an asymptotic interpolation of

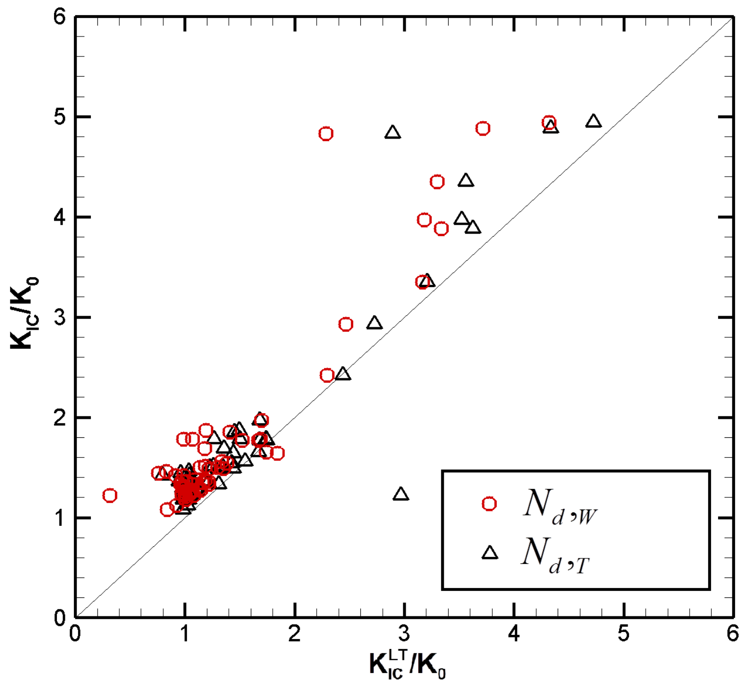

Figure 5.11: Comparison of the normalized stress intensity factor at fracture toughness computed from dislocations structures by Eq. 5.5b and Eq. 5.7 to DD results for material A-E. Red circles are K_{IC}^{LT}/K_0 calculated from the dislocation structure inside the plastic zone, see Fig. 5.10 and black triangles are K_{IC}^{LT}/K_0 calculated from the total dislocations.

the limiting solution for a Dugdale cohesive crack. They demonstrated that the asymptotic solution significantly improves upon the Lin-Thomson solution (for a sharp crack) in providing a more reasonable estimate of dislocation shielding of a cohesive crack. Moreover the dislocation shielding showed increasing deviations from Lin-Thomson predictions as the cohesive strength decreased. At the cohesive strength equal to 5 GPa, as used here, the difference of dislocation shielding is, however, less than 2%. Fig. 5.12 shows the fracture toughness from the dislocation structures obtained by Lin-Thomson solution versus those predicted by the asymptotic shielding solution for a cohesive crack. Expectedly, both predictions are in good agreement due to the high cohesive strength. Returning to examine the parameters that can affect fracture toughness, we again consider the interfacial work separation ϕ_n, Young's modulus E and Burgers vector b. Changes of ϕ_n and E can alter K_0 and changes of E and b (or μb) can scale the effect of the dislocation/dislocation and dislocation/crack

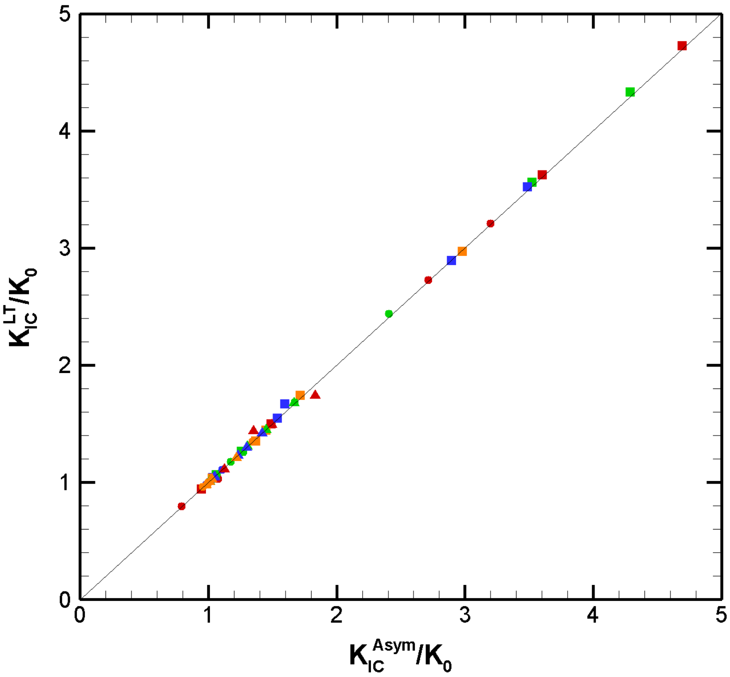

Figure 5.12: Comparison of fracture toughness counted on dislocation structures by Lin-Thomson solution versus those predicted by asymptotic shielding solution of cohesive crack.

interactions. In continuum plasticity, toughness predictions depend on K_0 only, such that the normalized fracture toughness K_I/K_0 is independent of variations in ϕ_n and E. The DD toughness predictions have a more complicated dependence that does not simply scale with K_0. With increasing ϕ_n, the dislocations are less able to induce the crack separation necessary for failure and the material toughness increases. It is not surprising that lower E and the same K_0 results in the lower toughness since the μb effect on the mutual elastic interaction (dislocation/dislocation and dislocation/crack interactions) is smaller. The decrease of μb leads to a reduction of both the crack shielding due to dislocation/crack interaction and the dislocation activities due to dislocation/dislocation interaction. Other evidence from the DD simulations demonstrates that the toughening depends on the dislocation shielding, as shown in Fig. 5.13. K_I/K_0 versus the crack extension Δa of material A for σ_Y=500 MPa in the first realization compares with the one obtained from the dislocation shielding of Lin-Thomson along the load increment. Although there is a fluctuation due to

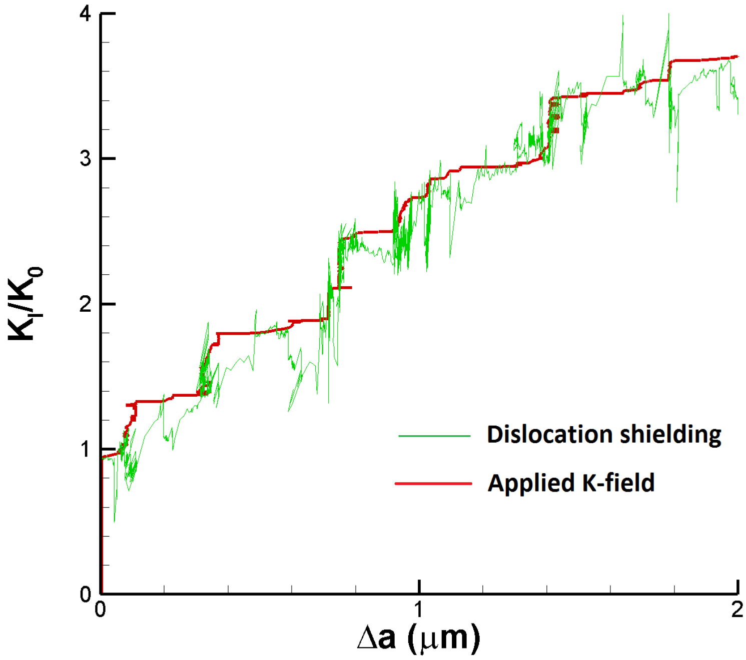

Figure 5.13: Comparison of K_I/K_0 versus the crack extension Δa of material A for σ_Y=500 MPa in the 1^{st} realization from the simulation(red line) and from dislocation structures through Lin-Thomson shielding solution (green line) along the load increment.

dynamic effects during dislocation development, the overall toughening from the dislocation shielding still follows the R-curve from the DD simulation. Specifically the crack toughening corresponds to the instantaneous shielding of the overall dislocation structure.

In the Lin-Thomson solution, Eq. 5.5b, $F = (K_I^\infty - K_0)/\mu b$ is a sum over the shielding contributions from each dislocation. We found that μb and K_0 can be combined as $\mu b K_0^3$ to collapse the trends of F, i.e. the overall shielding, in materials A-E. F versus $\mu b K_0^3$ is plotted in Fig. 5.14 where 5.14(a), 5.14(b) and 5.14(c) are yield stress σ_Y of 500, 600 and 700 MPa, respectively. Here the fourth realization is ignored since this randomness provides very low fracture toughness in all cases. Overall fracture toughness increases with increasing $\mu b K_0^3$ at any yield stress, although it is not explicit in materials B and D due to their near-brittle behavior. Comparing materials A and B (both material properties are similar except the lower Young's modulus in material B), μb and K_0 are decreased with decreasing Young's modulus.

In fact dislocations are able to induce the crack separation more easily for the lower K_0. Also lower dislocation activity is a consequence of the lower μb. From above reasons, the fracture toughness in material B is much lower than in material A.

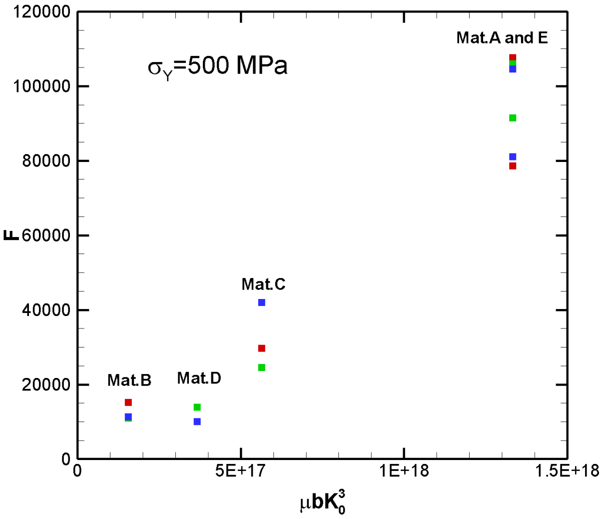

(a)

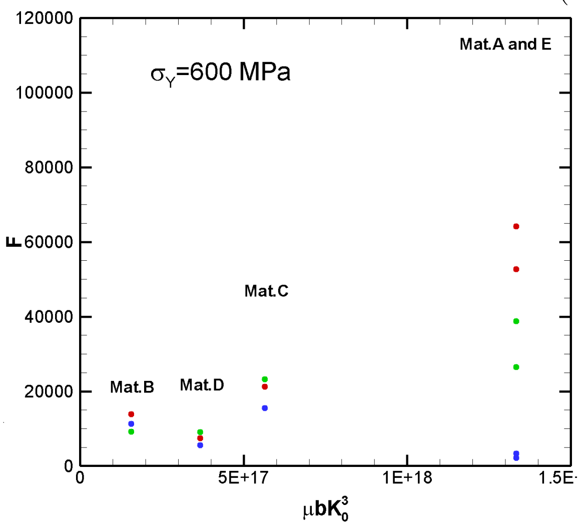

(b)

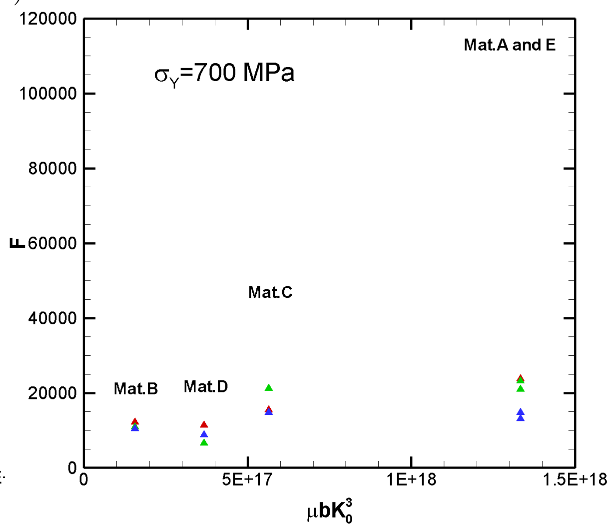

(c)

Figure 5.14: A sum over all the positional dependence of the dislocation shielding F versus $\mu b K_0^3$ for material A-E with various yield σ_Y using three statistically different realizations of sources and obstacles in the simulation (a) σ_Y=500 MPa (b) σ_Y=600 MPa (c) σ_Y=700 MPa.

5.3 Summary

We have implemented symmetric boundaries for a short crack problem to reduce the computational time and storage in 2d-DD. In addition the stability, accuracy and robustness of the 2d-DD methodology for fracture can be improved significantly by the new algorithm of Chakravarthy and Curtin (2011a). Our improvement and results is listed in the following:

- Use of the new superposition scheme (O'Day and Curtin (2004)) avoids the time expense in the polarization stress calculation and correctly captures the dislocation interactions with cohesive zone that stabilizes the problem with large cohesive strength.

- To improve material model with realistic yield stress and realistic cohesive strength, the obstacle-controlled yield model is utilized and adaptive meshing is employed to retain the required fine mesh resolution near the crack tip for large cohesive strength while the crack is growing.

- For a short cracked particle in the high yield stress matrix under monotonic loading, the fracture behavior is nearly brittle.

- For long crack problems with such high strength material, we show that a change of μb and K_0 parameters has a huge effect on fracture toughness through the shielding quantity $F = (K_{IC} - K_0)/\mu b$ and the toughness can be characterized in terms of $\mu b K_0^3$.

- Results from the simulations confirm that the dislocation shielding of cohesive crack with the asymptotic interpolation solution (Bhandakkar et al. (2010)) is comparable to the sharp crack solution (Lin and Thomson (1986)) if the cohesive strength is very high as used in our case; σ_{coh}=5 GPa.

Chapter 6

Conclusions and Outlook

Fracture processes are composed of the underlying physical mechanisms of irreversible deformation i.e. plastic dissipation and material separation taking place by breaking of atomic bonds. The region around the crack tip is a micron-scale volume where continuum plasticity cannot predict crack growth properly. The prediction of fracture toughness requires material length scales, and there is a large body of experimental evidence that plastic flow processes in crystalline solids are inherently size-dependent over a scale that ranges from a micrometer to 100 μm. Many approaches to size-dependent plasticity, such as strain-gradient plasticity and the discrete dislocation plasticity, have been developed to tackle this problem. In discrete dislocation plasticity, the dislocations are treated as line singularities in an elastic body. A many body interaction problem involving the discrete dislocations need to be solved with the boundary value problem. The crack surface is described by a cohesive zone law, so that crack growth is an outcome of the boundary value problem. This thesis has focused on modifications and extensions to the two dimensional discrete dislocation method (2d-DD) of Van der Giessen and Needleman (1995) for fatigue and fracture problems.

Crack growth from small initially-cracked elastic particles into a ductile metal material has been analyzed in Chapter 3 to characterize the inelastic deformation in the matrix at micron scales. Under fatigue loading, the presence of a cracked particle reveals that the particle reduces ΔK^{th} (the threshold value of ΔK) and the Paris power-law exponent, relative to a single crystal material. Also slip blocking at the particle−matrix interface gives rise to a dislocation structure with increased anti-shielding relative to the single crystal material. Stress concentrations due to elastic mismatch increase the local stress intensity factor and thus reduce the applied stress intensity factor at which crack growth is observed. The elastic stress concentrations decay with increasing crack length, leading to halting of crack growth near and above the threshold value of ΔK after some critical distance of crack growth.

In Chapter 4, fracture in HCP-like single crystals, such as Zinc in this study, using a modified 2d-DD model with a Peierls stress approach to control the plastic anisotropy associated with basal and pyramidal slip. From the results, we find that fracture toughness is mostly independent of plastic anisotropy. The toughening was found to depend on the crystallographic direction in which the crack is made to grow. Basal slip occurs extensively around the crack tip and is necessary in certain regions to help generate the necessary sector-like solutions expected in a single crystal, but the basal dislocations in these regions do not provide significant crack shielding. Application of the Stress Gradient Plasticity concept shows that the equilibrium dislocation dipole spacing serves as an internal material length scale for controlling fracture toughness. Furthermore, the fracture toughness of materials with Peierls stress and no obstacles and of materials with obstacles and zero Peierls stress can be unified through the Stress Gradient Plasticity concept, demonstrating the general feature that internal material length scales can control fracture. Microcrack nucleation along basal planes parallel to the main crack may be a result of tensile stress concentration that exist along the 60° line emanating from the crack tip, due to the discreteness of the dislocation plasticity and incomplete cancellation of dislocation stress fields in structures that are attempting to generate the constant stress sectors expected from continuum-level analysis.

The implementation of symmetric boundaries to reduce computational cost for short crack simulations is described in Chapter 5. The improvement to the material model with realistic yield stress and realistic cohesive strength is achieved by the new algorithms of Chakravarthy and Curtin (2011a). Unfortunately, the particles in "strong" Aluminum did not lead to any result since the fracture behavior is like a brittle material under monotonic loading. For long crack problems with such high yield stress material, a change of μb and K_0 has a huge effect on fracture toughness through a sum over all positional dependence $F = (K_{IC} - K_0)/\mu b$ of dislocation shielding.

In this 2d-DD, there is a variety of idealizations in the simulations of fracture/fatigue crack growth that need to be relaxed to obtain quantitatively useful predictions, for example;

- For numerical reasons, the analyses are carried out for pure Mode-I loading with symmetry assumed about the crack plane, while in single crystals mixed mode loading conditions generally prevail at the crack tip.

- The analyses have been two dimensional, with both three-dimensional dislocation effects and three-dimensional crack growth effects neglected

- The effects of crack tip blunting are not taken into account in this small strain analysis.

- The calculations have been carried out for small amounts of straight ahead crack growth in a single crystal, whereas experimental data typically are for larger amounts of crack growth in polycrystalline materials as a result in the microstructural aspects involved in crack transmission across a grain boundary Catoor (2008).

Fatigue crack growth rates are sensitive to the environment and accounting for environmental effects means accounting for chemistry in the crack tip region. This in turn requires an atomistic rather than a phenomenological cohesive model of the creation of new free surface. Also, most of the limitations mentioned in the previous paragraph have the effect of giving rise to values of ΔK^{th} that are relatively low and the Paris law exponents values rather high. For increased values of crack growth resistance the region over which significant plastic dissipation occurs increases, Curtin et al. (2010). Moreover 2d-DD simulations of fatigue crack growth require large amounts of computer time to enable calculations of larger amounts of crack growth. Generally many important length scales involve for fracture range from that of the macroscale object to the atomic scale so that a multiscale modeling framework is needed for a predictive theory. Recently the success tool for the multiscale modeling with directly coupling the interface between different length scales is the coupled atomistic and continuum modeling (e.g. Shilkrot et al. (2002), Xiao and Belytschko (2004), Warner et al. (2007)). Using the multiscale modeling is a new direction for innovative research and can explore some of the above issues in fracture/fatigue mechanics.

Appendix A

Multipoint Constraint Method

In this appendix, the multipoint constraints (MPCs) method for finite element equations is presented, Liu and Quek (2003). The method is used to obtain artificial elements to establish the relationship between the degree-of-freedoms (DOFs) at the boundary nodes. The boundary condition for the multiple cracks in an infinite space as shown in Fig. 5.1(a) is represented by the equivalent constraints in Fig. 5.1(b).

Recall that the global system equation for the finite element system with a DOFs of n can be written in the following matrix form:

$$[\mathbf{K}]\{\mathbf{u}\} = \{\mathbf{F}\} \tag{A.1}$$

where $[\mathbf{K}]$ is the stiffness matrix of $n \times n$, $\{\mathbf{u}\}$ is the displacement vector of $n \times 1$, and $\{\mathbf{F}\}$ is the external force vector of $n \times 1$. If the system is constrained by m MPC equations, these equations are written in the following general matrix form:

$$[\mathbf{C}]_{\mathrm{m}}\{\mathbf{u}\}_{\mathrm{m}} = \{\mathbf{Q}\}_{\mathrm{m}} \tag{A.2}$$

where $[\mathbf{C}]_{\mathrm{m}}$ is a local constant matrix of $m \times n$ $(m < n)$, $\{\mathbf{u}\}_{\mathrm{m}}$ is the local displacement vector of $m \times 1$ and $\{\mathbf{Q}\}_{\mathrm{m}}$ is a local constant vector of $m \times 1$.

For the specification to our case of constraint in this thesis, the nodes on the right surface is constrained to remain straight. Therefore the set of constrained equation are written as

$$u_1 = u_2, \quad u_2 = u_3, \quad u_3 = u_4, \quad \ldots. \quad u_{m-1} = u_m \tag{A.3}$$

The set of constraint equations can be written in the matix form as following:

$$\underbrace{\begin{pmatrix} 1 & -1 & 0 & \ldots & 0 \\ 0 & 1 & -1 & \ldots & 0 \\ 0 & 0 & 1 & \ldots & 0 \\ \vdots & \vdots & \vdots & \ddots & \vdots \\ 0 & 0 & 0 & 1 & -1 \end{pmatrix}}_{[\mathbf{C}]_\mathrm{m}} \underbrace{\begin{Bmatrix} u_1 \\ u_2 \\ u_3 \\ \vdots \\ u_m \end{Bmatrix}}_{\{\mathbf{u}\}_\mathrm{m}} = \underbrace{\begin{Bmatrix} 0 \\ 0 \\ 0 \\ \vdots \\ 0 \end{Bmatrix}}_{\{\mathbf{Q}\}_\mathrm{m}} \tag{A.4}$$

The constraint equations above correspond to our constraint where the right surface is enforced to move in x-direction identically, as shown in Fig. A.1

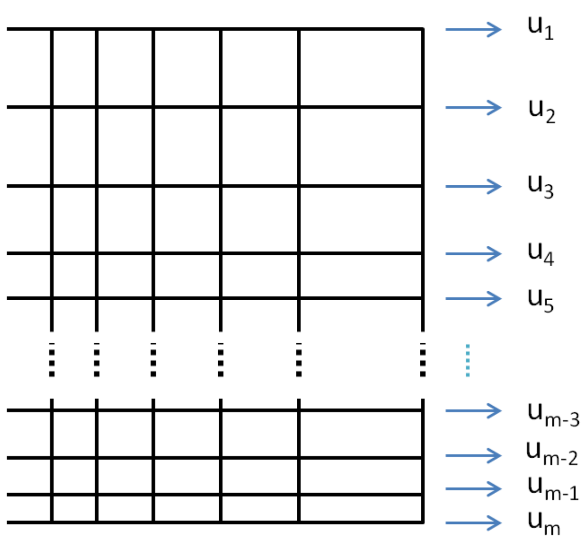

Figure A.1: Illustration for the specific constraint at the right surface enforced in x-direction to remain straight.

The conventional approach to implement the multipoint constraints (MPCs) is often obtained by two methods which are "Lagrange Multiplier" and "Penalty Method".

The advantage of Penalty method is no requirement for extra variable to solve and thus the size of the matrix remains the same. However the constraint equations can only be satisfied *approximately*, and the right choice of can be a problem for some cases. The Penalty method is easily implemented by adding the constraint equations directly to the global stiffness matrix. In this method, the constraint equations, Eq. A.2 is written as

$$\{\mathbf{v}\} = [\mathbf{C}]\{\mathbf{u}\} - \{\mathbf{Q}\} \tag{A.5}$$

where $[\mathbf{C}]$ is a global constant matrix of $m \times n$ $(m < n)$, $\{\mathbf{u}\}$ is the global displacement vector of $m \times 1$ and $\{\mathbf{Q}\}$ is a global constant vector of $m \times 1$ such that $\{\mathbf{v}\} = 0$ implies full satisfaction of the global constraints. The potential energy function can then be modified as

$$\Pi = \frac{1}{2}\{\mathbf{u}\}^{\mathrm{T}}[\mathbf{K}]\{\mathbf{u}\} - \{\mathbf{u}\}^{\mathrm{T}}\{\mathbf{F}\} + \frac{1}{2}\{\mathbf{v}\}^{\mathrm{T}}\alpha\{\mathbf{v}\} \tag{A.6}$$

where $\frac{1}{2}\{\mathbf{v}\}^{\mathrm{T}}\alpha\{\mathbf{v}\}$ is a diagonal matrix of penalty parameter that are constants chosen by $\alpha = 1 \times 10^{5-8} \times$Young's modulus. The stationary condition of the modified potential function requires the derivatives of Π with respect to the $\{\mathbf{u}\}$ to vanish, which yields

$$\left[[\mathbf{K}] + [\mathbf{C}]^{T}\alpha[\mathbf{C}]\right]\{\mathbf{u}\} = \{\mathbf{F}\} + [\mathbf{C}]^{\mathrm{T}}\alpha\{\mathbf{Q}\} \tag{A.7}$$

where $[\mathbf{C}]^{T}\alpha[\mathbf{C}]$ is called a *global penalty matrix.* The efficiency of solving the system Eq. A.7 is almost the same as that of solving Eq. A.1. In our specific case which is $\{\mathbf{F}\} + [\mathbf{C}]^{\mathrm{T}}\alpha\{\mathbf{Q}\} = \{\mathbf{0}\}$, the *local penalty matrix* can be written as

$$[\mathbf{C}]_{\mathrm{m}}^{T}\alpha[\mathbf{C}]_{\mathrm{m}} = \begin{pmatrix} 2\alpha & -\alpha & 0 & \dots & 0 \\ -\alpha & 2\alpha & -\alpha & \dots & 0 \\ 0 & -\alpha & 2\alpha & \dots & 0 \\ \vdots & \vdots & \vdots & \ddots & \vdots \\ 0 & 0 & 0 & -\alpha & 2\alpha \end{pmatrix} \tag{A.8}$$

From the local matrix system, we can easily convert the local components to the global components by replacing to the position of equation number.

Bibliography

E. C. Aifantis. The physics of plastic deformation. *International Journal of Plasticity*, 3(3):211–247, 1987.

J. E. Allison, J. W. Jones, A. Needleman, S. R. Nuti, S. Suresh, and V. Tvergaard. *Fundamentals of metal matrix composites*. 1993.

S. Aubry, K. Kang, S. Ryu, and W. Cai. Energy barrier for homogeneous dislocation nucleation: Comparing atomistic and continuum models. *Scripta Materialia*, 64 (11):1043 – 1046, 2011.

D. S. Balint, V. S. Deshpande, A. Needleman, and E. Van der Giessen. A discrete dislocation plasticity analysis of grain-size strengthening. *Materials Science and Engineering: A*, 400-401(0):186 – 190, 2005.

D. S. Balint, V. S. Deshpande, A. Needleman, and E. Van der Giessen. Discrete dislocation plasticity analysis of the grain size dependence of the flow strength of polycrystals. *International Journal of Plasticity*, 24(12):2149 – 2172, 2008.

A. J. Beaudoin, P. R. Dawson, K. K. Mathur, and U. F. Kocks. A hybrid finite element formulation for polycrystal plasticity with consideration of macrostructural and microstructural linking. *International Journal of Plasticity*, 11(5):501–521, 1995.

T. K. Bhandakkar, A. C. Chng, W. A. Curtin, and H. Gao. Dislocation shielding of a cohesive crack. *Journal of the Mechanics and Physics of Solids*, 58(4):530–541, 2010.

E. Bittencourt, A. Needleman, M. E. Gurtin, and E. Van der Giessen. A comparison of nonlocal continuum and discrete dislocation plasticity predictions. *Journal of the Mechanics and Physics of Solids*, 51(2):281 – 310, 2003.

R. C. Blish. *Dislocation Velocity and Slip on the* $\{\bar{1}2\bar{1}2\}$ $\langle 1\bar{2}13\rangle$ *System of Zinc*. PhD thesis, California Institute of Technology, USA, 1967.

J. R. Brockenbrough, A. J. Hinkle, P. E. Magnusen, and R. J. Bucci. Microstructurally based model of fatigue initiation and growth. Technical report, DTIC Document, 1994.

M. S. Bruzzi and P. E. McHugh. Micromechanical investigation of the fatigue crack growth behaviour of Al-SiC MMCs. *International Journal of Fatigue*, 26(8):795 – 804, 2004.

M. S. Bruzzi, P. E. McHugh, F. O'Rourke, and T. Linder. icromechanical modelling of the static and cyclic loading of an Al 2124-SiC MMC. *International Journal of Plasticity*, 17(4):565 – 599, 2001.

M. J. Buehler, F. F. Abraham, and H. Gao. Hyperelasticity governs dynamic fracture at a critical length scale. *Nature*, 426(6963):141–146, 2003.

D. Caillard. Kinetics of dislocations in pure Fe. part I. in-situ straining experiments at room temperature. *Acta Materialia*, 58(9):3493 – 3503, 2010.

G. T. Camacho and M. Ortiz. Computational modelling of impact damage in brittle materials. *International Journal of solids and structures*, 33(20):2899–2938, 1996.

P. Castany, F. Pettinari-Sturmel, J. Crestou, J. Douin, and A. Coujou. Experimental study of dislocation mobility in a Ti-6Al-4V alloy. *Acta Materialia*, 55(18):6284 – 6291, 2007.

D. Catoor. Fracture in single and bicrystals of zinc: Experiments and computational modeling. 2008.

D. Catoor and K. S. Kumar. Crack growth on the basal plane in single crystal zinc: experiments and computations. *Philosophical Magazine*, 88(10):1437–1460, 2008.

S. S. Chakravarthy and W. A. Curtin. Effect of source and obstacle strengths on yield stress: A discrete dislocation study. *Journal of the Mechanics and Physics of Solids*, 58(5):625 – 635, 2010a.

S. S. Chakravarthy and W. A. Curtin. Origin of plasticity length-scale effects in fracture. *Physical Review Letters*, 105(11):115502, Sep 2010b.

S. S. Chakravarthy and W. A. Curtin. New algorithms for discrete dislocation modeling of fracture. *Modelling and Simulation in Materials Science and Engineering*, 19(4):045009, 2011a.

S. S. Chakravarthy and W. A. Curtin. Stress-gradient plasticity. *Proceedings of the National Academy of Sciences of the United States of America*, 108(38):15716–15720, 2011b.

N. Chawla, C. Andres, J. W. Jones, and J. E. Allison. Cyclic stress-strain behavior of particle reinforced metal matrix composites. *Scripta materialia*, 38(10), 1998a.

N. Chawla, J. W. Jones, C. Andres, and J. E. Allison. Effect of SiC volume fraction and particle size on the fatigue resistance of a 2080 Al/SiCp composite. *Metallurgical and Materials Transactions A*, 29(11):2843–2854, 1998b.

D. Chen. Stress intensity factor for a crack normal to an interface between two orthotropic materials. *International Journal of Fracture*, 88:19–39, 1997. ISSN 0376-9429.

Q. Chen, V. S. Deshpande, E. Van der Giessen, and A. Needleman. Friction stress effects on mode I crack growth predictions. *Scripta Materialia*, 48(6):755 – 759, 2003.

Z. Z. Chen, K. Tokaji, and A. Minagi. Particle size dependence of fatigue crack propagation in SiC particulate-reinforced aluminium alloy composites. *Journal of Materials Science*, 36:4893–4902, 2001. ISSN 0022-2461.

A. C. Chng, M. P. ODay, W. A. Curtin, A. A. O. Tay, and K. M. Lim. Fracture in confined thin films: a discrete dislocation study. *Acta materialia*, 54(4):1017–1027, 2006.

H. H. M. Cleveringa, E. Van der Giessen, and A. Needleman. Comparison of discrete dislocation and continuum plasticity predictions for a composite material. *Acta Materialia*, 45(8):3163 – 3179, 1997.

H. H. M. Cleveringa, E. Van der Giessen, and A. Needleman. Discrete dislocation simulations and size dependent hardening in single slip. *Le Journal de Physique IV*, 8(PR4), 1998.

H. H. M. Cleveringa, E. Van der Giessen, and A. Needleman. A discrete dislocation analysis of bending. *International Journal of Plasticity*, 15(8):837 – 868, 1999.

H. H. M. Cleveringa, E. Van der Giessen, and A. Needleman. A discrete dislocation analysis of mode I crack growth. *Journal of the Mechanics and Physics of Solids*, 48(6-7):1133 – 1157, 2000.

H. H. M. Cleveringa, E. Van der Giessen, and A. Needleman. A discrete dislocation analysis of rate effects on mode i crack growth. *Materials Science and Engineering: A*, 317(1 - 2):37 – 43, 2001.

W. C. Crone and T. W. Shield. Experimental study of the deformation near a notch tip in copper and copper-beryllium single crystals. *Journal of the Mechanics and Physics of Solids*, 49(12):2819–2838, 2001.

W. A. Curtin, V. S. Deshpande, A. Needleman, E. Van der Giessen, and M. Wallin.

Hybrid discrete dislocation models for fatigue crack growth. *International Journal of Fatigue*, 32(9):1511–1520, 2010.

R. De Borst and H. B. Mühlhaus. Gradient-dependent plasticity: Formulation and algorithmic aspects. *International Journal for Numerical Methods in Engineering*, 35(3):521–539, 1992.

A. Deruyttere and G. B. Greenough. The criterion for the cleavage fracture of zinc single crystals. *Journal of the Institute of Metals*, 84:337–345, 1956.

V. S. Deshpande, A. Needleman, and E. Van der Giessen. Dislocation dynamics is chaotic. *Scripta Materialia*, 45(9):1047 – 1053, 2001a.

V. S. Deshpande, A. Needleman, and E. Van der Giessen. A discrete dislocation analysis of near-threshold fatigue crack growth. *Acta Materialia*, 49(16):3189 – 3203, 2001b.

V. S. Deshpande, A. Needleman, and E. Van der Giessen. Discrete dislocation modeling of fatigue crack propagation. *Acta Materialia*, 50(4):831 – 846, 2002.

V. S. Deshpande, A. Needleman, and E. Van der Giessen. Discrete dislocation plasticity modeling of short cracks in single crystals. *Acta Materialia*, 51(1):1 – 15, 2003a.

V. S. Deshpande, A. Needleman, and E. Van der Giessen. Scaling of discrete dislocation predictions for near-threshold fatigue crack growth. *Acta Materialia*, 51(15): 4637 – 4651, 2003b.

B. Devincre and L. P. Kubin. Mesoscopic simulations of dislocations and plasticity. *Materials Science and Engineering: A*, 234-236(0):8 – 14, 1997.

T. Do, N. S. McIntyre, P. A. W. Van der Heide, and U. G. Akano. Oxidation kinetics of Mg-, Si-, and Fe-implanted aluminum by using x-ray photoelectron spectroscopy. *The Journal of Physical Chemistry B*, 103(13):2402–2407, 1999.

W. J. Drugan. Asymptotic solutions for tensile crack tip fields without kink-type shear bands in elastic-ideally plastic single crystals. *Journal of the Mechanics and Physics of Solids*, 49(9):2155 – 2176, 2001.

J. D. Eshelby. Elastic inclusions and inhomogeneities. *Progress in solid mechanics*, 2 (1):89–140, 1961.

J. Fan, D. L. McDowell, M. F. Horstemeyer, and K. Gall. Computational micromechanics analysis of cyclic crack-tip behavior for microstructurally small cracks in dual-phase Al-Si alloys. *Engineering Fracture Mechanics*, 68(15):1687–1706, 2001.

M. C. Fivel, T. J. Gosling, and G. R. Canova. Implementing image stresses in a 3D dislocation simulation. *Modelling and Simulation in Materials Science and Engineering*, 4:581, 1996.

N. A. Fleck, G. M. Muller, M. F. Ashby, and J. W. Hutchinson. Strain gradient plasticity: theory and experiment. *Acta Metallurgica et Materialia*, 42(2):475–487, 1994.

L. B. Freund. The mechanics of dislocations in strained-layer semiconductor materials. In J. W. Hutchinson and T. Y. Wu, editors, *Advances in Applied Mechanics*, volume 30 of *Advances in Applied Mechanics*, pages 1 – 66. Elsevier, 1993.

K. Gall, M. F. Horstemeyer, B. W. Degner, D. L. McDowell, and J. Fan. On the driving force for fatigue crack formation from inclusions and voids in a cast a356 aluminum alloy. *International Journal of Fracture*, 108:207–233, 2001.

V. V. Ganesh and N. Chawla. Effect of particle orientation anisotropy on the tensile behavior of metal matrix composites: experiments and microstructure-based simulation. *Materials Science and Engineering: A*, 391(1):342–353, 2005.

J. J. Gilman. Creation of cleavage steps by dislocation. *Transactions of the Metallurgical Society of AIME*, 212:310–315, 1958.

J. N. Hall, J. W. Jones, and A. K. Sachdev. Particle size, volume fraction and matrix strength effects on fatigue behavior and particle fracture in 2124 aluminum-SiCp composites. *Materials Science and Engineering: A*, 183(1-2):69–80, 1994.

A. Hartmaier, M. C. Fivel, G. R. Canova, and P. Gumbsch. 3d discrete dislocation models of thin-film plasticity. *Proceedings material Research Society Symp.(Boston, MA, USA)*, 505(0):539 – 544, 1997.

J. W. He, N. Li, M. Jia, S. P. Wen, and P. R. Jia. Effect of interface layer on fatigue crack growth in an aluminium laminate. *Fatigue and Fracture of Engineering Materials and Structures*, 27(3):171–176, 2004.

P. B. Hirsch, S. G. Roberts, and J. F. Nye. Modelling plastic zones and the brittle-ductile transition and discussion. *Philosophical Transactions: Mathematical, Physical and Engineering Sciences*, 355(1731):pp. 1991–2002, 1997.

D. Hull and D. J. Bacon. *Introduction to dislocations*, volume 37. Butterworth-Heinemann, 2011.

F. Jiang, Z. L. Deng, K. Zhao, and J. Sun. Fatigue crack propagation normal to a plasticity mismatched bimaterial interface. *Materials Science and Engineering: A*, 356(1 - 2):258 – 266, 2003.

H. A. Khater and D. J. Bacon. Dislocation core structure and dynamics in two atomic models of $\alpha-$zirconium. *Acta Materialia*, 58(8):2978 – 2987, 2010.

A. S. Kim, S. Suresh, and C. F. Shih. Plasticity effects on fracture normal to interfaces with homogeneous and graded compositions. *International Journal of Solids and Structures*, 34(26):3415 – 3432, 1997.

T. Kruml, E. Conforto, B. L. Piccolo, D. Caillard, and J. L. Martin. From dislocation cores to strength and work-hardening: a study of binary Ni3Al. *Acta Materialia*, 50(20):5091 – 5101, 2002.

L. P. Kubin, G. Canova, M. Condat, B. Devincre, V. Pontikis, and Y. Bréchet. Dislocation microstructures and plastic flow: A 3D simulation. *Solid-State Phys.*, 23&24:455–472, 1992.

L. P. Kubin, B. Devincre, and M. Tang. Mesoscopic modelling and simulation of plasticity in fcc and bcc crystals: Dislocation intersections and mobility. *Journal of Computer-Aided Materials Design*, 5:31–54, 1998.

G. P. Leyson, W. A. Curtin, L. G. Hector, and C. F. Woodward. Quantitative prediction of solute strengthening in aluminium alloys. *Nature Materials*, 9(9): 750–755, Sept. 2010.

I. Lin and R. Thomson. Cleavage, dislocation emission, and shielding for cracks under general loading. *Acta Metallurgica*, 34(2):187 – 206, 1986.

G. R. Liu and S. S. Quek. *The finite element method: a practical course*. Butterworth-Heinemann, 2003.

D. J. Lloyd. Particle reinforced aluminium and magnesium matrix composites. *International Materials Reviews*, 39(1):1–23, 1994.

Q. Ma and D. R. Clarke. Size dependent hardness of silver single crystals. *Journal of Materials Research*, 10(04):853–863, 1995.

I. Mastorakos and H. Zbib. Shielding and amplification of a penny-shape crack due to the presence of dislocations. *International Journal of Fracture*, 142:103–117, 2006.

D. L. McDowell, K. Gall, M. F. Horstemeyer, and J. Fan. Microstructure-based fatigue modeling of cast Al356-T6 alloy. *Engineering Fracture Mechanics*, 70(1):49 – 80, 2003.

M. T. Milan and P. Bowen. Experimental and predicted fatigue crack growth resistance in Al 2124/Al 2124+35%SiC(3 microns) bimaterial. *International Journal of Fatigue*, 25(7):649 – 659, 2003.

M. T. Milan and P. Bowen. Fatigue crack growth resistance of sic p reinforced Al alloys: Effects of particle size, particle volume fraction, and matrix strength. *Journal of materials engineering and performance*, 13(5):612–618, 2004.

F. R. N. Nabarro. Dislocations in a simple cubic lattice. *Proceedings of the Physical Society*, 59(2):256, 1947.

N. Narasaiah and K. K. Ray. Study of short crack growth behaviour in single and multiphase steels using rotating bending machine. *International Journal of Fatigue*, 28(8):891 – 900, 2006.

A. Needleman. A continuum model for void nucleation by inclusion debonding. *Journal of Applied Mechanics*, 54(3):525–531, 1987.

L. Nicola, E. Van der Giessen, and A. Needleman. Size effects in polycrystalline thin films analyzed by discrete dislocation plasticity. *Thin Solid Films*, 479(1-2):329 – 338, 2005.

L. Nicola, Y. Xiang, J. J. Vlassak, E. Van der Giessen, and A. Needleman. Plastic deformation of freestanding thin films: Experiments and modeling. *Journal of the Mechanics and Physics of Solids*, 54(10):2089 – 2110, 2006.

T. Nogaret, W. A. Curtin, J. A. Yasi, L. G. Hector Jr, and D. R. Trinkle. Atomistic study of edge and screw $\langle c + a \rangle$ dislocations in magnesium. *Acta Materialia*, 58 (13):4332 – 4343, 2010.

M. P. O'Day. *A New Super Position Framework for Discrete Dislocation Plasticity: Methodology and Application to Inhomogeneous Boundary Value Problem.* PhD thesis, Brown University, USA, 2005.

M. P. O'Day and W. A. Curtin. A superposition framework for discrete dislocation plasticity. *Journal of applied mechanics*, 71:805, 2004.

M. P. O'Day and W. A. Curtin. Bimaterial interface fracture: A discrete dislocation model. *Journal of the Mechanics and Physics of Solids*, 53(2):359 – 382, 2005.

M. P. O'Day, P. Nath, and W. A. Curtin. Thin film delamination: A discrete dislocation analysis. *Journal of the Mechanics and Physics of Solids*, 54(10):2214 – 2234, 2006.

P. C. Paris, M. Gomez, and W. E. Anderson. A rational analytic theory of fatigue. *The Trend in Engineering*, 13(1):9 – 14, 1961.

R. Parisot, S. Forest, A. Pineau, F. Grillon, X. Demonet, and J.-M. Mataigne. Deformation and damage mechanisms of zinc coatings on hot-dip galvanized steel sheets: Part II. damage modes. *Metallurgical and Materials Transactions A*, 35:813–823, 2004. ISSN 1073-5623.

P. Paufler. Crystal research and technology. *(Ecole d't d'Yravals, 314 September 1979), publie sous la direction de: P. Groh, L. P. Kubin et J.-L. Martin. Dislocations et deformation plastique. Les ditions de physique, les ulis 1980, 462 p. Preis: FF 100.00*, 18(2):178–178, 1983.

R. Pippan and F. O. Riemelmoser. Fatigue of bimaterials. investigation of the plastic mismatch in case of cracks perpendicular to the interface. *Computational Materials Science*, 13(1):108–116, 1998.

R. Pippan and P. Weinert. The effective threshold of fatigue crack propagation in aluminium alloys. II. the influence of particle reinforcement. *Philosophical Magazine A*, 77(4):875–886, 1998.

R. Pippan, K. Flechsig, and F. O. Riemelmoser. Fatigue crack propagation behavior in the vicinity of an interface between materials with different yield stresses. *Materials Science and Engineering: A*, 283(1 - 2):225 – 233, 2000.

D. P. Pope. *The Mobility of Edge Dislocations in the Basal slip System of Zinc*. PhD thesis, California Institute of Technology, USA, 1967.

J. E. Raynolds, J. R. Smith, G. L. Zhao, and D. J. Srolovitz. Adhesion in NiAl-Cr from first principles. *Physical Review B*, 53(20):13883, 1996.

J. R. Rice. Tensile crack tip fields in elastic-ideally plastic crystals. *Mechanics of Materials*, 6(4):317 – 335, 1987a.

J. R. Rice. Tensile crack tip fields in elastic-ideally plastic crystals. *Mechanics of Materials*, 6(4):317–335, 1987b.

F. O. Riemelmoser, R. Pippan, and O. Kolednik. Cyclic crack growth in elastic plastic solids: a description in terms of dislocation theory. *Computational Mechanics*, 20: 139–144, 1997.

F. O. Riemelmoser, P. Gumbsch, and R. Pippan. Dislocation modelling of fatigue cracks: An overview. *Material Transactions*, 42(1):2–13, 2001.

A. Romeo and R. Ballarini. A cohesive zone model for cracks terminating at a bimaterial interface. *International Journal of Solids and Structures*, 34(11):1307 – 1326, 1997.

J. H. Rose, J. Ferrante, and J. R. Smith. Universal Binding Energy Curves for Metals and Bimetallic Interfaces. *Physical Review Letters*, 47(9):675–678, Aug. 1981.

M. Shell De Guzman, G. Neubauer, P. Flinn, and W. D. Nix. The role of indentation depth on the measured hardness of materials. In *MRS Proceedings*, volume 308. Cambridge Univ Press, 1993.

T. W. Shield and K. S. Kim. Experimental measurement of the near tip strain field in an iron-silicon single crystal. *Journal of the Mechanics and Physics of Solids*, 42 (5):845–873, 1994.

L. E. Shilkrot, R. E. Miller, and W. A. Curtin. Coupled atomistic and discrete dislocation plasticity. *Physical review letters*, 89(2):25501, 2002.

C. S. Shin, M. C. Fivel, M. Verdier, and C. Robertson. Dislocation dynamics simulations of fatigue of precipitation-hardened materials. *Materials Science and Engineering: A*, 400 - 401(0):166 – 169, 2005.

S. S. Shishvan, S. Mohammadi, M. Rahimian, and E. Van der Giessen. Plane-strain discrete dislocation plasticity incorporating anisotropic elasticity. *International Journal of Solids and Structures*, 48(2):374–387, 2011.

T. Siegmund, N. A. Fleck, and A. Needleman. Dynamic crack growth across an interface. *International Journal of Fracture*, 85:381–402, 1997.

J. Spence and C. Koch. Experimental evidence for dislocation core structures in silicon. *Scripta Materialia*, 45(11):1273 – 1278, 2001.

E. J. Stofel. *Plastic Flow and Fracture of Zinc Single Crystals*. PhD thesis, California Institute of Technology, USA, 1962.

Y. Sugimura, P. G. Lim, C. F. Shih, and S. Suresh. Fracture normal to a bimaterial interface: Effects of plasticity on crack-tip shielding and amplification. *Acta Metallurgica et Materialia*, 43(3):1157 – 1169, 1995.

S. Suresh. *Fatigue of Materials*. Cambridge solid state science series. Cambridge University Press, 1998.

S. Suresh, Y. Sugimura, and E. K. Tschegg. The growth of a fatigue crack approaching a perpendicularly-oriented, bimaterial interface. *Scripta Metallurgica et Materialia*, 27(9):1189 – 1194, 1992.

H. Tada, P. C. Paris, and G. R. Irwin. *The Stress Analysis of Cracks Handbook, Third Edition*. ASME Press, New York, NY, 3 edition, 2000.

K. Tanaka, Y. Akiniwa, K. Shimizu, H. Kimura, and S. Adachi. Fatigue thresholds of discontinuously reinforced aluminum alloy correlated to tensile strength. *International Journal of Fatigue*, 22(5):431 – 439, 2000.

K. Tapasa, Y. N. Osetsky, and D. J. Bacon. Computer simulation of interaction of an edge dislocation with a carbon interstitial in α-iron and effects on glide. *Acta Materialia*, 55(1):93 – 104, 2007.

V. Tvergaard. Resistance curves for mixed mode interface crack growth between dissimilar elastic-plastic solids. *Journal of the Mechanics and Physics of Solids*, 49 (11):2689 – 2703, 2001.

V. Tvergaard and G. Herrmann. Modeling of defects and fracture mechanics, 1993.

V. Tvergaard and J. W. Hutchinson. The relation between crack growth resistance and fracture process parameters in elastic-plastic solids. *Journal of the Mechanics and Physics of Solids*, 40(6):1377–1397, 1992.

V. Tvergaard and J. W. Hutchinson. The influence of plasticity on mixed mode interface toughness. *Journal of the Mechanics and Physics of Solids*, 41(6):1119 – 1135, 1993.

E. Van der Giessen and A. Needleman. Discrete dislocation plasticity: a simple planar model. *Modelling and Simulation in Materials Science and Engineering*, 3(5):689, 1995.

E. Van der Giessen, V. S. Deshpande, H. H. M. Cleveringa, and A. Needleman. Discrete dislocation plasticity and crack tip fields in single crystals. *Journal of the Mechanics and Physics of Solids*, 49(9):2133 – 2153, 2001.

B. Wang and T. Siegmund. Simulation of fatigue crack growth at plastically mismatched bi-material interfaces. *International Journal of Plasticity*, 22(9):1586 – 1609, 2006.

Y. Wang, D. J. Srolovitz, J. M. Rickman, and R. LeSar. Dislocation motion in the presence of diffusing solutes: a computer simulation study. *Acta Materialia*, 48(9): 2163 – 2175, 2000.

D. Wappling, J. Gunnars, and P. Sthle. Crack growth across a strength mismatched bimaterial interface. *International Journal of Fracture*, 89:223–243, 1998.

D. H. Warner, W. A. Curtin, and S. Qu. Rate dependence of crack-tip processes predicts twinning trends in fcc metals. *Nature materials*, 6(11):876–881, 2007.

Y. Wei and J. W. Hutchinson. Steady-state crack growth and work of fracture for solids characterized by strain gradient plasticity. *Journal of the Mechanics and Physics of Solids*, 45(8):1253–1273, 1997.

A. Widjaja, E. Van der Giessen, and A. Needleman. Discrete dislocation analysis of the wedge indentation of polycrystals. *Acta Materialia*, 55(19):6408 – 6415, 2007.

A. J. Wilkinson, S. G. Roberts, and P. B. Hirsch. Modelling the threshold conditions for propagation of stage I fatigue cracks. *Acta Materialia*, 46(2):379 – 390, 1998.

Y. Xiang, H. Wei, P. Ming, and E. Weinan. A generalized peierls−nabarro model for curved dislocations and core structures of dislocation loops in *al* and *cu*. *Acta Materialia*, 56(7):1447 – 1460, 2008.

S. P. Xiao and T. Belytschko. A bridging domain method for coupling continua with molecular dynamics. *Computer methods in applied mechanics and engineering*, 193 (17):1645–1669, 2004.

X. P. Xu and A. Needleman. Void nucleation by inclusion debonding in a crystal matrix. *Modelling and Simulation in Materials Science and Engineering*, 1:111, 1993.

Y. Xue, D. L. McDowell, M. Horstemeyer, M. H. Dale, and J. B. Jordon.

Microstructure-based multistage fatigue modeling of aluminum alloy 7075-T651. *Engineering Fracture Mechanics*, 74(17):2810 – 2823, 2007.

H. M. Zbib and E. C. Aifantis. On the localization and postlocalization behavior of plastic deformation: I: On the initiation of shear bands. *Res Mechanica*, 23(2): 261–277, 1988.

H. M. Zbib and T. Diaz de la Rubia. A multiscale model of plasticity. *International Journal of Plasticity*, 18(9):1133–1163, 2002.

M. Zhou, A. Needleman, and R. J. Clifton. Finite element simulations of shear localization in plate impact. *Journal of the Mechanics and Physics of Solids*, 42 (3):423–458, 1994.